In: Advances in Mathematics Research, Volume 8
Editor: Albert R. Baswell, pp. 1-87
ISBN: 978-1-60456-454-9
© 2009 Nova Science Publishers, Inc.

Chapter 1

THE METHOD OF CHARACTERISTICS FOR THE NUMERICAL SOLUTION OF HYPERBOLIC DIFFERENTIAL EQUATIONS

M. Shoucri
Institut de Recherche d'Hydro-Québec (IREQ), Varennes, Québec, Canada J3X1S1

Abstract

The application of the method of characteristics for the numerical solution of hyperbolic type partial differential equations will be presented. Especial attention will be given to the numerical solution of the Vlasov equation, which is of fundamental importance in the study of the kinetic theory of plasmas, and to other equations pertinent to plasma physics. Examples will be presented with possible combination with fractional step methods in the case of several dimensions. The methods are quite general and can be applied to different equations of hyperbolic type in the field of mathematical physics. Examples for the application of the method of characteristics to fluid equations will be presented, for the numerical solution of the shallow water equations and for the numerical solution of the equations of the incompressible ideal magnetohydrodynamic (MHD) flows in plasmas.

Copyright © 2009. Nova Science Publishers, Inc.. All rights reserved.

1. Introduction

Different types of partial differential equations require different numerical methods of solution. Numerical methods for hyperbolic equations are generally more complicated and difficult to develop compared to the numerical methods applied for parabolic or elliptic type partial differential equations. There has been important advances in the last few decades in the domain of the numerical solution of hyperbolic type partial differential equations using the method of characteristics, when applied to solve the initial value problem for general first order partial differential equations The order of a partial differential equation is the order of the highest-order partial derivative that appears in the equation. Let us consider for example the following simple hyperbolic type advection equation:

Baswell, Albert R.. Advances in Mathematics Research, Nova Science Publishers, Inc., 2009. ProQuest Ebook Central, http://ebookcentral.proquest.com/lib/inflibnet-ebooks/detail.action?docID=3019187.
Created from inflibnet-ebooks on 2018-02-22 20:59:47.

$$\frac{\partial f}{\partial t} + c\frac{\partial f}{\partial x} = 0 . \tag{1.1}$$

where c is a constant, sometimes called the velocity of propagation. The characteristic equation to solve Eq.(1.1) is $dx/dt = c$. The rate at which the solution will propagate along the characteristics is c. If c is a constant, all the points on the solution profile will move at the same speed along the characteristics determined by the solution of $dx/dt = c$. Let us assume the initial condition $x(0) = x_0$. The solution of the characteristic equation gives the characteristic curves $x = x_0 + ct$ (a straight line for the present case where c is a constant), where x_0 is the point where each curve intersects the x-axis at t=0 in the x-t plane. If at t=0 we have $f \equiv f(x_0)$, $x_0 = x - ct$, then $f(x,t) = f(x - ct)$. The function $f(x,t)$ remains constant along a characteristic, which can be verified if we differentiate $f(x,t)$ along one of these curves to find the rate of change of f along the characteristic:

$$\frac{df(x(t),t)}{dt} = \frac{\partial f(x(t),t)}{\partial t} + \frac{dx}{dt}\frac{\partial f(x(t),t)}{\partial x} = \frac{\partial f}{\partial t} + c\frac{\partial f}{\partial x} = 0 . \tag{1.2}$$

which verify that f is constant along the characteristic curves. This is the simplest mathematical model of wave propagation. Constant quantities along the characteristic curves are called Riemann invariant [1]. We next consider the variable coefficient advection equation written as follows:

$$\frac{\partial f}{\partial t} + g(x,t)\frac{\partial f}{\partial x} = 0 . \tag{1.3}$$

The characteristic equation is $dx/dt = g(x,t)$. Again if the value of f at some arbitrary point (x_0, t_0) is known, the coordinate of the characteristic curve passing through (x_0, t_0) can be determined by integrating the ordinary differential equation $dx/dt = g(x,t)$. The velocity of propagation depends now on the spatial coordinate and time. In the general case an analytic solution is not straightforward and the characteristic curves are not straight lines anymore. Also it will be possible for the characteristic curves to intersect. The solution obtained by following the characteristic curves may contain discontinuities, which can lead to the formation of shocks or rarefaction waves [1]. Numerical techniques can be used to produce good approximations by following the solution computationally with small time-steps . As an example, we can discretize Eq.(1.3) as follows:

$$\frac{f(x,t+dt) - f(x,t)}{dt} + g(x,t)\frac{f(x,t) - f(x-dx,t)}{dx} = 0 . \tag{1.4}$$

Copyright © 2009. Nova Science Publishers, Inc.. All rights reserved.

Baswell, Albert R.. Advances in Mathematics Research, Nova Science Publishers, Inc., 2009. ProQuest Ebook Central, http://ebookcentral.proquest.com/lib/inflibnet-ebooks/detail.action?docID=3019187.
Created from inflibnet-ebooks on 2018-02-22 20:59:47.

$$f(x,t+dt) = f(x,t) - g(x,t).\frac{dt}{dx}.(f(x,t) - f(x-dx,t) = f(x-dx,t). \quad (1.5)$$

For a small time-step between t and $t+dt$, it is possible to write the solution for the characteristic equation between x and $x+dx$ in the form:

$$dx = \int_{t}^{t+dt} g(x(t'),t')dt' . \quad (1.6)$$

Substituting in the right hand side of Eq.(1.5), we get:

$$f(x,t+dt) = f(x - \int_{t}^{t+dt} g(x(t'),t')dt',t) . \quad (1.7)$$

Eq.(1.5) and Eq.(1.7) indicate that the value of the function f at the time $t+dt$ and at a position x is equal to the value of the function at time t, at the shifted position $x - dx = x - \int_{t}^{t+dt} g(x(t'),t')dt'$. Eq.(1.7) is an implicit equation, and in all but the simplest cases different numerical approximations must be used to write an explicit solution. It is the purpose of the present chapter to discuss some of these approximations through examples and numerical methods applied to hyperbolic equations. Some of these approximations have been recently discussed for instance in [2,3]. The value of the function at the shifted position is usually calculated by interpolation from the known values of the function at the neighbouring grid points. In the present chapter cubic splines interpolation will be extensively used to calculate the shifted value in Eq.(1.7), since in several applications and problems they have compared favourably with other methods of interpolation [4]. For the more general case where several dimensions are involved, the fractional step technique allows sometimes the reduction of the multi-dimensional equation to an equivalent set of one dimensional equations [2-5]. The shifts become fractional, i.e. each of the dimension is shifted separately. The specific order, number of shifts and choice of the size of shift-factors depend now on the numerical method. If the fractional step technique cannot be applied, we can use other methods which consist in interpolating in several dimensions using a tensor product of *B*-splines [6]. This technique has been extensively applied in the field of meteorology [7,8], where it is called the semi-Lagrangian method (although we prefer to call it the Euler-Lagrange method, since it essentially uses a fixed Eulerian grid, and uses a corrector or an iterative process to take care of the variation of the velocity along the characteristic curve).

We can generalize Eq.(1.3) for a multi-dimensional problem in the following form:

$$\frac{df}{dt} = \frac{\partial f}{\partial t} + \mathbf{G}(\mathbf{r},t).\frac{\partial f}{\partial \mathbf{r}} = 0 . \quad (1.8)$$

Copyright © 2009. Nova Science Publishers, Inc.. All rights reserved.

Baswell, Albert R.. Advances in Mathematics Research, Nova Science Publishers, Inc., 2009. ProQuest Ebook Central, http://ebookcentral.proquest.com/lib/inflibnet-ebooks/detail.action?docID=3019187.
Created from inflibnet-ebooks on 2018-02-22 20:59:47.

which reflects the fact that the function $f(\mathbf{r},t)$ is constant along the trajectories defined by the characteristic curves :

$$\frac{d\mathbf{r}}{dt} = \mathbf{G}(\mathbf{r},t)\,. \tag{1.9}$$

Denoting by $\mathbf{r}(t;\mathbf{r_i},t_n)$ the characteristic crossing the grid point $\mathbf{r_i}$ at t_n , we can also write at $t = t_n$:

$$f(\mathbf{r}(t;\mathbf{r_i},t_n),t) = f(\mathbf{r}(t;\mathbf{r_i},t_n),t_n) = f(\mathbf{r_i},t_n)\,. \tag{1.10}$$

Replacing t_n by $t_n + \Delta t$ and t by $t - \Delta t$, results in :

$$f(\mathbf{r_i},t_n + \Delta t) = f(\mathbf{r}(t - \Delta t;\mathbf{r_i},t_n + \Delta t),t - \Delta t)\,. \tag{1.11}$$

$\mathbf{r}(t - \Delta t;\mathbf{r_i},t_n + \Delta t)$ is the characteristic which ends up at $\mathbf{r_i}$ at time $t_n + \Delta t$. The function value at the time-step $t_n + \Delta t$ and at the grid point $\mathbf{r_i}$ can be calculated by looking backward to the function value at an interstitial point, prescribed by the characteristic curve at the previous time $t - \Delta t$. The starting point at the previous time-step $t_n - \Delta t$, of the characteristic curve ending at $\mathbf{r_i}$ at time $t_n + \Delta t$, is denoted by $\tilde{\mathbf{r}} = \mathbf{r}(t_n - \Delta t;\mathbf{r_i},t_n + \Delta t)$ (see Fig.(1)). Usually $\tilde{\mathbf{r}}$ is an intermediate interstitial point which does not coincide with a grid point. The value of the function at $\tilde{\mathbf{r}}$ has to be calculated by interpolation. Discretizing Eq.(1.9) of the characteristic curves using a leap-frog scheme, we can write:

$$\frac{\mathbf{r}(t_n + \Delta t) - \mathbf{r}(t_n - \Delta t)}{2\Delta t} \equiv \frac{\mathbf{r_i} - \tilde{\mathbf{r}}}{2\Delta t} = \mathbf{G}(\mathbf{r}(t_n),t_n)\,. \tag{1.12}$$

Using $\mathbf{r}(t_n) \approx \big(\mathbf{r}(t_n + \Delta t) + \mathbf{r}(t_n - \Delta t)\big)/2 \equiv (\mathbf{r_i} + \tilde{\mathbf{r}})/2$ in the right hand side of Eq.(1.12), results in $\Delta_{\mathbf{r}} = \Delta t\mathbf{G}(\mathbf{r_i} - \Delta_{\mathbf{r}},t_n)$, where $\Delta_{\mathbf{r}} = (\mathbf{r_i} - \tilde{\mathbf{r}})/2$. We solve this equation numerically for $\Delta_{\mathbf{r}}$ using the Newton iterative scheme :

$$\Delta_{\mathbf{r}}^{k+1} = \Delta t\mathbf{G}(\mathbf{r_i} - \Delta_{\mathbf{r}}^{\mathbf{k}},t_n) \tag{1.13}$$

starting with k=0, $\Delta_{\mathbf{r}}^{0} = 0$. Two or three iterations are usually sufficient to converge to precise results. We then calculate the value of f at the position $\mathbf{r_i}$ at $t_n + \Delta t$:

Copyright © 2009. Nova Science Publishers, Inc.. All rights reserved.

Baswell, Albert R.. Advances in Mathematics Research, Nova Science Publishers, Inc., 2009. ProQuest Ebook Central, http://ebookcentral.proquest.com/lib/inflibnet-ebooks/detail.action?docID=3019187.
Created from inflibnet-ebooks on 2018-02-22 20:59:47.

$$f(\mathbf{r_i}, t_n + \Delta t) = f(\mathbf{r}(t - \Delta t; \mathbf{r_i}, t_n + \Delta t), t_n - \Delta t) = f(\mathbf{r_i} - 2 * \Delta_{\mathbf{r}}, t_n - \Delta t) \,. \quad (1.14)$$

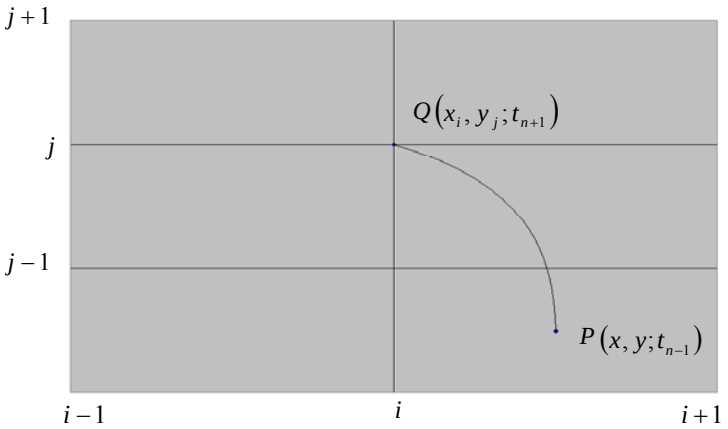

Figure 1.

The multi-dimensional interpolation in Eqs.(1.13-1.14) will generally involve a tensor product of *B*-splines. In practice, we will restrict ourselves to problems in two dimensions. In the Fig.(1) we give an example for the case of a two-dimensional space, showing the point of departure *P* at $t_n - \Delta t$, where the value of the function *f* is to be interpolated as in Eq.(1.14) to yield the value of $f(\mathbf{r_i}, t_n + \Delta t)$ at the point *Q*. Similar schemes have been extensively used in problems of meteorology [7,8], and more recently in plasma physics [6,9].

The ideas outlined in this introduction will be applied to selected problems in the present chapter. In section 2 we will present examples where a fractional step method reduces the multi-dimensional problem to an equivalent set of one-dimensional (1D) problems. In section 3 we will present examples where 2D interpolation involves a tensor product of cubic *B*-splines. We will emphasize the precision, good performance and numerical stability of the cubic splines interpolation, which have been also previously pointed out in [4,7]. Examples will be taken from the field of plasma physics, especially concerning the numerical solution of the Vlasov equation, of fundamental importance in the kinetic theory of plasmas. Some additional applications in the field of fluid dynamics will be presented in section 4, for the numerical solution of the shallow water equations, and for the numerical solution of the equations of the incompressible ideal magnetohydrodynamic flows in plasmas.

2. The Fractional Step Method Applied to the Vlasov Equation

The study of nonlinear processes in kinetic plasmas is heavily based on the numerical solution of the Vlasov equation for the distribution function. The Vlasov equation provides the basic dynamical description of hot plasmas in regimes where the effect of collisions are negligible with respect to those originating from the collective, mean-field electromagnetic interactions. The Vlasov-type equation is an advection equation in phase-space for the distribution function *f* , of the general form given in Eq.(1.8). Different techniques have been proposed to

Copyright © 2009. Nova Science Publishers, Inc.. All rights reserved.

Baswell, Albert R.. Advances in Mathematics Research, Nova Science Publishers, Inc., 2009. ProQuest Ebook Central, http://ebookcentral.proquest.com/lib/inflibnet-ebooks/detail.action?docID=3019187.
Created from inflibnet-ebooks on 2018-02-22 20:59:47.

solve this equation. Particle-in-cell (PIC) methods for instance approximate the plasma by a finite number of pseudo-particles and compute their trajectories given by Eq.(1.9). However, the numerical noise in these codes decreases only as $1/\sqrt{N}$, where N is the number of pseudo-particles in any particular computational cell. This noise problem becomes important if the physics of interest is in the low density region of phase-space or in the high energy tail of the distribution function. On the other hand the direct numerical solution of the Vlasov equation as a partial differential equation on a fixed grid in phase-space has become an important method for the numerical solution of the Vlasov equation. Interest in Eulerian grid-based Vlasov solvers arises from the very low noise level associated with these methods, and the recent advances of parallel computers have increased the interest in the applications of splitting schemes to higher dimensional problems. The original, ground-breaking publication of Cheng and Knorr [10], which proposed the second-order fractional step scheme or splitting scheme for the solution of the Vlasov-Poisson system, was followed by several publications where this method was successfully applied to one-dimensional (two-dimensional in phase-space) Vlasov- Poisson problems [11-14]. The technique was extended to higher phase-space dimensions [15-19]. An important application using the Eulerian splitting schemes for the Vlasov-Maxwell system of equations has been reported for the study of laser-plasma interaction [20-27 and references therein], and extended to two-dimensional problems [28]. In the work on beat wave current drive [29], a constant magnetic field was introduced in the Vlasov equation. Further applications in the recent work in [30,31] testify to the success of this method in laser-plasma interaction. We also note the application of Eulerian splitting schemes to study two spatial dimension problems of Kelvin-Helmholtz instabilities and higher dimensionality gyrokinetic equations [32-39]. There exists also a variety of other applications using different methods developed for Eulerian grid-based Vlasov solvers [40-44]. Of particular interest is the work coupling a Vlasov equation to a Fokker-Planck collision operator presented in [45]. In the present section 2 , we will present selected examples where the fractional step techniques associated with interpolation along the characteristic curves in one dimension are applied for the numerical solution of the Vlasov equation.

2.1. The Fractional Step Method Applied to the Vlasov-Poisson System in One Spatial Dimension

The first system we study is the Vlasov-Poisson system in one spatial dimension (a two-dimensional phase space x-v). The problem is the long time nonlinear evolution of a two-stream instability in a collisionless plasma [46,47]. The system in this case evolves to a Bernstein-Greene-Kruskal BKG equilibrium [48] consisting of a stationary structure exhibiting holes or vortices in phase-space. BKG structures with more than one hole are unstable and coalesce until the evolution brings a final stable vortex. This flow of energy of the system during the evolution to the longest wavelength available in the system (inverse cascade) is characteristic of two-dimensional systems and has been discussed in several publications (see for instance [49-50]). We use an Eulerian code associated with a method of fractional step for the integration of the Vlasov equation along the characteristics. The Eulerian method allows accurate resolution of the phase-space on a fixed Eulerian grid. In the present problem the spatial dimension x is assumed to be periodic. The normalized Vlasov

Copyright © 2009. Nova Science Publishers, Inc.. All rights reserved.

Baswell, Albert R.. Advances in Mathematics Research, Nova Science Publishers, Inc., 2009. ProQuest Ebook Central, http://ebookcentral.proquest.com/lib/inflibnet-ebooks/detail.action?docID=3019187.
Created from inflibnet-ebooks on 2018-02-22 20:59:47.

equation for the electron distribution function $f(x,v,t)$ and the Poisson equation for the potential $\varphi(x)$ are given by:

$$\frac{\partial f}{\partial t} + v\frac{\partial f}{\partial x} - E_x \frac{\partial f}{\partial v} = 0. \tag{2.1}$$

$$\frac{\partial^2 \varphi}{\partial x^2} = -(1 - n_e),$$

where $$n_e = \int_{-\infty}^{\infty} f\, dv, \text{ and } E_x = -\frac{\partial \varphi}{\partial x} \tag{2.2}$$

The ions form an immobile background in the present problem. The distance x, the velocity v and the time t are respectively normalized to the Debye length $\lambda_{De} = v_{th} / \omega_{pe}$, the thermal velocity v_{th} and the inverse plasma frequency ω_{pe}^{-1}. Eq.(2.1) is essentially a two-dimensional advection equation. An important property of this equation is that its characteristics, the particles trajectories $dx/dt = v$, $dv/dt = -E_x$ describe a Hamiltonian flow in phase-space. The particles motion is described by the Hamiltonian:

$$H = \frac{v^2}{2} + \varphi(x). \tag{2.3}$$

The Vlasov Eq.(2.1) can be written in the form:

$$\frac{\partial f}{\partial t} + [H, f] = 0. \tag{2.4}$$

The Poisson brackets $$[H, f] = \left\{ \frac{\partial H}{\partial v}\frac{\partial f}{\partial x} - \frac{\partial H}{\partial x}\frac{\partial f}{\partial v} \right\}$$

The distribution function *f* is constant along the particle trajectories. As a consequence, the integral over the entire phase-space of the distribution function is a constant, as well as the integral of any arbitrary smooth function of *f*. Thus the evolution of the distribution function *f* is constrained by a number of constants of motion. Hamiltonian systems like Eq.(2.4) are known to develop increasingly smaller scales during their nonlinear evolution. One way to control these finer structures is to increase resolution. These small structures dissipate when they reach the size of a the grid. We write the initial electron distribution function in the form[46]:

Copyright © 2009. Nova Science Publishers, Inc.. All rights reserved.

Baswell, Albert R.. Advances in Mathematics Research, Nova Science Publishers, Inc., 2009. ProQuest Ebook Central, http://ebookcentral.proquest.com/lib/inflibnet-ebooks/detail.action?docID=3019187.
Created from inflibnet-ebooks on 2018-02-22 20:59:47.

$$f(x,v,t=0) = A(1+\frac{\varepsilon}{1-\xi})\, e^{-\varepsilon}\, (1+\alpha\cos(k_0 x) + \beta\cos(2k_0 x) + \gamma\cos(3k_0 x)) \quad . \tag{2.5}$$

With $$A = \frac{1}{\sqrt{2\pi}}\frac{2-2\xi}{3-2\xi}$$

$\varepsilon = v^2/2$, and ξ is a parameter which characterizes a produced vortex in phase-space. $k_0 = \frac{2\pi}{L}$ denotes the fundamental wavenumber, L is the length of the periodic box. We choose $k_0 = \frac{k_M}{4}$, where k_M is the maximum wavenumber for instability [46] given by $k_M^2 = \frac{2\xi-1}{3-2\xi}$, which leads to a box length $L = 8\pi\sqrt{\frac{3-2\xi}{2\xi-1}}$. We choose $\xi = 0.90$, which gives $k_M = 0.816$, $L = 30.78\lambda_{De}$ and $k_0 = 0.204$.

We take a cut-off velocity at $v_{\max} = \pm 6 v_{th}$. The distribution function is given at mesh points in the phase-space, with $N_x = 128$ points in space and $N_v = 256$ points in velocity space. The time-step is $\Delta t = 0.25\omega_{pe}^{-1}$. A method which has second order in time precision [10,11] is obtained by splitting Eq.(2.1) as follows:

Step1 - Solve $\frac{\partial f}{\partial t} + v\frac{\partial f}{\partial x} = 0$ for a step $\Delta t/2$ (2.6)

- Solve Poisson equation for the electric field which we denote by E_x^*.

Step2 -Solve $\frac{\partial f}{\partial t} - E_x^*\frac{\partial f}{\partial v} = 0$ for a step Δt (2.7)

Step3 -Solve $\frac{\partial f}{\partial t} + v\frac{\partial f}{\partial x} = 0$ for a step $\Delta t/2$ (2.8)

In this 2D phase-space problem the shifts become fractional, i.e. each of the dimension of the phase-space is shifted separately. This splitting has the advantage that each of the *x* or *v* updates is a linear advection effected by applying successively the shifts :

$$f^a(x,v,t+\Delta t/2) = f(x - v\Delta t/2, v, t), \tag{2.9}$$

$$f^b(x,v,t+\Delta t) = f^a(x, v - E_x^*\Delta t, t), \tag{2.10}$$

Copyright © 2009. Nova Science Publishers, Inc.. All rights reserved.

Baswell, Albert R.. Advances in Mathematics Research, Nova Science Publishers, Inc., 2009. ProQuest Ebook Central, http://ebookcentral.proquest.com/lib/inflibnet-ebooks/detail.action?docID=3019187.
Created from inflibnet-ebooks on 2018-02-22 20:59:47.

$$f(x,v,t+\Delta t/2) = f^{b}(x - v\Delta t/2, v, t), \tag{2.11}$$

That is, half of the spatial shift is performed first in space. Since *v* is an independent variable, the shift in Eq.(2.9) is done as in Eq.(1.1) for each value of *v* (see Appendix A). This is followed by solving Poisson equation for the calculation of the electric field E_x^*, which is used for the calculation of the total shift in velocity space where the integral in Eq.(1.7) is approximated as in Eq.(2.10). Poisson equation in Eq.(2.2) is discretized in space as a tridiagonal matrix:

$$\varphi_{j-1} - 2\varphi_j + \varphi_{j+1} = -\Delta x^2 (1 - n_{ej}). \tag{2.12}$$

where $\Delta x = L/N_x$, the subscript *j* denotes the grid-point x_j . Eq.(2.12) is solved using appropriate boundary conditions (periodic boundary conditions for the present problem). From φ we calculate E_x^* (Eq.(2.2)). Finally the second half of the spatial shift is repeated in Eq.(2.11). It has been shown in [10] that the overall precision of this numerical scheme is $O(\Delta t^2)$. We can verify after this sequence that the distribution function f^{n+1} at time $t = (n+1)\Delta t$ can be written as follows:

$$\begin{aligned} f^{n+1}(x,v) &= f^{n}(x^*, v^*) \\ x^* &= x - \Delta t(v + \frac{1}{2} E_x(x - v\Delta t/2)\Delta t). \\ v^* &= v + E_x(x - v\Delta t/2) \end{aligned} \tag{2.13}$$

On the other hand we can consider the characteristics equations , $dx/dt = v$, $dv/dt = -E_x$, which are the particles trajectory. The integration of these equations between *t* and $t = t + \Delta t$ gives the following result :

$$\begin{aligned} x(t) &= x(t+\Delta t) - \Delta t(v(t+\Delta t) + 1/2 E_x(\bar{x}, t+\Delta t/2)\Delta t) \\ v(t) &= v(t+\Delta t) + \Delta t E_x(\bar{x}, t+\Delta t/2) \end{aligned} . \tag{2.14}$$

where $\bar{x} = x(t + \Delta t/2)$. The field $E_x(x,t)$ in Eq.(2.7) is calculated after the first shift. The density distribution, and therefore $E_x(x,t)$, remains unaffected by the second shiht. Thus the field $E_x(\bar{x}, t+\Delta t/2)$ can be approximated by $E_x(x - v\Delta t/2, t+\Delta t/2)$. The shifts in Eqs.(2.9-2.11) are calculated using a cubic spline interpolation as defined in the appendices. For the present problem, we used the results in Appendix A.

Copyright © 2009. Nova Science Publishers, Inc.. All rights reserved.

Baswell, Albert R.. Advances in Mathematics Research, Nova Science Publishers, Inc., 2009. ProQuest Ebook Central, http://ebookcentral.proquest.com/lib/inflibnet-ebooks/detail.action?docID=3019187.
Created from inflibnet-ebooks on 2018-02-22 20:59:47.

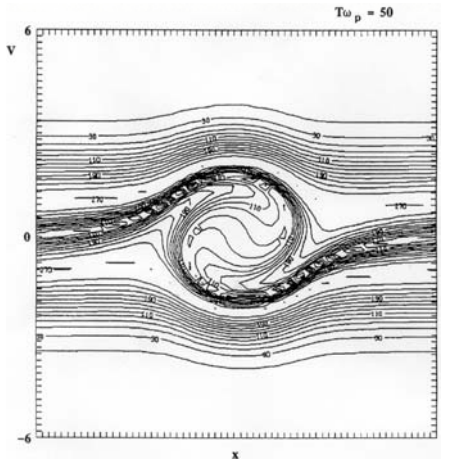

Figure 2. The vorticity at t=50 ω_{pe}^{-1}.

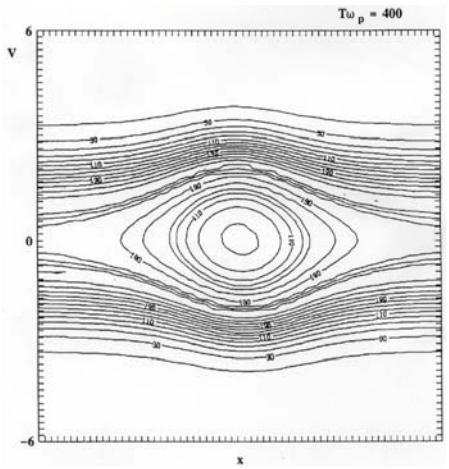

Figure 3. The vorticity at t=100 ω_{pe}^{-1}.

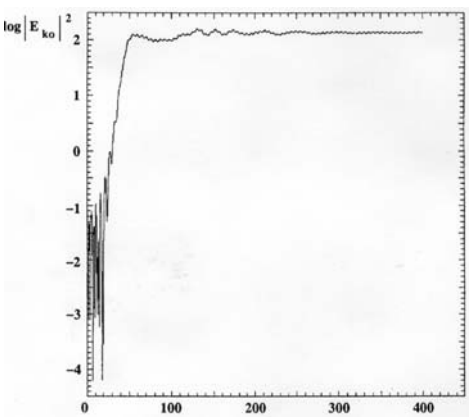

Figure 4. Time evolution of the first Fourier mode.

Copyright © 2009. Nova Science Publishers, Inc.. All rights reserved.

Baswell, Albert R.. Advances in Mathematics Research, Nova Science Publishers, Inc., 2009. ProQuest Ebook Central, http://ebookcentral.proquest.com/lib/inflibnet-ebooks/detail.action?docID=3019187.
Created from inflibnet-ebooks on 2018-02-22 20:59:47.

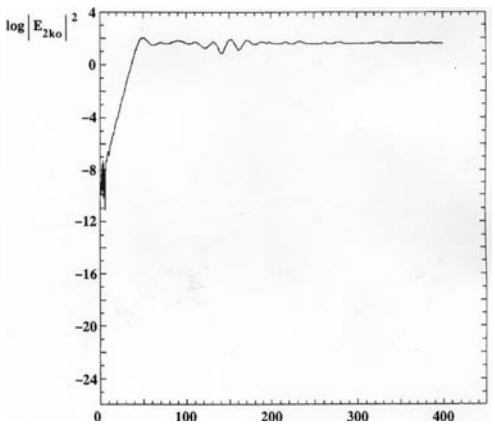

Figure 5. Time evolution of the second Fourier mode.

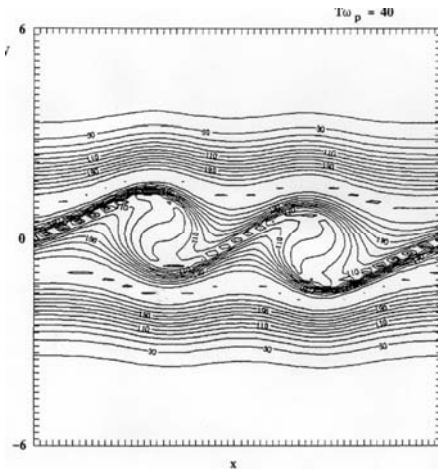

Figure 6. The vorticity at t=40 ω_{pe}^{-1}.

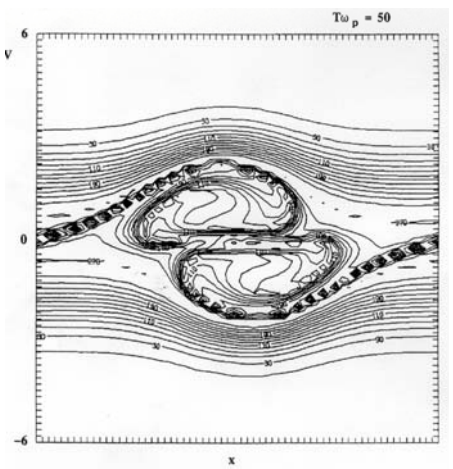

Figure 7. The vorticity at t=50 ω_{pe}^{-1}.

Copyright © 2009. Nova Science Publishers, Inc.. All rights reserved.

Baswell, Albert R.. Advances in Mathematics Research, Nova Science Publishers, Inc., 2009. ProQuest Ebook Central, http://ebookcentral.proquest.com/lib/inflibnet-ebooks/detail.action?docID=3019187.
Created from inflibnet-ebooks on 2018-02-22 20:59:47.

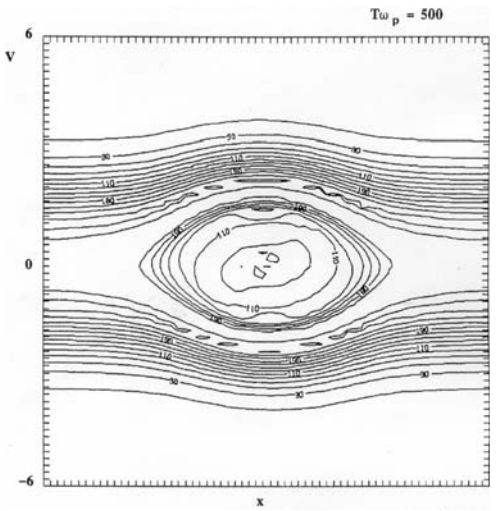

Figure 8. The vorticity at t=500 ω_{pe}^{-1}.

We apply the numerical scheme previously discussed to study the evolution of a two-stream instability. We introduce a perturbation on the fundamental wavenumber k_0 by taking $\alpha = 0.001$ and $\beta = \gamma = 0.$ Only one vortex appears in phase space during the nonlinear plasma evolution (see Fig.(2)), and the final equilibrium in Fig.(3) consists of a single smooth hole. Fig.(4) and Fig.(5) show the nonlinear evolution of the first and second Fourier modes respectively, showing the initial growth and saturation. In a second experiment, we start with a perturbation in Eq.(2.5) of the three modes, $\alpha = 0.001$, $\beta = \gamma = \alpha/1.2$. We obtain in the first step the appearance of two vortices in the phase-space shown in Fig.(6) at $t = 40\omega_{pe}^{-1}$, followed rapidly by the coalescence of the vortices at $t = 50\omega_{pe}^{-1}$ in Fig.(7) (so the two vortices structure is not stable). Note the tendency of holes to behave as quasi-particles just before coalescence [47]. We finally end up with a single vortex (see Fig.(8)). We note again this tendency of the energy to move to the longest wavelength available in the system [49,50] (the so called inverse cascade), which is characteristic of two dimensional systems. Small scale vortices can be created in the transient regime, but they rapidly coalesce to give rise to larger vortices, and finally only large scale structures persist. The system selects the longest wavelength allowed by the imposed boundary conditions. Fig.(9) and Fig.(10) show the nonlinear evolution of the first and second Fourier modes respectively, showing the initial growth and saturation. We note that the saturation level decreases the higher the mode. Statistical studies presented in [49,50] for 2D systems predict for two dimensional systems a level of the energy associated with the different Fourier modes of the form $\left|E_k\right|^2 = 1/(\delta + \sigma k^2)$ (δ and σ are constants), with energy condensing in the low k modes (inverse cascade). We note the strong influence of the initial conditions on the plasma evolution, although the final state is generally a single vortex structure. We also note the accurate and stable performance of the noiseless Eulerian numerical code, which provided precise information on the phase-space behaviour of the one-dimensional Vlasov plasma.

Copyright © 2009. Nova Science Publishers, Inc.. All rights reserved.

Baswell, Albert R.. Advances in Mathematics Research, Nova Science Publishers, Inc., 2009. ProQuest Ebook Central, http://ebookcentral.proquest.com/lib/inflibnet-ebooks/detail.action?docID=3019187.
Created from inflibnet-ebooks on 2018-02-22 20:59:47.

Finally we point to the extension of the fractional step method to a fourth order scheme using a symplectic integrator, recently reported in [42].

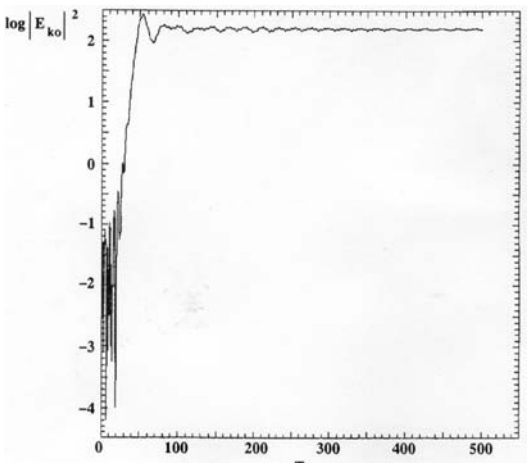

Figure 9. Time evolution of the first Fourier mode.

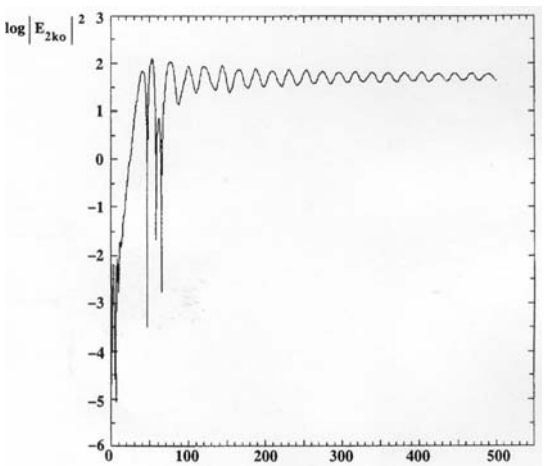

Figure 10. Time evolution of the second Fourier mode.

2.2. The Vlasov-Poisson System in Higher Phase-Space Dimensions: the Problem of the Formation of an Electric Field at a Plasma Edge in a Slab Geometry

Further evaluation of the performance of the cubic spline interpolation with respect to other interpolation methods, like the cubic interpolated propagation CIP method and the flux corrected transport method, has been presented in [4] and shows the cubic spline interpolation compares favourably with respect to the other methods. We consider in this section the problem of the charge separation at a plasma edge. This problem, with the calculation of the self-consistent electric field along a steep gradient, is of major importance in many physical problems. In tokamak physics, it is highly relevant to the edge physics associated with the

Copyright © 2009. Nova Science Publishers, Inc.. All rights reserved.

Baswell, Albert R.. Advances in Mathematics Research, Nova Science Publishers, Inc., 2009. ProQuest Ebook Central, http://ebookcentral.proquest.com/lib/inflibnet-ebooks/detail.action?docID=3019187.
Created from inflibnet-ebooks on 2018-02-22 20:59:47.

high confinement mode (H mode). Two methods will be used to study this problem, and the results obtained will be compared. In the first method presented in this section, Cartesian geometry (a slab model) will be used at the edge of the plasma, and a fractional step technique associated with 1D interpolation using a cubic spline will be applied. In the second method to be presented in section 3.2, we will discuss the solution of the same problem at the plasma edge using cylindrical coordinates (r, θ, z), with a code which applies a 2D interpolation using a tensor product of cubic *B*-splines [6,51]. The plasma is assumed to be in front of a floating limiter with the magnetic field being aligned parallel to the limiter surface. Electrons are assumed to be frozen along the magnetic field lines. We compare the electric field with the macroscopic values calculated from the same kinetic codes for the gradient of the ion pressure and the Lorentz force term. We find that along the gradient, these quantities balance exactly the electric field.

The inhomogeneous direction in the 1D slab geometry considered is the *x* direction, normal to the limiter plane (*y*, *z*). The constant magnetic field is in the *y* direction (assumed to represent the toroidal direction), and *z* represents the poloidal direction. The ions are described by the 1D in space (three phase-space dimensions) Vlasov equation for the ion distribution function $f_i(x, v_x, v_z, t)$:

$$\frac{\partial f_i}{\partial t} + v_x \frac{\partial f_i}{\partial x} + \left(E_x - v_z\ \omega_{ci}\right) \frac{\partial f_i}{\partial v_x} + v_x \omega_{ci} \frac{\partial f_i}{\partial v_z} = 0 \tag{2.15}$$

In Eq.(2.15) time is normalized to the inverse ion plasma frequency ω_{pi}^{-1}, velocity is normalized to the acoustic velocity $c_s = \sqrt{T_e / M_i}$ (T_e is the electron temperature and M_i is the ion mass), and length is normalized to the Debye length $\lambda_{De} = c_s / \omega_{pi}$, where ω_{pi} is the ion plasma frequency. The potential is normalized to T_e / e, and the density is normalized to the peak initial central density. ω_{ci} is the ion cyclotron frequency. We assume deuterons plasma. The system is solved over a length $L = 175\ \lambda_{De}$ in front of the limiter plate, with an initial density profile for the ions and electrons (indices *i* and *e* denote ions and electrons respectively):

$$n_i = n_e = 0.5\left(1 + \tanh\left((x - L/5)/7\right)\right) \tag{2.16}$$

The initial value of the ion distribution function $f_i(x, v_x, v_z)$ is given by:

$$f_i(x, v_x, v_z) = n_i(x) \frac{e^{-(v_x^2 + v_z^2)/2T_i}}{2\pi T_i} \tag{2.17}$$

The magnetized electrons are frozen along the magnetic field lines, with a constant profile given by Eq. (2.16). In this case the electrons cannot move across the magnetic field in

Copyright © 2009. Nova Science Publishers, Inc.. All rights reserved.

Baswell, Albert R.. Advances in Mathematics Research, Nova Science Publishers, Inc., 2009. ProQuest Ebook Central, http://ebookcentral.proquest.com/lib/inflibnet-ebooks/detail.action?docID=3019187.
Created from inflibnet-ebooks on 2018-02-22 20:59:47.

the gradient region to compensate the charge separation which is built up due to the finite ion orbits. It is important to calculate the ion orbits accurately by using an accurate Eulerian Vlasov code. The larger the ion gyroradius, the bigger the charge separation and the self-consistent electric field at the edge. (Hence the important role played by even a small fraction of impurity ions). The electric field is calculated from the Poisson equation:

$$\frac{\partial^2 \varphi}{\partial x^2} = -\left(n_i - n_e\right) \quad ; \qquad E_x = -\frac{\partial \varphi}{\partial x} \tag{2.18}$$

The following parameters are used for deuterium ions:

$$\frac{\omega_{ci}}{\omega_{pi}} = 0.1\,; \qquad \frac{T_i}{T_e} = 1\,; \qquad \frac{\rho_i}{\lambda_{De}} = \sqrt{\frac{2T_i}{T_e}}\,\frac{1}{\omega_{ci}/\omega_{pi}} = 10\sqrt{2} \tag{2.19}$$

If we assume an initial Maxwellian distribution for the ions with $T_{ix} = T_{iz} = T_i$ spatially constant, then the factor $2T_i$ in the calculation of the gyro-radius in Eq.(2.19) takes into account that the perpendicular temperature $< v_\perp^2 > = < v_x^2 > + < v_z^2 > = 2T_i / m_i$. We assume in the present calculation that the deuterons hitting a wall at $x = 0$ are collected by a floating limiter. Since the magnetized electrons do not move in the x direction across the magnetic field there is no electron current collected at the floating limiter. Therefore we have at $x = 0$ the relation :

$$\left.\frac{\partial E_x}{\partial t}\right|_{x=0} = -J_{xi}\big|_{x=0} \qquad \text{or} \qquad E_x\big|_{x=0} = -\int_0^t J_{xi}\big|_{x=0}\, dt \tag{2.20}$$

Integrating Eq. (2.18) over the domain (0, *L)*, we get the total charge σ in the system:

$$E_x\big|_{x=L} - E_x\big|_{x=0} = \int_0^x \left(n_i - n_e\right) dx = \sigma \tag{2.21}$$

The difference between the electric fields at the boundaries must be equal to the charge appearing in the system. Equation (2.15) is solved by a method of fractional step, in which the advection term in space is solved first, then the equation in velocity space can be solved either using 2D interpolation with a tensor product of cubic *B*-spline as discussed in [51] (to be applied in section 3.2) , or by successive 1D cubic spline interpolation as follows:

Step1- Solve $$\frac{\partial f}{\partial t} + v_x \frac{\partial f}{\partial x} = 0 \ \text{ for a step } \Delta t / 2 \tag{2.22}$$

Copyright © 2009. Nova Science Publishers, Inc.. All rights reserved.

Baswell, Albert R.. Advances in Mathematics Research, Nova Science Publishers, Inc., 2009. ProQuest Ebook Central, http://ebookcentral.proquest.com/lib/inflibnet-ebooks/detail.action?docID=3019187.
Created from inflibnet-ebooks on 2018-02-22 20:59:47.

- Solve Poisson equation for the electric field which we denote by $E_x^{n+1/2}$.

Step2- Solve $$\frac{\partial f}{\partial t} + (E_x^{n+1/2} - v_z\omega_{ci})\frac{\partial f}{\partial v_x} = 0 \text{ for a step } \Delta t/2 \tag{2.23}$$

Step3- Solve $$\frac{\partial f}{\partial t} + v_x\omega_{ci}\frac{\partial f}{\partial v_z} = 0 \text{ for a step } \Delta t \tag{2.24}$$

Step4- Repeat Step2 for a time step $\Delta t/2$

Step5- Repeat Step1 for a time step $\Delta t/2$

This splitting leads to the following successive shifts :

$$f^a(x,v_x,v_z,t+\Delta t/2) = f(x - v_x\Delta t/2, v_x, v_z, t), \tag{2.25}$$

$$f^b(x,v_x,v_z,t+\Delta t/2) = f^a(x, v_x - E_x^{n+1/2}\Delta t/2 + v_z\omega_{ci}\Delta t/2, v_z, t), \tag{2.26}$$

$$f^c(x,v_x,v_z,t+\Delta t) = f^b(x, v_x, v_z - v_z\omega_{ci}\Delta t, t), \tag{2.27}$$

We then repeat Eq.(2.26) and Eq.(2.25) to complete the cycle. We can then verify after this sequence that the distribution function f^{n+1} at time $t = (n+1)\Delta t$ can be written in the following form:

$$f^{n+1}(x,v_x,v_z) = f^n(x^*, v_x^*, v_z^*) \tag{2.28}$$

where:

$$x^* = x - v_x\Delta t + \frac{1}{2}E_x^*\Delta t^2 - v_z\omega_{ci}\frac{\Delta t^2}{2} \tag{2.29}$$

$$v_x^* = v_x - E_x^*\Delta t + v_z\omega_{ci}\Delta t - \frac{1}{2}v_x\omega_{ci}^2\Delta t^2 \tag{2.30}$$

$$v_z^* = v_z - v_x\omega_{ci}\Delta t + \frac{1}{2}\omega_{ci}E_x^*\Delta t^2 - \frac{1}{2}v_z\omega_{ci}^2\Delta t^2 \tag{2.31}$$

where $E_x^* = E_x(x - v_x\Delta t/2, t = n\Delta t + \Delta t/2)$

Copyright © 2009. Nova Science Publishers, Inc.. All rights reserved.

Baswell, Albert R.. Advances in Mathematics Research, Nova Science Publishers, Inc., 2009. ProQuest Ebook Central, http://ebookcentral.proquest.com/lib/inflibnet-ebooks/detail.action?docID=3019187.
Created from inflibnet-ebooks on 2018-02-22 20:59:47.

On the other hand , we can consider the characteristics equations for Eq.(2.15) which describe the particles motion:

$$\frac{dx}{dt} = v_x \tag{2.32}$$

$$\frac{dv_x}{dt} = E_x - v_z \omega_{ci} \tag{2.33}$$

$$\frac{dv_z}{dt} = v_x \omega_{ci} \tag{2.34}$$

By integrating the Eqs.(2.32-2.34) from $t_n = n\Delta t$ to $t_{n+1} = (n+1)\Delta t$, we get:

$$x^n = x^{n+1} - v_x^{n+1} \frac{\Delta t}{2} - v_x^n \frac{\Delta t}{2} \tag{2.35}$$

$$v_x^n = v_x^{n+1} - E_x^{n+1/2} \Delta t + \omega_{ci} v_z^{n+1} \frac{\Delta t}{2} + \omega_{ci} v_z^n \frac{\Delta t}{2} \tag{2.36}$$

$$v_z^n = v_z^{n+1} - v_x^{n+1} \omega_{ci} \frac{\Delta t}{2} - v_x^n \omega_{ci} \frac{\Delta t}{2} \tag{2.37}$$

Eqs(2.35-2.36) leads to the following solution correct to second order in Δt :

$$x^n = x^{n+1} - v_x^{n+1} \Delta t + E_x^{n+1/2} \frac{\Delta t^2}{2} - \omega_{ci} v_z^{n+1} \frac{\Delta t^2}{2} \tag{2.38}$$

$$v_x^n = v_x^{n+1} - E_x^{n+1/2} \Delta t + \omega_{ci} v_z^{n+1} \Delta t - \omega_{ci}^2 v_x^{n+1} \frac{\Delta t^2}{2} \tag{2.39}$$

$$v_z^n = v_z^{n+1} - v_x^{n+1} \omega_{ci} \Delta t + \omega_{ci} E_x^{n+1/2} \frac{\Delta t^2}{2} - v_z^{n+1} \omega_{ci}^2 \frac{\Delta t^2}{2} \tag{2.40}$$

By comparing Eqs.(2.29-2.31) to Eqs.(2.38-2.40), we see that the splitting scheme integrates the distribution function along the characteristics correctly to an order $O(\Delta t^2)$. (Note also that to an order $O(\Delta t^2)$, v_z^{n+1} in the last term in Eq.(2.40) can be substituted by v_z^n).

Copyright © 2009. Nova Science Publishers, Inc.. All rights reserved.

Baswell, Albert R.. Advances in Mathematics Research, Nova Science Publishers, Inc., 2009. ProQuest Ebook Central, http://ebookcentral.proquest.com/lib/inflibnet-ebooks/detail.action?docID=3019187.
Created from inflibnet-ebooks on 2018-02-22 20:59:47.

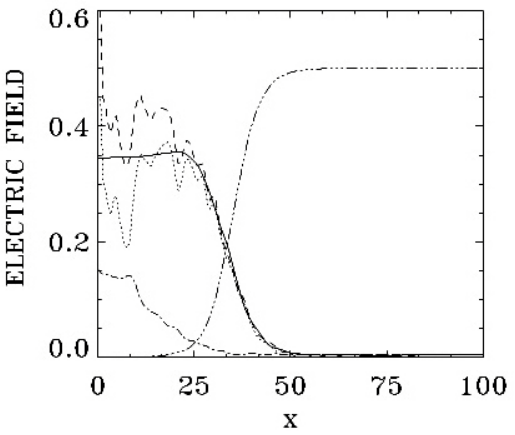

Figure 11. Plot, for the Cartesian geometry, of the electric field E_x (solid curve), the Lorentz force $+0.1<v_z>$ (dash- dotted curve), the pressure force $\nabla P_i / n_i$ (dotted curve), and the sum $\nabla P_i / n_i + 0.1<v_z>$ (broken curve). The density $n_i/2$ is is also plotted (dash- three-dots curve, plotted for reference).

We assume that the gyrating plasma deuterons are allowed to enter or leave at the right boundary. So the electric field at the right boundary $x = L$ must be such that the difference between the electric fields at both boundaries in Eq. (2.21) is equal to the total charge σ appearing in the system. Fig. (11) shows at $t = 500$ the plot of the electric field E_x (solid curve, we concentrate on the region $x < 100$ to emphasize the gradient region, although the system extends to $x = 175$). We also plot $n_i / 2$ (dash-three-dots curve) in the same figure for reference. The dash-dotted curve gives the Lorentz force, which in our normalized units is given by $<v_z>\omega_{ci}/\omega_{pi} = 0.1<v_z>$, and the dotted curve gives the pressure force $\nabla P_i / n_i$, $P_i = 0.5\, n_i\left(T_{ix} + T_{iz}\right)$, with:

$$T_{ix,z}(x) = \frac{1}{n_i}\int dv_x dv_z \left(v_{x,z} - <v_{x,z}>\right)^2 \; f_i\left(x, v_x, v_z\right) \tag{2.41}$$

$$<v_{x,z}> = \frac{1}{n_i}\int dv_x dv_z v_{x,z}\, f_i\left(x, v_x, v_z\right); \qquad n_i(x) = \int dv_x dv_z\, f_i\left(x, v_x, v_z\right) \tag{2.42}$$

In steady state the transport $<v_x>$ vanishes. The broken curve in Fig. (11) gives the sum $\nabla P_i / n_i + 0.1<v_z>$, which shows a good agreement along the gradient with the solid curve E_x. In the region $x < 20$ we have small oscillations in space (and time), the accuracy of the curve plotted in this region being degraded by the division by n_i, due to the low density n_i and large ∇T_i appearing close to the surface.

Copyright © 2009. Nova Science Publishers, Inc.. All rights reserved.

Baswell, Albert R.. Advances in Mathematics Research, Nova Science Publishers, Inc., 2009. ProQuest Ebook Central, http://ebookcentral.proquest.com/lib/inflibnet-ebooks/detail.action?docID=3019187.
Created from inflibnet-ebooks on 2018-02-22 20:59:47.

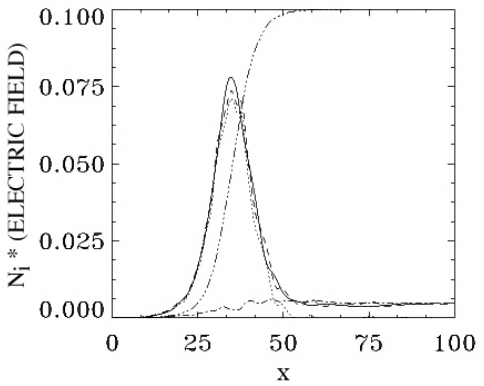

Figure 12. Plot of n_iE_x (solid curve), $+0.1n_i < v_z >$, (dash-dotted curve) , ∇P_i (dotted curve), and $\nabla P_i + 0.1n_i < v_z >$ (broken curve), (n_i/10 is also plotted for reference).

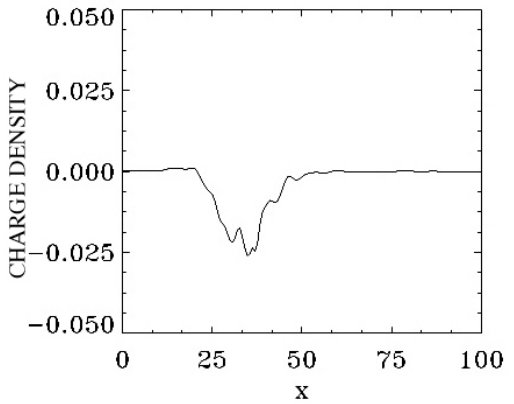

Figure 13. Charge (n_i –n_e).

We plot in Fig. (12) the quantities n_iE_x, ∇P_i, $0.1\,n_i < v_z >$ and the sum $\nabla P_i + 0.1\,n_i < v_z >$. We note that there is a very nice agreement for the relation $n_iE_x = \nabla P_i + 0.1\,n_i < v_z >$ (here the density $n_i/10$ is plotted with the dash-three-dots curve to locate the profiles with respect to the gradient). The electric field should interact with the constant magnetic field to give an $\vec{E}x\vec{B}$ drift in the poloidal direction (there is no shear in this drift in the flat part of the electric field, which can explain the absence of turbulence at the plasma edge observed in H-mode tokamaks). The charge σ appearing in the system is calculated by the code and amounts to –0.34197 at $t = 500$. The charge collected and accumulated at $x = 0$, which defines $E_x\big|_{x=0}$ from Eq. (2.20), is 0.34535. The difference between these two numbers is ≈ 0.00338, which is $E_x\big|_{x=L}$ from Eq. (2.21). We see also from Figs. (11,12) that inside the plasma at the right boundary, in the flat part of the density where $\nabla P_i = 0$, the constant electric field is exactly compensated by the Lorentz force due to

Copyright © 2009. Nova Science Publishers, Inc.. All rights reserved.

Baswell, Albert R.. Advances in Mathematics Research, Nova Science Publishers, Inc., 2009. ProQuest Ebook Central, http://ebookcentral.proquest.com/lib/inflibnet-ebooks/detail.action?docID=3019187.
Created from inflibnet-ebooks on 2018-02-22 20:59:47.

the poloidal drift $0.1 < v_z >$, while along the gradient the electric field is essentially balanced by $\nabla P_i / n_i$ (the electric drift is equal and opposite to the diamagnetic drift). Fig. (13) shows the charge density $(n_i - n_e)$ at $t = 500$, which illustrates how the combined effect of the steep profile at a plasma edge and the large ion orbits (large ratio ρ_i / λ_{De}) leads to a charge separation at a plasma edge along the gradient, when the electrons frozen to the magnetic field cannot move across the field to compensate the charge separation caused by the finite ion gyroradius. Fig. (14) shows the potential. Figs (15) and (16) show the temperatures T_{ix} and T_{iz} (solid curves). The broken lines represent the pressures $n_i T_{ix}$ and $n_i T_{iz}$ which follow closely the curve of the density n_i. Thus close to the floating limiter a complex sheath structure is formed which governs the plasma-wall transition.

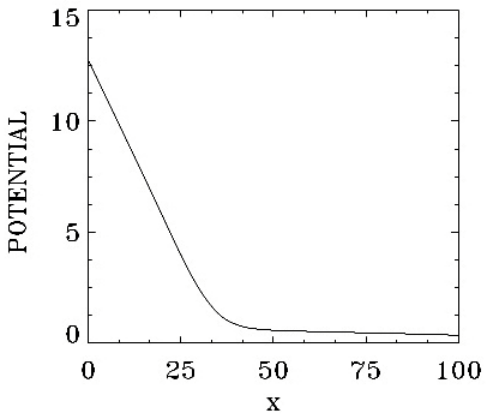

Figure 14. Potential profile.

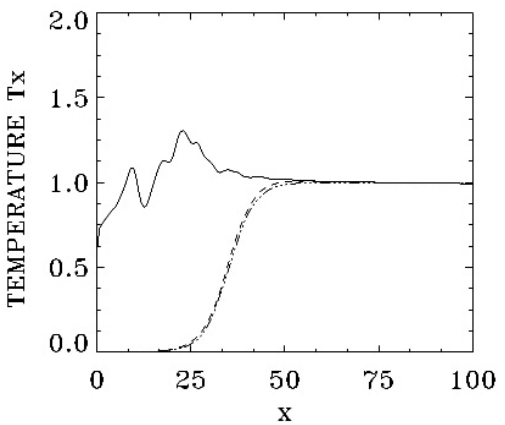

Figure 15. Temperature T_x.

Copyright © 2009. Nova Science Publishers, Inc.. All rights reserved.

Baswell, Albert R.. Advances in Mathematics Research, Nova Science Publishers, Inc., 2009. ProQuest Ebook Central, http://ebookcentral.proquest.com/lib/inflibnet-ebooks/detail.action?docID=3019187.
Created from inflibnet-ebooks on 2018-02-22 20:59:47.

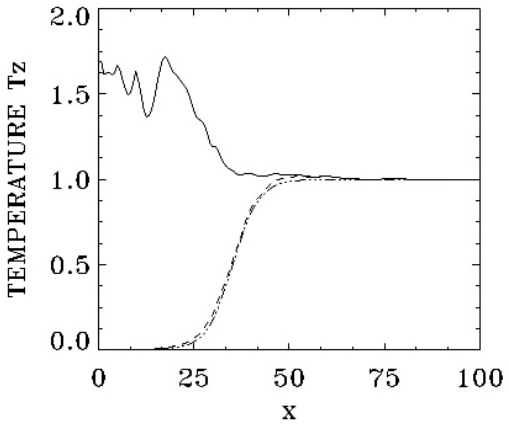

Figure 16. Temperature T_z.

2.3. Vlasov-Maxwell Equations for Laser-Plasma Interaction

Two systems of equations for 1D laser-plasma interaction will be discussed in this chapter. In the first one, presented in this section, we consider a linearly polarized electromagnetic wave [21]. This system is solved using a fractional step method and uses a cubic spline interpolation to solve for the advection term in the reduced one dimensional equations. In the second system, to be presented in section 3.3 a fully relativistic code is used [52], and the wave is circularly polarized. In this case, to advance the equations in time, we shall use a tensor product of cubic *B*-spline for a two dimensional interpolation along the characteristics. Comparison for the results obtained by the two methods will be provided at the end of section 3.3, both from the physical point of view and from the numerical point of view to underline the accuracy of the cubic spline interpolation.

In the model we present in this section, a linear polarization of the electromagnetic wave is assumed. Time t is normalized to the inverse electron plasma frequency ω_{pe}^{-1}, length is normalized to $l_0 = c\omega_{pe}^{-1}$, velocity and momentum are normalized respectively to the velocity of light c and to $M_e c$, where M_e is the electron rest mass. The one-dimensional Vlasov equations for the electron distribution function $f_e(x, p_{xe}, t)$ and the ion distribution function $f_i(x, p_{xi}, t)$ are given by [20]:

$$\frac{\partial f_{e,i}}{\partial t} + m_{e,i} \frac{p_{xe,i}}{(1+(m_{e,i}\, p_{xe,i})^2)^{1/2}} \frac{\partial f_{e,i}}{\partial x} \mp (E_x + v_y^{e,i} B_z) \frac{\partial f_{e,i}}{\partial p_{xe,i}} = 0 . \qquad (2.43)$$

The indices *e* and *i* refers to electrons and ions. In our normalized units $m_e = 1$, for the electrons, and $m_i = M_e / M_i$ for the ions. The relativistic correction in this case is given by

Copyright © 2009. Nova Science Publishers, Inc.. All rights reserved.

Baswell, Albert R.. Advances in Mathematics Research, Nova Science Publishers, Inc., 2009. ProQuest Ebook Central, http://ebookcentral.proquest.com/lib/inflibnet-ebooks/detail.action?docID=3019187.
Created from inflibnet-ebooks on 2018-02-22 20:59:47.

$\gamma_{e,i} = (1 + (m_{e,i} p_{xe,i})^2)^{1/2}$. For the velocity in the direction normal to the gradient, we have the following relation:

$$\frac{\partial v_y^{e,i}}{\partial t} = \mp m_{e,i} E_y . \tag{2.44}$$

The electric field is calculated from the relation $E_x = -\frac{\partial \varphi}{\partial x}$, and the potential φ is calculated from Poisson equation:

$$\frac{\partial^2 \varphi}{\partial x^2} = \int f_e(x, p_{xe}) dp_{xe} - \int f_i(x, p_{xi}) dp_{xi} \tag{2.45}$$

We note also that the canonical momentum $P_y = v_y^{e,i} / m_{e,i} \mp a_y = 0$. Hence $v_y^{e,i} = \pm m_{e,i} a_y$, which when derived with respect to time leads to Eq.(2.44) ($E_y = -\partial a_y / \partial t$). $a_y = eA_y / M_e c$ is the normalized *y* component of the vector potential. The linearly polarized electromagnetic field propagates in the *x* direction with an electric field E_y in the *y* direction, normalized to $\omega_{pe} M_e c / e$, and a magnetic field $B_z = \partial a_y / \partial x$ in the *z* direction, normalized to $\omega_{pe} M_e / e$. We define the quantity $E^{\pm} = E_y \pm B_z$, which obeys the equation:

$$(\frac{\partial}{\partial t} \pm \frac{\partial}{\partial x}) E^{\pm} = -J_y = v_y^e \int f_e(x, p_{xe}, t) dp_{xe} - v_y^i \int f_i(x, p_{xi}, t) dp_{xi} = v_y^e n_e - v_y^i n_i . \tag{2.46}$$

The Hamiltonian associated with this system is given by:

$$H_{e,i} = \frac{1}{m_{e,i}} \left(1 + (m_{e,i} p_{xe,i})^2\right)^{1/2} \pm \varphi + \frac{1}{2} m_{e,i} A_y^2 . \tag{2.47}$$

We can write Eq.(2.43) in the form: $\frac{\partial f_{e,i}}{\partial t} + \left[H_{e,i}, f_{e,i}\right] = 0$, where the Poisson bracket:

$$\left[H_{e,i}, f_{e,i}\right] = \frac{\partial H_{e,i}}{\partial p_{xe,i}} \frac{\partial f_{e,i}}{\partial x} - \frac{\partial H_{e,i}}{\partial x} \frac{\partial f_{e,i}}{\partial p_{xe,i}} . \tag{2.48}$$

Eqs.(2.43) are solved by a fractional step [20]. The momentum space is divided into N_p cells between $-p_{x\max e,i}$ and $+p_{x\max e,i}$. The length *L* of the system is divided into N_x cells.

Copyright © 2009. Nova Science Publishers, Inc.. All rights reserved.

Baswell, Albert R.. Advances in Mathematics Research, Nova Science Publishers, Inc., 2009. ProQuest Ebook Central, http://ebookcentral.proquest.com/lib/inflibnet-ebooks/detail.action?docID=3019187.
Created from inflibnet-ebooks on 2018-02-22 20:59:47.

The fractional step method involves the following steps to advance Eq.(2.43) in time from t_n to t_{n+1} :

Step1- For a time step $\Delta t/2$, we calculate

$$f_{e,i}^{*}(x, p_{xe,i}, t_{n+1/2}) = f_{e,i}(x-(m_{e,i}p_{xe,i}/\gamma_{e,i})\Delta t/2, p_{xe,i}, t_n). \quad (2.49)$$

Step2- Calculate the fields at time $t_{n+1/2}$ using $f_{e,i}^{*}$, then use these values to shift for Δt in the direction $p_{xe,i}$ the distribution functions:

$$f_{e,i}^{**}(x, p_{xe,i}, t_{n+1/2}) = f_{e,i}^{*}(x, p_{xe,i} \pm (E_x^{n+1/2} + v_y^{e,in+1/2}B_z^{n+1/2})\Delta t, t_{n+1/2}). \quad (2.50)$$

Step3- Shift again for a time step $\Delta t/2$ in x space:

$$f_{e,i}(x, p_{xe,i}, t_{n+1}) = f_{e,i}^{**}(x-(m_{e,i}p_{xe,i}/\gamma_{e,i})\Delta t/2, p_{xe,i}, t_n). \quad (2.51)$$

The shifts in Eqs.(2.49-2.51) are done using cubic spline interpolation (see Appendix B). The solution of Eq.(2.44) between t_n and t_{n+1} is given by the time centered scheme:

$$v_y^{e,i}(x, t_{n+1}) = v_y^{e,i}(x, t_n) \mp \Delta t \frac{E^{+}(x, t_{n+1/2}) - E^{-}(x, t_{n+1/2})}{2}. \quad (2.52)$$

Eqs.(2.46) are solved using the centered scheme with $\Delta x = \Delta t$:

$$E^{\pm}(x \pm \Delta t, t_{n+1/2}) = E^{\pm}(x, t_{n-1/2}) - \Delta t J_y(x \pm \Delta t/2, t_n). \quad (2.53)$$

with $$J_y(x \pm \Delta t/2, t_n) = \frac{J_y(x \pm \Delta x, t_n) + J_y(x, t_n)}{2}.$$

We integrate exactly along the vacuum characteristic with $\Delta x = \Delta t$, we can write the following numerical scheme for Eq.(2.53):

$$\begin{aligned} E^{\pm}(x, t_{n+1/2}) = E^{\pm}(x \mp \Delta x, t_{n-1/2}) + \frac{1}{2}\Delta t(n_e(x, t_{n+1/2})v_y^e(x, t_n) + \\ n_e(x \mp \Delta x, t_{n-1/2})v_y^e(x \mp \Delta x, t_n) - n_i(x, t_{n+1/2})v_y^i(x, t_n) + \\ n_i(x \mp \Delta x, t_{n-1/2})v_y^i(x \mp \Delta x, t_n)) \end{aligned} \quad (2.54)$$

The calculation of $E_x^{n+1/2}$ is done by discretizing Eq.(2.45) using a tridiagonal matrix similar to Eq.(2.12). The solution of Eq.(2.45) in a finite domain require boundary conditions.

Copyright © 2009. Nova Science Publishers, Inc.. All rights reserved.

Baswell, Albert R.. Advances in Mathematics Research, Nova Science Publishers, Inc., 2009. ProQuest Ebook Central, http://ebookcentral.proquest.com/lib/inflibnet-ebooks/detail.action?docID=3019187.
Created from inflibnet-ebooks on 2018-02-22 20:59:47.

The system is initially neutral. If a charge Q_p appears in the system, it has to disappear through the boundaries. A first approximation used in [21] was to divide this charge equally between the two (left and right) boundaries. A more accurate calculation consists in calculating the charge at the two boundaries by collecting the current hitting these boundaries. Let us assume that Q_l, Q_p, and Q_r are the charges calculated during the simulation respectively at the left boundary, in the plasma, and at the right boundary. Q_l can be calculated by collecting the current at the left boundary from the relation :

$$\left.\frac{\partial E_x}{\partial t}\right|_{x=0} = -J_x\big|_{x=0} = -\left(J_{xi} - J_{xe}\right)\big|_{x=0}. \tag{2.55}$$

From which :
$$E_x\big|_{x=0} = -\int_0^t J_x\big|_{x=0} dt = Q_l. \tag{2.56}$$

and
$$J_{xe,i}\big|_{x=0} = m_{e,i}\int_{-\infty}^{0} \frac{p_{xe,i}}{\gamma_{e,i}} f_{e,i}(0, p_{xe,i}, t) dp_{xe,i}$$

and a similar expression at the right boundary: $E_x\big|_{x=L} = -\int_0^t J_x\big|_{x=L} dt = Q_r$. (2.57)

and
$$J_{xe,i}\big|_{x=L} = m_{e,i}\int_{0}^{\infty} \frac{p_{xe,i}}{\gamma_{e,i}} f_{e,i}(L, p_{xe,i}, t) dp_{xe,i}$$

Integrating Eq.(2.45) over the domain $(0, L)$, we get :

$$E_x\big|_{x=L} - E_x\big|_{x=0} = \int_0^L (n_i - n_e) dx = Q_p \tag{2.58}$$

where Q_p is the charge appearing in the plasma. The charge appearing at the right boundary is $Q_r = E_x\big|_{x=L}$, and the charge appearing at the left boundary is $Q_l = E_x\big|_{x=0}$. Eq.(2.58) is also written $Q_l + Q_p - Q_r = 0$. This relation is usually verified by the code. To take into account any imbalance in this relation, let us consider the electric field $E_x(x = x_0)$ at a point x_0 far to the left of the simulation box and boundaries. The electric field is the sum of the fields from Q_l, Q_p, and Q_r. Since a plate of charge q gives an electric field $E_x = q/2$

Copyright © 2009. Nova Science Publishers, Inc.. All rights reserved.

Baswell, Albert R.. Advances in Mathematics Research, Nova Science Publishers, Inc., 2009. ProQuest Ebook Central, http://ebookcentral.proquest.com/lib/inflibnet-ebooks/detail.action?docID=3019187.
Created from inflibnet-ebooks on 2018-02-22 20:59:47.

for a point to the right of the plate (and $E_x = -q/2$ for a point to the left), we can write with the convention of signs in Eq.(2.58) [53]:

$$E_x(x_0) = (-Q_l - Q_p + Q_r)/2. \tag{2.59}$$

Now if we move from $x = x_0$ to $x = 0_+$, just inside the left boundary, Q_l is now to our left, so it will contribute to the field by $Q_l/2$ instead of $-Q_l/2$, and the electric field is now given by:

$$E_x(x = 0_+) = (Q_l - Q_p + Q_r)/2. \tag{2.60}$$

This is the boundary condition used in [53]. Now consider the case when the charges are exactly balanced in the system, then as we mentioned before $Q_l + Q_p - Q_r = 0$, or $Q_p = Q_r - Q_l$, and substituting in Eq.(2.60), we get $E_x(x = 0) = Q_l$, which is the result in Eq.(2.56).

Finally we note that the pump wave is penetrating the plasma at the left boundary at *x*=0 where we set $E^+(x = 0) = 2E_0 \sin(\omega_0 t)$, $E^-(x = 0) = 0$, for the solution of Eqs.(2.53) . The normalized wave amplitude $E_0 = E_{am} e/(\omega_{epw} M_e c) \equiv \dfrac{V_{osc}/c}{\sqrt{n/n_c}}$, where E_{am} is the wave amplitude and n_c the critical density. This value of E_0 can also be written $E_0 = (0.00854265\lambda\sqrt{I0})/\sqrt{n/n_c}$. We use the parameters of [53], where $\lambda = 0.527\mu m$ for the laser, and n/n_c =0.032, and the intensity *I*0=100 (in units of 10^{14} W/cm^2). This results in $E_0 = 0.25$.

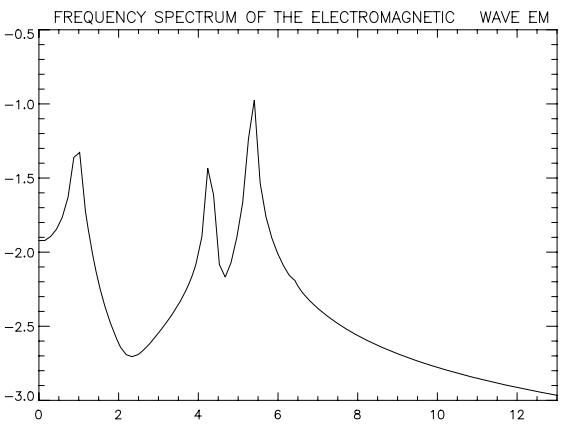

Figure 17. Frequency spectrum of E^+.

Copyright © 2009. Nova Science Publishers, Inc.. All rights reserved.

Baswell, Albert R.. Advances in Mathematics Research, Nova Science Publishers, Inc., 2009. ProQuest Ebook Central, http://ebookcentral.proquest.com/lib/inflibnet-ebooks/detail.action?docID=3019187.
Created from inflibnet-ebooks on 2018-02-22 20:59:47.

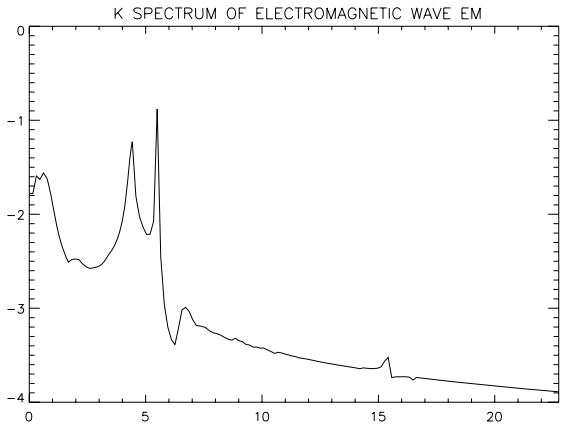

Figure 18. Wavenumber spectrum of E^+.

We use again the same parameters as in [53]. The laser pump is $\omega_0 = 5.59\omega_{pe}$ and the laser wavenumber is $k_0 = 5.5(\omega_{pe}/c)$. For the scattered mode we have $\omega_{SRS} = 4.478\omega_{pe}$ and $k_{SRS} = 4.4(\omega_{pe}/c)$. For the plasma wave we have $\omega_{epw} = 1.1124\omega_{pe}$, and $k_{epw} = 9.86(\omega_{pe}/c)$. The electron thermal velocity is $v_{Te} = 0.026c$, $T_e/T_i = 3.5$. The length of the system is $L = 50.265$, and $N_x = 5000$ grid points in space, $N_v = 256$ grid points in velocity space for electrons and 128 for ions. $\Delta x = \Delta t = 0.0105$. We show in Fig.(17) the results obtained for the frequency spectrum of the electromagnetic field E^+ at the position x=5 at t=60. We can identify the contribution of the pump and scattered mode at ω_0 and ω_{SRS}. Fig.(18) shows the wavenumber spectrum for E^+ at t=60, where again we

Copyright © 2009. Nova Science Publishers, Inc.. All rights reserved.

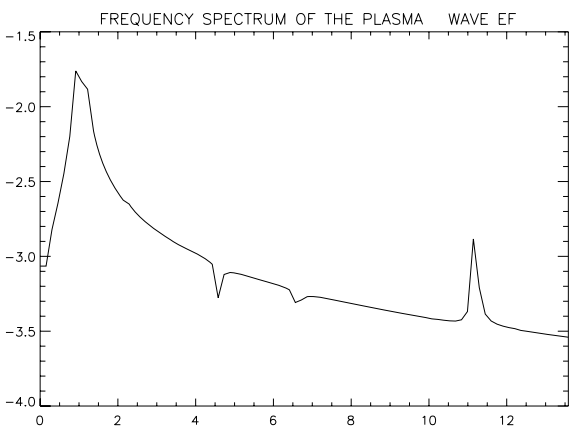

Figure 19. Frequency spectrum for the plasma wave.

Baswell, Albert R.. Advances in Mathematics Research, Nova Science Publishers, Inc., 2009. ProQuest Ebook Central, http://ebookcentral.proquest.com/lib/inflibnet-ebooks/detail.action?docID=3019187.
Created from inflibnet-ebooks on 2018-02-22 20:59:47.

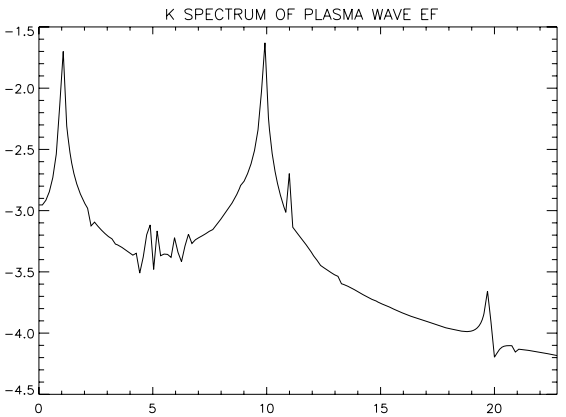

Figure 20. Wavenumber spectrum for the plasma wave.

can identify the contribution of the laser pump $k_0 = 5.5(\omega_{pe}/c)$ and the scattered mode at $k_{SRS} = 4.4(\omega_{pe}/c)$. Fig.(19) shows the frequency spectrum of the plasma wave showing the $\omega_{epw} = 1.1124\omega_{pe}$ peak and a peak at $\omega_h = 11.18\omega_{pe}$, *i.e.* the harmonic of the pump wave ω_0. We can identify in Fig.(20) the wavenumber peak at $k_{epw} = 9.86(\omega_{pe}/c)$ for the plasma wave, followed by a small neighbouring peak at $k_h = 11(\omega_{pe}/c)$, *i.e.* the harmonic of the pump wave k_0. The harmonic peaks at k_h and ω_h in Fig.(19) and (20) result from the $v_y B_z$ term in Eq.(2.43). This can also be verified in the results in Fig.(7) of [54] where we see the response of the plasma at the harmonic of the electromagnetic wave frequency, when using a model similar to what has been presented in this section and in Eq.(2.43) applied to the problem of inductive coupling. Indeed, if we assume a linearly polarized wave: $\vec{E} = (0, E_y, 0)$, we can write in a linear analysis $E_y = E_0 \cos(\psi)$, $\psi = (k_0 x - \omega_0 t)$. Faraday's law is:

$$\frac{\partial \vec{B}}{\partial t} = (0,0,-\frac{\partial E_y}{\partial x}). \tag{2.61}$$

Then $\vec{B} = (0,0,B_z)$ with $B_z = B_0 \cos(\psi)$, and $B_0 = E_0 k_0 / \omega_0$. Also from Eq.(2.44) $\vec{v} = (0, v_y, 0)$ with $v_y = -v_0 \sin(\psi)$, and $v_0 = E_0 / \omega_0$. The longitudinal Lorentz force $v_y B_z = -\frac{1}{2} k_0 v_0^2 \sin(2\psi)$. This drive a longitudinal response at the 2nd harmonic of the light wave.

Copyright © 2009. Nova Science Publishers, Inc.. All rights reserved.

Baswell, Albert R.. Advances in Mathematics Research, Nova Science Publishers, Inc., 2009. ProQuest Ebook Central, http://ebookcentral.proquest.com/lib/inflibnet-ebooks/detail.action?docID=3019187.
Created from inflibnet-ebooks on 2018-02-22 20:59:47.

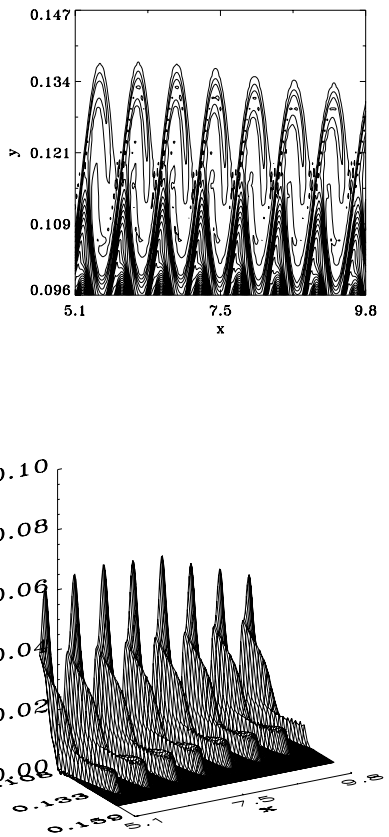

Figure 21. Contour plot and 3D view for the phase-space of the distribution function from x=5.1 to x=9.8 at $t = 60\omega_{pe}^{-1}$.

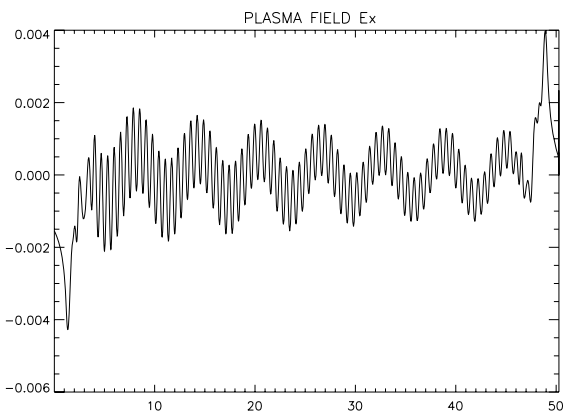

Figure 22. Longitudinal electric field.

Copyright © 2009. Nova Science Publishers, Inc.. All rights reserved.

Baswell, Albert R.. Advances in Mathematics Research, Nova Science Publishers, Inc., 2009. ProQuest Ebook Central, http://ebookcentral.proquest.com/lib/inflibnet-ebooks/detail.action?docID=3019187.
Created from inflibnet-ebooks on 2018-02-22 20:59:47.

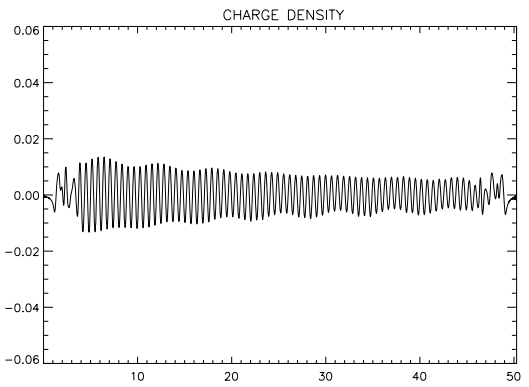

Figure 23. Charge (n_i–n_e).

Fig.(21) shows the phase-space structure in contour plot and 3D view of the tail of the electron distribution function between x= 5.1 and x=9.8 at t=60. Note the clear structure of the vortices in Fig.(21), in the low density regions of the phase-space, without numerical noise Fig.(22) shows the electric field E_x at t=60 across the simulation box, and Fig.(23) shows the charge ($n_i - n_e$). We note the system is solved for ions and electrons, but the response of the ions at t=60 is still negligible. In the conclusion of this section 2 , we stress the importance of the cubic spline and the good performance of the interpolation technique, having low numerical diffusion and dispersion and high accuracy. We also note the numerical stability of the numerical code.

3. Problems Involving the Interpolation along the Characteristic Curves in Two Dimensions

The problems studied in section 2 for the Vlasov equation dealt essentially with the fractional step methods where the interpolation along the characteristic curves was carried out in 1D using a cubic spline. We present in this section examples where the interpolation along the characteristic curves is carried in two dimensions , using a tensor product of cubic *B*-splines . The integration along the characteristics in higher dimensions applied to Eulerian Vlasov codes has been formulated sometime ago in [15,16], and only recently applied [6,9]. The first example we present in this section is the solution of the guiding-center equations in 2D (which are the equations of a plasma in a strong magnetic field) to study the Kelvin-Helmholtz instabilities. These equations are isomorphic with the Euler equations that govern 2D inviscid incompressible fluids in hydrodynamics [55-60]. We use this example to introduce in section 3.1 the methods of 2D interpolation discussed in section 1 and in [6,9]. In section 3.2 we will reconsider the problem of the formation of an electric field at a plasma edge, presented in section 2.2 , however we use this time a cylindrical geometry in the Vlasov equation. We will consider next in section 3.3 a case of laser-plasma interaction similar to what has been presented in section 2.3 , treated however with a circularly polarized wave and a fully relativistic Vlasov equation. The results obtained in this section will be compared both from the physical point of view as well as from the numerical point of view with the corresponding

Copyright © 2009. Nova Science Publishers, Inc.. All rights reserved.

Baswell, Albert R.. Advances in Mathematics Research, Nova Science Publishers, Inc., 2009. ProQuest Ebook Central, http://ebookcentral.proquest.com/lib/inflibnet-ebooks/detail.action?docID=3019187.
Created from inflibnet-ebooks on 2018-02-22 20:59:47.

results in sections 2.2 and 2.3, especially concerning the accuracy of the results and of the numerical techniques using cubic spline interpolation. Finally the problem of solving a reduced set of magnetohydrodynamic equations to study the problem of magnetic reconnection will be presented in section 3.4.

3.1. Solution of the Guiding-Center or Euler Equations

In the two-dimensional space $\mathbf{r} = (x, y)$, the evolution of a plasma in a strong magnetic field [55-60] $\mathbf{B} = B\mathbf{e}_z$ is governed by the guiding center equation :

$$\frac{\partial \rho}{\partial t} + \mathbf{V}_D . \frac{\partial \rho}{\partial \mathbf{r}} = 0 . \tag{3.1}$$

with the drift or guiding-center velocity $\mathbf{V}_D = \mathbf{e}_z \times \frac{\partial \phi}{\partial \mathbf{r}}$, $\mathbf{E} = -\frac{\partial \phi}{\partial \mathbf{r}}$, and ϕ is calculated from Poisson equation:

$$\Delta \phi = -\rho \tag{3.2}$$

The initial condition for the charge density is $\rho(\mathbf{r}, t = 0) = \rho_0(\mathbf{r})$. Eqs.(3.1) and (3.2) are isomorphic to the Euler equations that govern 2D inviscid incompressible fluids in hydrodynamics, where the charge density corresponds to the flow vorticity, and the potential ϕ corresponds to the stream function [57]. For a plasma in a strong magnetic field, the particle motion along the magnetic field B and across the magnetic field B are decoupled, the velocity perpendicular to the magnetic field is the guiding-center velocity $\mathbf{V}_D$ and the Vlasov equation can be reduced to the guiding-center plasma model in Eqs(3.1-3.2). These equations are also the simplest form for the gyro-kinetic or drift-kinetic Vlasov equation, when the kinetic motion along the magnetic field is taken into account and is coupled to the guiding-center motion across the magnetic field, as for instance in the case when the magnetic field is slightly tilted with respect to $\mathbf{e}_z$ [32-38,61]. The system in Eqs.(3.1-3.2) is solved on a rectangular domain $L_x \times L_y$. Periodic boundary conditions are used in the *y* direction, and Dirichlet boundary conditions are used in the *x* direction with $\phi(x = 0, L_x, y) = 0$, $\rho(x = 0, L_x, y) = 0$. Following the steps of what has been presented in Eqs.(1.8-1.14), Eq.(3.1) can be integrated along the characteristic curves given by the solution of the equations:

$$\frac{d\mathbf{r}}{dt} = \mathbf{V}_D(\mathbf{r}, t) . \tag{3.3}$$

Copyright © 2009. Nova Science Publishers, Inc.. All rights reserved.

Baswell, Albert R.. Advances in Mathematics Research, Nova Science Publishers, Inc., 2009. ProQuest Ebook Central, http://ebookcentral.proquest.com/lib/inflibnet-ebooks/detail.action?docID=3019187.
Created from inflibnet-ebooks on 2018-02-22 20:59:47.

We write that the value of ρ along the characteristic curves is constant (see Eq.(1.11)):

$$\rho(\mathbf{r}, t_{n+1}) = \rho\big(\mathbf{r}(t_{n-1}), t_{n-1}\big). \tag{3.4}$$

We assume the value of $\mathbf{r}(t = t_{n+1}) = \mathbf{r_i}$, where the $\mathbf{r_i}$ are grid points. A numerical scheme accurate to second order in Δt for the solution of Eq.(3.3) is given by the following leapfrog scheme (similar to Eq.(1.12)):

$$\frac{\mathbf{r_i} - \mathbf{r}(t_{n-1})}{2\Delta t} = \mathbf{V}_D^n\left(\frac{\mathbf{r_i} + \mathbf{r}(t_{n-1})}{2}\right). \tag{3.5}$$

where $\mathbf{V}_D^n = \mathbf{e}_z \times \dfrac{\partial \phi(\mathbf{r}, t_n)}{\partial \mathbf{r}}$, and $\mathbf{E}(\mathbf{r}, t_n)$ is computed by solving Poisson equation for $\rho(\mathbf{r}, t_n)$ at $t = t_n$. To solve Eq.(3.2), we Fourier transform this equation in the periodic *y* direction. We denote by ρ_{k_y} and ϕ_{k_y} the Fourier transform of ρ and ϕ in the periodic *y* direction. We have:

$$\phi(x, y) = \sum_{k_y} e^{ik_y y}\phi_{k_y}(x); \quad \rho(x, y) = \sum_{k_y} e^{ik_y y}\rho_{k_y}(x)$$

Which by substituting in Eq.(3.2) gives the following result:

$$\frac{\partial^2 \phi_{k_y}(x)}{\partial x^2} - k_y^2 \phi_{k_y}(x) = -\rho_{k_y}(x). \tag{3.6}$$

We can derive the following tridiagonal matrix by discretizing Eq.(3.6) in the *x* direction [61]:

$$(1 - C_{k_y})\phi_{k_y i+1} - (+2 + 10C_{k_y})\phi_{k_y i} + (1 - C_{k_y})\phi_{k_y i-1} = -\frac{\Delta x^2}{12}(\rho_{k_y i-1} + 10\rho_{k_y i} + \rho_{k_y i+1}). \tag{3.7}$$

where $C_{k_y} = \dfrac{k_y^2 \Delta x^2}{12}$. The tridiagonal matrix in Eq.(3.7) is solved with Dirichlet boundary conditions for ϕ_{k_y}, which is then Fourier transformed back to get ϕ. Again the implicit equation in Eq.(3.5) is solved by iteration as in Eq.(1.13), to calculate $\Delta_{\mathbf{r}} = (\mathbf{r_i} - \mathbf{r}(t_{n-1}))/2$ as follows:,

$$\Delta_{\mathbf{r}}^{k+1} = \Delta t \mathbf{V}_D(\mathbf{r_i} - \Delta_{\mathbf{r}}^k, t_n).$$

Copyright © 2009. Nova Science Publishers, Inc.. All rights reserved.

Baswell, Albert R.. Advances in Mathematics Research, Nova Science Publishers, Inc., 2009. ProQuest Ebook Central, http://ebookcentral.proquest.com/lib/inflibnet-ebooks/detail.action?docID=3019187.
Created from inflibnet-ebooks on 2018-02-22 20:59:47.

From Eqs.(1.14) and (3.4) the new value $\rho(\mathbf{r_i}, t_{n+1})$ is calculated from the relation:

$$\rho(\mathbf{r_i}, t_n + \Delta t) = \rho(\mathbf{r_i} - 2 * \Delta_{\mathbf{r}}, t_n - \Delta t). \tag{3.8}$$

More explicitly we have to calculate (see Fig.(1)) $\rho(x_i - 2\Delta_x, y_j - 2\Delta_y, t_n - \Delta t)$, where Δ_x and Δ_y are obtained by iteration by solving :

$$\Delta_x^{k+1} = \Delta t V_{Dx}(x_i - \Delta_x^k, y_j - \Delta_y^k, t_n) \tag{3.9}$$

$$\Delta_y^{k+1} = \Delta t V_{Dy}(x_i - \Delta_x^k, y_j - \Delta_y^k, t_n) \tag{3.10}$$

where $V_{Dy} = \dfrac{\partial \phi}{\partial x}$; $V_{Dx} = -\dfrac{\partial \phi}{\partial y}$. We start with $\Delta_x^0 = 0$, $\Delta_y^0 = 0$. Usually two or three iterations are sufficient for convergence. The interpolations in Eqs.(3.8-3.10) are carried out using a 2D cubic *B*-splines defined as a tensor product of one dimensional cubic *B*-splines. We first evaluate the coefficients η_{ij} from the values of the function at grid points (details can be found in [6], we have however to introduce appropriate modification to the boundary condition in the direction *y*, to take into account the periodic boundary condition as in [51]):

$$\rho(x_i, y_j) = \sum_{i=0}^{N_x} \sum_{j=0}^{N_y} \eta_{ij} B_i(x) B_j(y). \tag{3.11}$$

The cubic *B*-spline has been defined in Appendix C . Eq.(3.11) generalizes to two dimensions the results presented in Appendix C. Then the value of the function at interstitial points $\rho(x_i + \Delta_x, y_j + \Delta_y)$ is given by:

$$\rho(x_i + \Delta_x, y_j + \Delta_y) = \sum_{\kappa=0}^{3} \sum_{l=0}^{3} \eta_{i-\kappa, j-l} b_\kappa^x b_l^y. \tag{3.12}$$

where $i \equiv x_i$, $\Delta_x = x - x_i$, and $j \equiv y_j$, $\Delta_y = y - y_j$, b_κ^x are defined in Appendix C, and a similar definition holds for b_l^y by substituting Δ_y for Δ_x in the expression of b_κ^x. We finally note that in [9], in order to accelerate the calculation, a linear interpolation has been used in the intermediate step in Eqs. (3.9-3.10). This turned out however to introduce strong numerical diffusion [43,44].

We apply the previously described numerical method to study the stability of a sinusoidal profile [58,59]. Any function of one space variable is an equilibrium solution to Eqs(3.1-3.2). We consider the sinusoidal profile $\rho_0 = \sin(x)$. From Eq.(3.2) the self-consistent potential

Copyright © 2009. Nova Science Publishers, Inc.. All rights reserved.

Baswell, Albert R.. Advances in Mathematics Research, Nova Science Publishers, Inc., 2009. ProQuest Ebook Central, http://ebookcentral.proquest.com/lib/inflibnet-ebooks/detail.action?docID=3019187.
Created from inflibnet-ebooks on 2018-02-22 20:59:47.

is given by $\phi_0 = \sin(x)$. A necessary condition for the flow $V_{D0} = \frac{\partial \phi_0}{\partial x} = \cos(x)$ to have an unstable growing solution is that this flow should have a point of inflexion. This is the Rayleigh necessary condition for instability. This instability due to the shear in the velocity flow is called Kelvin-Helmholtz instability. Furthermore if the equilibrium is perturbed with a perturbation of the form $e^{-i(\omega t + k_y y)}$, $k_y = 2\pi / L_y$, there exists an eigensolution with real values of ω such that $\frac{\omega}{k_y} = V_D(x_s)$ (the so-called neutrally stable eigensolution), where x_s is the point of inflexion, and one can construct unstable solutions for which $\frac{\omega}{k_y} \to V_D(x_s)$ as the imaginary part of ω tends to zero through positive values. In the present case, we consider a domain with $L_x = 2\pi$, and $L_y = 10$. We use $N_x = N_y = 256$ and $\Delta t = 0.005$. In the domain $0 \le x \le 2\pi$ where the equilibrium flow is defined we have two points of inflexion located at $x_s = \pi/2$ and $x_s = 3\pi/2$. At these points $\frac{\omega}{k_y} = V_D(x_s) = \cos(x_s) = 0$. In this case $\omega = \omega_s = 0$, and a neutrally stable solution satisfying the boundary conditions of zero at $x = 0$ and $x = 2\pi$ is given by [58,59] :

$$\phi_s = \sin(\frac{x}{2}) .; \tag{3.13}$$

$$k_{ys} = \frac{\sqrt{3}}{2} \tag{3.14}$$

We perturb the equilibrium ρ_0 as follows:

$$\rho_0 = \sin(x) + \varepsilon \sin(\frac{x}{2}) \cos(k_y y) . \tag{3.15}$$

with $k_y = 2\pi / L_y = 0.628$, and $\varepsilon = 0.015$. Since we are close to a neutrally stable solution, we can use a Taylor expansion to calculate the growth rate of the instability:

$$\frac{\omega}{k_y} = \left.\frac{\omega}{k_y}\right|_{\omega_s, k_{ys}} + (k_y - k_{ys}) \frac{\partial}{\partial k_y} \left(\frac{\omega}{k_y}\right)_{\omega_s, k_{ys}} . \tag{3.16}$$

Details of these calculations have been presented in [58,59], and lead to the following result for the real and imaginary parts of ω :

Copyright © 2009. Nova Science Publishers, Inc.. All rights reserved.

Baswell, Albert R.. Advances in Mathematics Research, Nova Science Publishers, Inc., 2009. ProQuest Ebook Central, http://ebookcentral.proquest.com/lib/inflibnet-ebooks/detail.action?docID=3019187.
Created from inflibnet-ebooks on 2018-02-22 20:59:47.

$$\frac{\mathrm{Re}\,\omega}{k_y} = \frac{\sqrt{3}}{2}(k_{ys} - k_y)\,. \tag{3.17}$$

$$\frac{\mathrm{Im}\,\omega}{k_y} = \frac{\sqrt{3}}{2}(k_{ys} - k_y)\,. \tag{3.18}$$

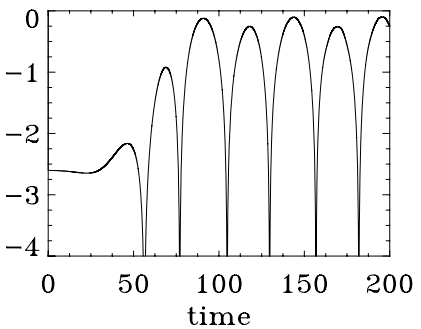

Figure 24. Growth and saturation of the potential at the position $x=3L_x/4$.

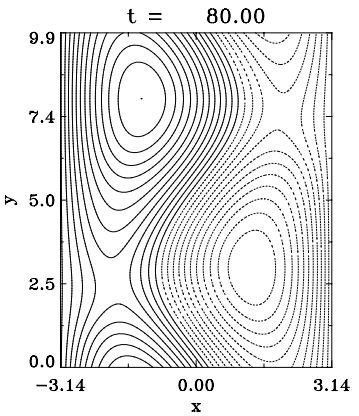

Figure 25. Contour plot of the potential at $t=80$.

In this case $k_y < k_{ys}$, and the system is unstable [58,59]. From Eq.(3.17), the phase velocity $\frac{\mathrm{Re}\,\omega}{k_y}$ is equal to 0.2058. We do verify by following the center of the vortex in Figs(25-26) that the phase velocity of the vortex is indeed 0.2 . Fig.(24) shows the growth and oscillation of the potential , monitored at the position $x = 3L_x/4;\ \ y = 0$. The theoretical results from Eqs(3.17-3.18) show $\mathrm{Im}\,\omega = \mathrm{Re}\,\omega = 0.129$, in good agreement with the observations taken from the results of Figs.(24), which shows a growth and an oscillation period of 0.124. Figs(25-26) shows the contour plot of the potential at $t=80$ and 120 during the saturation phase, and the corresponding charge is given in Figs.(27-28) (dotted curves denote negative values). Note the very nice agreement of the theoretical and numerical results.

Copyright © 2009. Nova Science Publishers, Inc.. All rights reserved.

Baswell, Albert R.. Advances in Mathematics Research, Nova Science Publishers, Inc., 2009. ProQuest Ebook Central, http://ebookcentral.proquest.com/lib/inflibnet-ebooks/detail.action?docID=3019187.
Created from inflibnet-ebooks on 2018-02-22 20:59:47.

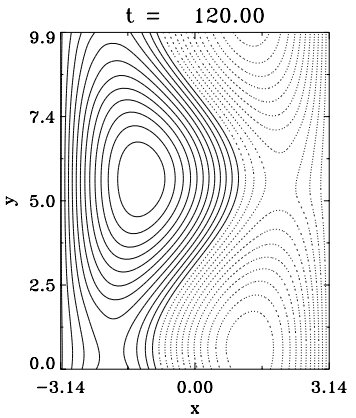

Figure 26. Contour plot of the potential at t=120.

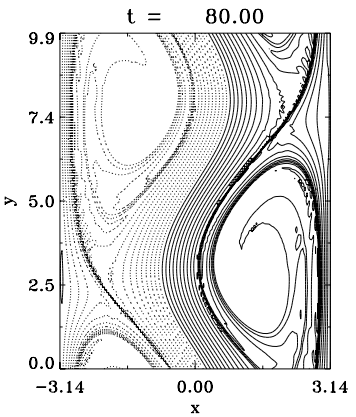

Figure 27. Contour plot of the charge at t=80.

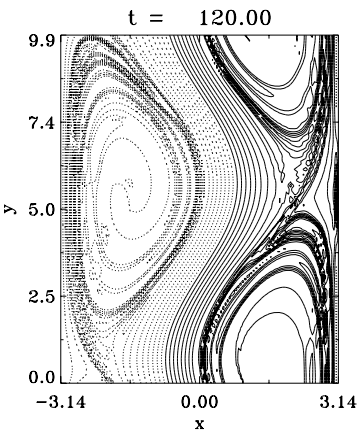

Figure 28. Contour plot of the charge at t=80.

Copyright © 2009. Nova Science Publishers, Inc.. All rights reserved.

Baswell, Albert R.. Advances in Mathematics Research, Nova Science Publishers, Inc., 2009. ProQuest Ebook Central, http://ebookcentral.proquest.com/lib/inflibnet-ebooks/detail.action?docID=3019187.
Created from inflibnet-ebooks on 2018-02-22 20:59:47.

3.2. The Vlasov-Poisson System in Higher Phase-Space Dimensions: Formation of an Electric Field at a Plasma edge in a Cylindrical Geometry

We will discuss in this section, using cylindrical geometry, the problem of the formation of an electric field at a plasma edge which has been studied in section 2.2 using a slab geometry. In cylindrical geometry, it is more convenient to use a tensor product of cubic *B*-spline to interpolate in 2D velocity space, while in section 2.2 we applied a fractional step associated with 1D cubic spline interpolation. Hence we have the opportunity to compare two completely different codes, and to evaluate the performance of the cubic spline for the solution of the same problem. In the present cylindrical geometry, the external magnetic field is in the *z* direction, and (r,θ) is the poloidal plane. The plasma is assumed uniform in the *z* and θ directions. Electrons are magnetized along the magnetic field, and consequently have a constant profile. The Vlasov and Poisson equations are written for the deuterons distribution function $f_i(r, v_r, v_\theta, t)$ and for the potential $\varphi(r)$ with the same normalization and parameters as in section 2.2, as follows (see [6]):

$$\frac{\partial f_i}{\partial t}+v_r\frac{\partial f_i}{\partial r}+\left[E_r+v_\theta\omega_{ci}+\frac{v_\theta^2}{r}\right]\frac{\partial f_i}{\partial v_r}-\left(\omega_{ci}v_r+\frac{v_r v_\theta}{r}\right)\frac{\partial f_i}{\partial v_\theta}=0 \tag{3.19}$$

$$E_r=-\frac{\partial\phi}{\partial r};\qquad \frac{1}{r}\frac{\partial}{\partial r}r\frac{\partial\phi}{\partial r}=-(n_i-n_e)\ ;\ n_i=\int f_i\ dv_r\ dv_\theta \tag{3.20}$$

We advance Eq. (3.19) for a time step Δt as follows:

Step1-We solve for a time step $\Delta t/2$, using cubic spline interpolation, the equation:

$$\frac{\partial f_i}{\partial t}+v_r\frac{\partial f_i}{\partial r}=0 \tag{3.21}$$

the solution is given by $f_i^*(r, v_r, v_\theta, t+\Delta t/2)=f_i^n(r-v_r\Delta t/2, v_r, v_\theta, t)$ (3.22)

We calculate the shift in Eq.(3.22) using 1D cubic spline interpolation as discussed before. We then solve Poisson equation in Eq.(3.20) to calculate the electric field E_r^*.

Step2-We solve next for a time step Δt the equation:

$$\frac{\partial f_i}{\partial t}+\left[E_r^*+v_\theta\omega_{ci}+\frac{v_\theta^2}{r}\right]\frac{\partial f_i}{\partial v_r}-\left(\omega_{ci}v_r+\frac{v_r v_\theta}{r}\right)\frac{\partial f_i}{\partial v_\theta}=0 \tag{3.23}$$

Splitting Eq.(3.23) is not straightforward as in Cartesian geometry. This equation is solved using 2D interpolation. The characteristics of this equation are given by:

Copyright © 2009. Nova Science Publishers, Inc.. All rights reserved.

Baswell, Albert R.. Advances in Mathematics Research, Nova Science Publishers, Inc., 2009. ProQuest Ebook Central, http://ebookcentral.proquest.com/lib/inflibnet-ebooks/detail.action?docID=3019187.
Created from inflibnet-ebooks on 2018-02-22 20:59:47.

$$\frac{dv_r}{dt} = E_r + v_\vartheta \omega_{ci} + \frac{v_\vartheta^2}{r} \; ; \; \frac{dv_\vartheta}{dt} = -v_r \omega_{ci} - \frac{v_\vartheta v_r}{r} \tag{3.24}$$

The solution of Eqs.(3.23) is given by:

$$f_i^{**}(r, v_r, v_\theta, t + \Delta t) = f^*(r, v_r - 2a, \; v_\theta - 2b, t) \tag{3.25}$$

The shift in Eq. (3.25) is effected using a tensor product of cubic *B*-spline [6,51] for the 2D interpolation, as discussed in section 3.1. However, the quantities *a* and *b* in Eq.(3.25) are calculated analytically by solving the equations of the characteristics in Eqs.(3.24), since in the present case an analytic solution is possible, similar to what has been presented in Eqs.(2.38-2.40). This solution gives, to an order $O(\Delta t^2)$, at a given position *r*, the expressions:

$$a = \frac{\Delta t}{2}\left(E_r + \omega_{ci}\left(v_\theta + \frac{\Delta t}{2}\left(\omega_{ci} v_r + \frac{v_r v_\theta}{r} \right) \right) + \frac{v_\theta^2}{r} + \Delta t \frac{v_\theta}{r}\left(\omega_{ci} v_r + v_r v_\theta / r \right) \right) \tag{3.26}$$

$$b = -\frac{\Delta t}{2}\left(\omega_{ci} \, v_r + \frac{v_r v_\theta}{r} + \frac{\Delta t}{2}\frac{v_r}{r}\left(\omega_{ci} v_r + \frac{v_r v_\theta}{r} \right) - \frac{\Delta t}{2}\left(\omega_{ci} + \frac{v_\theta}{r} \right)\left(E_r + v_\theta \omega_{ci} + \frac{v_\theta^2}{r} \right) \right) \tag{3.27}$$

(note that an iterative solution of Eqs.(3.24) as in section 3.1 would give the same results to an order $O(\Delta t^2)$).

Step3-We then repeat the step in Eq. (3.22) for $\Delta t/2$ to calculate f^{n+1} from f^{**}.

The initial profiles are the same as in section 2.2, written in the cylindrical geometry as:

$$n_i(r) = n_e(r) = 0.5\left(1 + \tanh\left((R - r - L/5)/7.\right)\right); \tag{3.28}$$

with a similar profile for the frozen electrons. The positive *r* direction is pointing towards the right, or outside the plasma. *R* is the plasma radius and *L* the width of the edge (taken to be 175 as in section 2.2). The initial ion distribution is given by:

$$f_i(r, v_r, v_\theta) = n_i(r) \frac{e^{-(v_r^2 + v_\theta^2)/2T_i}}{2\pi T_i} \tag{3.29}$$

We assume that the deuterons hitting the wall surface or limiter at *r*= *R* are collected by a floating cylindrical vessel. Since the magnetized electrons do not move in the *r* direction across the magnetic field, there is no electron current collected at the floating vessel.

Copyright © 2009. Nova Science Publishers, Inc.. All rights reserved.

Baswell, Albert R.. Advances in Mathematics Research, Nova Science Publishers, Inc., 2009. ProQuest Ebook Central, http://ebookcentral.proquest.com/lib/inflibnet-ebooks/detail.action?docID=3019187.
Created from inflibnet-ebooks on 2018-02-22 20:59:47.

Therefore we have at $r = R$ the relation (we stress that the subscript i denotes here ion contribution):

$$\left.\frac{\partial E_r}{\partial t}\right|_{r=R} = -J_{ri}\big|_{r=R} \qquad \text{or} \qquad E_r\big|_{r=R} = -\int_0^t J_{ri}\big|_{r=R}\, dt \tag{3.30}$$

Integrating Eq. (3.20) over the domain (R-L, R), we get for the total charge σ appearing in the system:

$$RE_r\big|_{r=R} - (R-L)E_r\big|_{r=R-L} = \int_{R-L}^{R} (n_i - n_e) r dr = \sigma \tag{3.31}$$

which is the equivalent to Eq.(2.21) obtained for the slab geometry. We assume that the gyrating plasma ions (deuterons) are allowed to enter or leave at the left boundary. The electric fields at the left boundary $r = R - L$ and at the wall $r = R$ must satisfy Eq. (3.31). We use a very large value of R ($R = 10000$ Debye lengths in the present calculation, so v_θ^2 / r is negligible), so that the system should behave essentially as a Cartesian system. Indeed we recover the same results as those which have been presented in Cartesian geometry in section 2.2. These results have been presented for cylindrical geometry in Fig.(1-6) in [51], and are identical to Figs(11-16) (if we take into account the mirroring due to the fact that in the Cartesian geometry and in the cylindrical geometry, the edge gradients are in opposite directions). Fig. (29) shows at $t = 500$ the plot of the electric field E_r (solid curve, we concentrate on the region less than 100 Debye lengths from the boundary to emphasize the edge region). To position the profiles in Fig. (29) with respect to the gradient we also plot $-n_i/2$ in the same figure. The electric field has the direction of pushing the ions back to the interior of the plasma (and interact with the magnetic field to give a poloidal drift rotation, note also that in the flat part of the electric field, this drift has no shear, which can explain the absence of turbulence). The dash-dotted curve gives the Lorentz force, which in our normalized units is given by $-< v_\theta > \omega_{ci} / \omega_{pi}$, and the dotted curve gives the pressure force $\nabla P_i / n_i$, $P_i = 0.5\, n_i (T_{ir} + T_{i\theta})$, with the following definition in cylindrical geometry:

$$T_{ir,\theta}(r) = \frac{1}{n_i} \int dv_r\, dv_\theta\, (v_{r,\theta} - < v_{r,\theta} >)^2\, f_i(r, v_r, v_\theta) \tag{3.32}$$

$$< v_{r,\theta} > = \frac{1}{n_i} \int dv_r\, dv_\theta\, v_{r,\theta}\, f_i(r, v_r, v_\theta) \;; \qquad n_i(r) = \int dv_r\, dv_\theta\, f_i(r, v_r, v_\theta) \tag{3.33}$$

In steady state the transport $< v_r >$ vanishes. The broken curve in Fig. (29) gives the sum $\nabla P_i / n_i - 0.1 < v_\theta >$, which shows a very good agreement along the gradient with the solid curve for E_r. In the region less than 20 Debye lengths from the wall, we have small

Copyright © 2009. Nova Science Publishers, Inc.. All rights reserved.

Baswell, Albert R.. Advances in Mathematics Research, Nova Science Publishers, Inc., 2009. ProQuest Ebook Central, http://ebookcentral.proquest.com/lib/inflibnet-ebooks/detail.action?docID=3019187.
Created from inflibnet-ebooks on 2018-02-22 20:59:47.

oscillations in space (and time), the accuracy being degraded by the low density n_i and large ∇T_i appearing close to the surface. We plot in Fig. (30) the quantities $n_i E_r, \nabla P_i, -0.1\, n_i < v_\theta >$ and the sum $\nabla P_i - 0.1 n_i < v_\theta >$. We see that there is a very nice agreement for the relation $n_i\ E_r = \nabla P_i - 0.1\, n_i < v_\theta >$ (the density $-n_i/10$ is also plotted to locate the profiles with respect to the gradient). The charge σ / R appearing in the system and calculated by the code from Eq.(3.31) amounts to -0.360 at t = 500. The collected charge calculated from Eq.(3.29) at $r = R$ is 0.364, hence $E_r\big|_{r=R} = -0.364$. The difference $E_r\big|_{r=R} - \sigma / R$ as calculated from Eq.(3.30) gives for $E_r\big|_{r=R-L}$ the value of -0.004, which is very close to the value obtained by the code at $R - r$ = 175 (see Fig. (30)). We see also from Fig. (30) that at the left boundary inside the plasma in the flat part of the density where $\nabla P_i = 0$, the electric field is compensated by the Lorentz force due to the poloidal drift $-0.1 < v_\theta >$, while along the gradient the electric field is essentially balanced by $\nabla P_i / n_i$. Figs. (3-6) in [51] are reproducing essentially Fig.(13-16) of section 2.2 (taking into consideration the mirroring due to the difference in the positive direction). We see that the results in section 2.2 obtained in Cartesian geometry by a fractional step method associated with 1D cubic spline interpolation are the same as those obtained in this section using a cylindrical geometry , and associated with 2D interpolation in velocity space with a tensor product of cubic *B*-spline. By using two different numerical techniques based on the cubic spline interpolation with two different coordinate systems, we get identic results for the same problem. The curves in Figs(11-16) and in Figs(1-6) of [51] gives essentially identical results. This illustrates the accuracy of the method of characteristics used , and of the cubic spline used for the numerical interpolation.

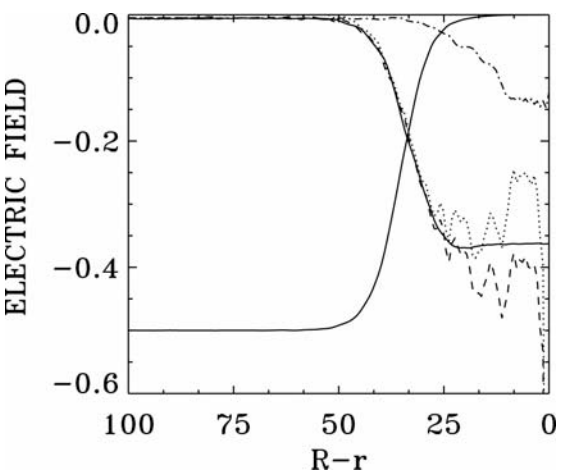

Figure 29. Plot, for the cylindrical geometry, of the electric field E_r (solid curve), the Lorentz force $-0.1 < v_\theta >$ (dash- dotted curve), the pressure force $\nabla P_i / n_i$ (dotted curve), and the sum $\nabla P_i / n_i - 0.1 < v_\theta >$ (broken curve). The density -n_i/2 is is also plotted (dash-three-dots curve, plotted for reference).

Copyright © 2009. Nova Science Publishers, Inc.. All rights reserved.

Baswell, Albert R.. Advances in Mathematics Research, Nova Science Publishers, Inc., 2009. ProQuest Ebook Central, http://ebookcentral.proquest.com/lib/inflibnet-ebooks/detail.action?docID=3019187.
Created from inflibnet-ebooks on 2018-02-22 20:59:47.

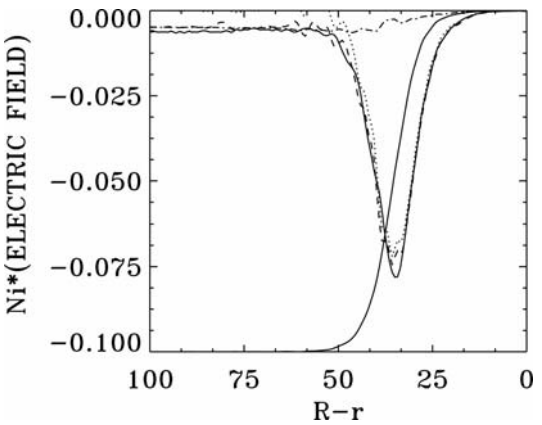

Figure 30. Plot of n_iE_r (solid curve), $-0.1n_i < v_\theta >$, (dash-dotted curve) , ∇P_i (dotted curve), and $\nabla P_i - 0.1n_i < v_\theta >$ (broken curve), (-n_i/10 is also plotted for reference).

3.3. One-Dimensional Fully Relativistic System for the Problem of Laser-Plasma Interaction

The problem of laser-plasma interaction treated in section 2.3 with a linear polarization will be repeated in this section with a full relativistic equation with a circular polarization. In the present case the fractional step will not be used , we will rather apply a 2D interpolation using a tensor product of cubic *B*-splines. When studying similarities or differences in the results, attention will be given to the accurate performance of the cubic spline interpolation. The general form of the Vlasov equation is written for the present problem (using the same normalization as in section 2.3) in a 4D phase-space for the electron distribution function $F_e(x, p_{xe}, p_{ye}, p_{ze}, t)$ and the ion distribution function $F_i(x, p_{xi}, p_{yi}, p_{zi}, t)$ (one spatial dimension) as follows [52]:

$$\frac{\partial F_{e,i}}{\partial t} + m_{e,i}\frac{p_{xe,i}}{\gamma_{e,i}}\frac{\partial F_{e,i}}{\partial x} \mp (\vec{E} + \frac{\vec{p}\ \mathrm{x}\ \vec{B}}{\gamma_{e,i}})\cdot\frac{\partial F_{e,i}}{\partial \vec{p}_{e,i}} = 0\,. \tag{3.34}$$

with
$$\gamma_{e,i} = \left(1 + m_{e,i}^2(p_{xe,i}^2 + p_{ye,i}^2 + p_{ze,i}^2)\right)^{1/2} \tag{3.35}$$

(the upper sign is for electrons and the lower sign for ions, and subscripts *e* or *i* denote electrons or ions respectively). Again in our normalized units $m_e = 1$ and $m_i = \frac{M_e}{M_i}$. Eq.(3.34) can be reduced to a two-dimensional phase-space Vlasov equation if the canonical momentum $\vec{P}_{ce,i}$ connected to the particle momentum $\vec{p}_{e,i}$ by the relation $\vec{P}_{ce,i} = \vec{p}_{e,i} \mp \vec{a}$ is chosen initially as zero. $\vec{a} = e\vec{A}/M_e c$ is the normalized vector potential. For a particle in an

Copyright © 2009. Nova Science Publishers, Inc.. All rights reserved.

Baswell, Albert R.. Advances in Mathematics Research, Nova Science Publishers, Inc., 2009. ProQuest Ebook Central, http://ebookcentral.proquest.com/lib/inflibnet-ebooks/detail.action?docID=3019187.
Created from inflibnet-ebooks on 2018-02-22 20:59:47.

electromagnetic wave propagating in a one-dimensional spatial system, we can write the following Hamiltonian:

$$H_{e,i} = \frac{1}{m_{e,i}}\left(1 + m_{e,i}^2(\vec{P}_{ce,i} \pm \vec{a})^2\right)^{1/2} \pm \varphi . \tag{3.36}$$

where φ is the electrostatic potential. Choosing the Coulomb gauge ($div\vec{a} = 0$) , we have for the vector potential $\vec{a} = \vec{a}_\perp(x,t)$, and we also have the following relation along the longitudinal direction:

$$\frac{dP_{cxe,i}}{dt} = -\frac{\partial H_{e,i}}{\partial x} \tag{3.37}$$

And since there is no transverse dependence :

$$\frac{d\vec{P}_{c\perp e,i}}{dt} = -\nabla_\perp H_{e,i} = 0 . \tag{3.38}$$

This last equation means $\vec{P}_{c\perp e,i} = \text{const}$. We can choose this constant to be zero without loss of generality, which means that initially all particles at a given (*x,t*) have the same perpendicular momentum $\vec{p}_{e,i} = \pm\vec{a}_\perp(x,t)$. The Hamiltonian now is written:

$$H_{e,i} = \frac{1}{m_{e,i}}\left(1 + m_{e,i}^2 p_{xe,i}^2 + m_{e,i}^2 a_\perp^2(x,t)\right)^{1/2} \pm \varphi(x,t) . \tag{3.39}$$

The 4D distribution function $F_{e,i}(x, p_x, \vec{p}_\perp, t)$ can now be reduced to a 2D distribution function $f_{e,i}(x, p_{xe,i}, t)$ corresponding to Eq.(3.39):

$$\frac{df_{e,i}}{dt} = \frac{\partial f_{e,i}}{\partial t} + \frac{\partial H_{e,i}}{\partial p_{xe,i}}\frac{\partial f_{e,i}}{\partial x} - \frac{\partial H_{e,i}}{\partial x}\frac{\partial f_{e,i}}{\partial p_{xe,i}} = 0 . \tag{3.40}$$

Which gives the following Vlasov equations for electrons and ions::

$$\frac{\partial f_{e,i}}{\partial t} + m_{e,i}\frac{p_{xe,i}}{\gamma_{e,i}}\frac{\partial f_{e,i}}{\partial x} + (\mp E_x - \frac{m_{e,i}}{2\gamma_{e,i}}\frac{\partial a_\perp^2}{\partial x})\frac{\partial f_{e,i}}{\partial p_{xe,i}} = 0 . \tag{3.41}$$

Where $\gamma_{e,i} = \left(1 + \left(m_{e,i} p_{e,i}\right)^2 + \left(m_{e,i} a_\perp\right)^2\right)^{1/2}$.

Copyright © 2009. Nova Science Publishers, Inc.. All rights reserved.

Baswell, Albert R.. Advances in Mathematics Research, Nova Science Publishers, Inc., 2009. ProQuest Ebook Central, http://ebookcentral.proquest.com/lib/inflibnet-ebooks/detail.action?docID=3019187.
Created from inflibnet-ebooks on 2018-02-22 20:59:47.

$$E_x = -\frac{\partial \varphi}{\partial x} \text{ and } \vec{E}_\perp = -\frac{\partial \vec{a}_\perp}{\partial t} \tag{3.42}$$

and Poisson equation is given by Eq.(2.45). The transverse electromagnetic fields E_y, B_z and E_z, B_y for the circularly polarized wave obey Maxwell's equations. With $E^\pm = E_y \pm B_z$ and $F^\pm = E_z \pm B_y$, we have:

$$(\frac{\partial}{\partial t} \pm \frac{\partial}{\partial x})E^\pm = -J_y \,.\; ; \; (\frac{\partial}{\partial t} \mp \frac{\partial}{\partial x})F^\pm = -J_z \tag{3.43}$$

Which are integrated along their vacuum characteristic $x=t$. In our normalized units we have the following expressions for the normal current densities:

$$\vec{J}_\perp = \vec{J}_{\perp e} + \vec{J}_{\perp i} \;\; ; \qquad \vec{J}_{\perp e,i} = -\vec{a}_\perp m_{e,i} \int \frac{f_{e,i}}{\gamma_{e,i}} dp_{xe,i} \,. \tag{3.44}$$

The numerical scheme to advance Eq.(3.41) from time t_n to t_{n+1} necessitates the knowledge of the electromagnetic field $E^\pm$ and $F^\pm$ at time $t_{n+1/2}$. This is done using a scheme similar to Eq.(2.53), where we integrate Eq.(3.43) exactly along the vacuum characteristics with $\Delta x = \Delta t$, to calculate $E^{\pm n+1/2}$ and $F^{\pm n+1/2}$. From Eq.(3.42) we also have $\vec{a}_\perp^{\,n+1} = \vec{a}_\perp^{\,n} - \Delta t \vec{E}_\perp^{\,n+1/2}$, from which we calculate $\vec{a}_\perp^{\,n+1/2} = (\vec{a}_\perp^{\,n+1} + \vec{a}_\perp^{\,n})/2$. To calculate $E_x^{n+1/2}$, two methods have been used. A first method calculates E_x^n from $f_{e,i}^n$ using Poisson equation, then we use a Taylor expansion::

$$\begin{aligned} & E_x^{n+1/2} = E_x^n + \frac{\Delta t}{2}\left(\frac{\partial E_x}{\partial t}\right)^n + 0.5\left(\frac{\Delta t}{2}\right)^2 \left(\frac{\partial^2 E_x}{\partial t^2}\right)^n ; \\ & \text{with } \left(\frac{\partial E_x}{\partial t}\right)^n = -J_x^n ; \qquad \left(\frac{\partial^2 E_x}{\partial t^2}\right)^n = -\left(\frac{\partial J_x}{\partial t}\right)^n \end{aligned} \,. \tag{3.45}$$

and $$J_x^n = m_i \int_{-\infty}^{+\infty} \frac{p_{xi}}{\gamma_i} f_i^{\,n} dp_{xi} - m_e \int_{-\infty}^{+\infty} \frac{p_{xe}}{\gamma_e} f_e^{\,n} dp_{xe}$$

A second method to calculate $E_x^{n+1/2}$ is to use Ampère's equation: $\frac{\partial E_x}{\partial t} = -J_x$, from which $E_x^{n+1/2} = E_x^{n-1/2} - \Delta t J_x^n$. Both methods gave the same results. The boundary conditions are the same as what has been discussed in section 2.3. Now given $f_{e,i}^n$ at mesh points (we stress here that the subscript i denotes the ion distribution function), we follow the

Copyright © 2009. Nova Science Publishers, Inc.. All rights reserved.

Baswell, Albert R.. Advances in Mathematics Research, Nova Science Publishers, Inc., 2009. ProQuest Ebook Central, http://ebookcentral.proquest.com/lib/inflibnet-ebooks/detail.action?docID=3019187.
Created from inflibnet-ebooks on 2018-02-22 20:59:47.

same steps as in section 3.1 to calculate the new value $f_{e,i}^{n+1}$ at mesh points from the relations:

$$f_{e,i}^{n+1}(\mathbf{X}_{e,i}) = f_{e,i}^{n}(\mathbf{X}_{e,i} - 2\Delta_{\mathbf{X}e,i}) \; ; \quad . \tag{3.46}$$

where $\Delta_{\mathbf{X}e,i}$ is the two dimensional vector:

$$\Delta_{\mathbf{X}e,i} = \frac{\Delta t}{2}\mathbf{V}(\mathbf{X}_{e,i} - \Delta_{\mathbf{X}e,i}, t_{n+1/2}) \; . \tag{3.47}$$

$\mathbf{X}_{e,i}$ is the two dimensional vector $\mathbf{X}_{e,i} = \left(x, p_{xe,i}\right)$, and $\mathbf{V}_{e,i} = \left(m_{e,i}\dfrac{p_{xe,i}}{\gamma_{e,i}}, \mp E_x^{n+1/2} - \dfrac{m_{e,i}}{2\gamma_{e,i}}\dfrac{\partial (a_{\perp}^{(n+1/2)})^2}{\partial x} \right)$. Eq.(3.47) for $\Delta_{\mathbf{X}e,i}$ is implicit and is solved again iteratively as in Eq.(3.9-3.10). Then $f_{e,i}^{n+1}$ is calculated by interpolating $f_{e,i}^{n}$ in Eq.(3.46) in the two dimensions $(x, p_{xe,i})$ using a tensor product of cubic *B*-splines [6] as discussed for Eqs.(3.11-3.12).

We use the same parameters as section 2.3 and in [53]. The pump wave is penetrating the plasma at the left boundary at *x*=0 where we set $E^{+}(x=0) = 2E_0 \sin(\omega_0 t)$ and $F^{-}(x=0) = 2E_0 \cos(\omega_0 t)$. The laser pump is $\omega_0 = 5.59\omega_{pe}$ and the laser wavenumber is $k_0 = 5.5(\omega_{pe}/c)$. For the scattered mode we have $\omega_{SRS} = 4.478\omega_{pe}$ and $k_{SRS} = 4.4(\omega_{pe}/c)$. For the plasma wave we have $\omega_{epw} = 1.1124\omega_{pe}$, and $k_{epw} = 9.86(\omega_{pe}/c)$. The electron thermal velocity is $v_{Te} = 0.026c$, $T_e/T_i = 3.5$. The length of the system is $L = 50.265$, and $N_x = 5000$ grid points in space, $N_v = 256$ grid points in velocity space for electrons and 128 for ions. $\Delta x = \Delta t = 0.0105$. Figs.(31-37) show the results obtained when using the present fully relativistic model. Fig(31) for the frequency spectrum of the electromagnetic wave E^{+} at *x*=5 and *t*=60 is very close to Fig.(17). We can identify the contribution of the pump and the scattered mode at $\omega_0 = 5.59\omega_{pe}$ and $\omega_{SRS} = 4.478\omega_{pe}$. Fig.(32) for the wavenumber spectrum of E^{+} is essentially the same as Fig.(18), we can identify $k_0 = 5.5(\omega_{pe}/c)$ for the laser pump wave, and $k_{SRS} = 4.4(\omega_{pe}/c)$ for the scattered mode. Figs.(33) and (34) differ from Fig.(19) and (20) by the absence of the harmonic peaks at $\omega_h = 11.18\omega_{pe}$ and $k_h = 11(\omega_{pe}/c)$. These harmonic peaks in Fig.(19) and (20) result from the $v_y B_z$ term in Eq.(2.54) as we explained at the end of section 2.3.

Copyright © 2009. Nova Science Publishers, Inc.. All rights reserved.

Baswell, Albert R.. Advances in Mathematics Research, Nova Science Publishers, Inc., 2009. ProQuest Ebook Central, http://ebookcentral.proquest.com/lib/inflibnet-ebooks/detail.action?docID=3019187.
Created from inflibnet-ebooks on 2018-02-22 20:59:47.

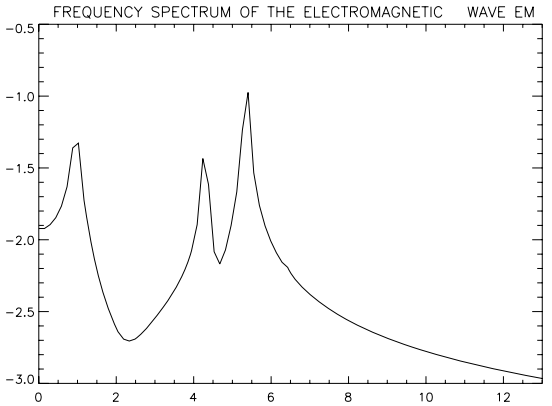

Figure 31. Frequency spectrum of E^+

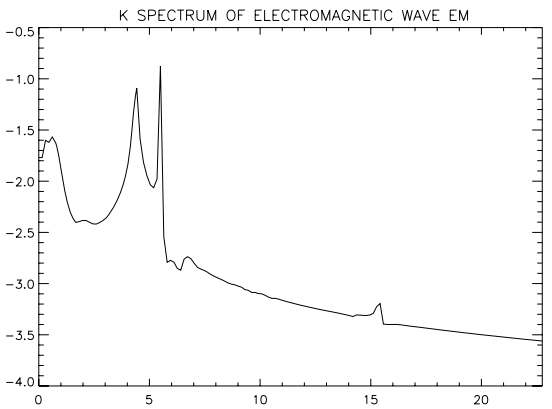

Figure 32. Wavenumber spectrum of E^+.

In circular polarization we have for the pump wave in a linear analysis, following the same notation as at the end of section 2.3, $\vec{E} = E_0(0, \cos\psi, \sin\psi)$, $\psi = (k_0 x - \omega_0 t)$. Faragay's law is:

$$\frac{\partial \vec{B}}{\partial t} = (0, \frac{\partial E_z}{\partial x}, -\frac{\partial E_y}{\partial x}).$$

which gives $\vec{B} = B_0(0, -\sin\psi, \cos\psi)$. From $\vec{E}_\perp = -\frac{\partial \vec{a}_\perp}{\partial t}$ and $\vec{p}_\perp = \vec{a}_\perp$, we get $\vec{p}_\perp = p_0(0, -\sin\psi, \cos\psi)$. We thus see that $\vec{p}\mathrm{x}\vec{B}$ is identically zero, $\vec{p}$ and $\vec{B}$ being parallel. So in this case there is no 2nd harmonic longitudinal response to the leading order.

Copyright © 2009. Nova Science Publishers, Inc.. All rights reserved.

Baswell, Albert R.. Advances in Mathematics Research, Nova Science Publishers, Inc., 2009. ProQuest Ebook Central, http://ebookcentral.proquest.com/lib/inflibnet-ebooks/detail.action?docID=3019187.
Created from inflibnet-ebooks on 2018-02-22 20:59:47.

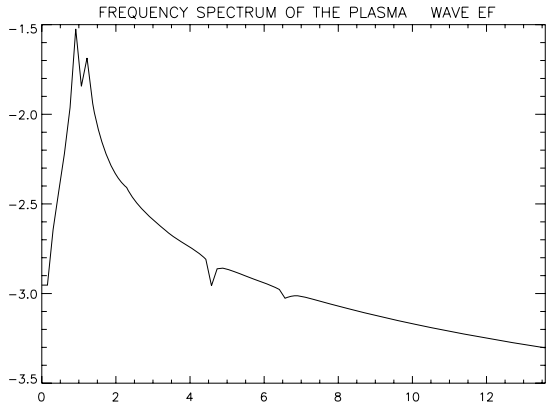

Figure 33. Frequency. spectrum of the plasma.

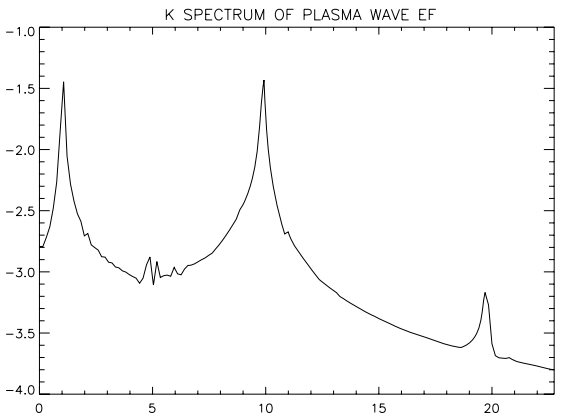

Figure 34. Wavenumber spectrum of the plasma.

We can assume following Eq.(3.41) that for $a_\perp \to 0$, we have $\gamma_{e,i} \approx \left(1+\left(m_{e,i}\, p_{e,i}\right)^2\right)^{1/2}$ and the approximation in Eq.(2.43) in section 2.3 becomes valid. Indeed, for the parameters in [53] used in this chapter, we have estimated at the end of section 2.3 that $E_0 = 0.25$. From Eq.(3.42) we can estimate that the amplitude a_0 of $\vec{a}_\perp$ is $a_0 = E_0 / \omega_0 = 0.044$, which is small. However, Fig.(35) shows the phase-space structure between x=5.1 and x=9.8 at t=60. It shows the vortices structure more important than in Fig.(21), due to the fact that the amplitude of the electric field in the present case where a circularly polarized wave is used, is now $\sqrt{E_x^2 + E_y^2} = E_0\sqrt{2}$ (if the amplitude is reduced to E_0, then the vortices are similar to Fig.(21)) . Note again the clear picture of the vortices, in the low density region of the phase-space, with very little numerical noise appearing. Figs(36) and (37) show respectively the electric field and the charge (n_i –n_e) across the box. Both figures show an enhanced value compared to what is presented in Figs.(22) and (23).

Copyright © 2009. Nova Science Publishers, Inc.. All rights reserved.

Baswell, Albert R.. Advances in Mathematics Research, Nova Science Publishers, Inc., 2009. ProQuest Ebook Central, http://ebookcentral.proquest.com/lib/inflibnet-ebooks/detail.action?docID=3019187.
Created from inflibnet-ebooks on 2018-02-22 20:59:47.

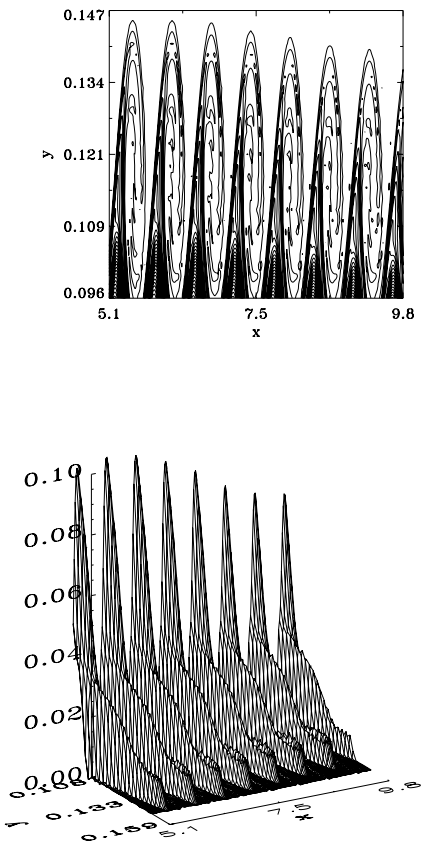

Figure 35. Contour plot and 3D view for the phase-space of the distribution function from x=5.1 to x=9.8 at $t = 60\omega_{pe}^{-1}$.

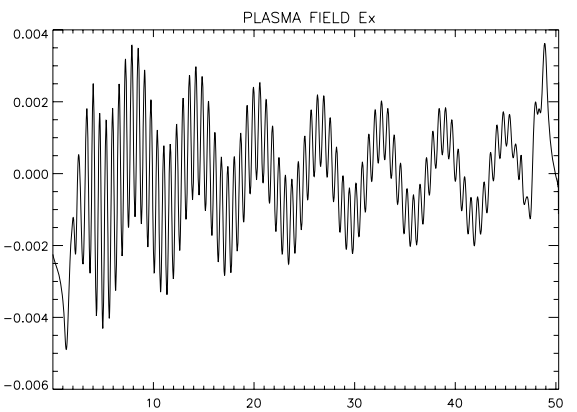

Figure 36. Longitudinal electric field.

Copyright © 2009. Nova Science Publishers, Inc.. All rights reserved.

Baswell, Albert R.. Advances in Mathematics Research, Nova Science Publishers, Inc., 2009. ProQuest Ebook Central, http://ebookcentral.proquest.com/lib/inflibnet-ebooks/detail.action?docID=3019187.
Created from inflibnet-ebooks on 2018-02-22 20:59:47.

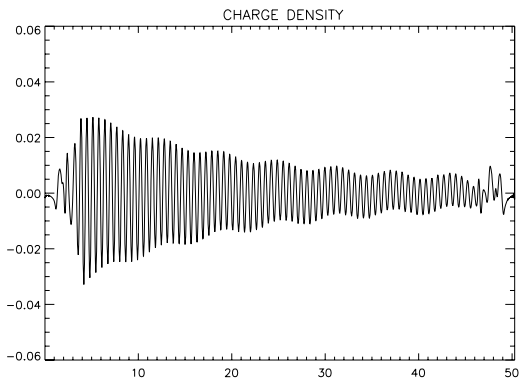

Figure 37. Charge ($n_I - n_e$).

So we have been able using the technique of cubic spline interpolation to get results from two different models for laser-plasma interaction, using two different numerical codes, which show similarities and differences in the physics associated with the scattering results. Differences observed have been explained as essentially due to different physics associated with the two models, and not to numerical problems. For the model used in section 2.3 with a linearly polarized wave, we used a method of fractional step associated with 1D interpolation using cubic spline, and in the method used in the present section with circular polarization a 2D interpolation in velocity space using a tensor product of cubic *B*-splines has been used.

3.4. Numerical Solution of a Reduced Model for the Collisionless Magnetic Reconnection

In the ideal magnetohydrodynamic (MHD) plasma description, the magnetic field is frozen in the plasma, and its flux through a surface moving with the plasma remains constant. This conservation of the magnetic topology requires that if two plasma elements are initially connected by a magnetic field line, they remain connected by a magnetic field line at any subsequent time, and it constrains the plasma dynamics by making configurations with lower magnetic energy but different topological connection inaccessible. Magnetic field reconnection removes these constraints. It is an important process in high temperature magnetically confined plasma. In this process, the magnetic configuration undergoes a topological rearrangement in a relatively short time, during which the magnetic energy is converted into heat and into kinetic flow energy. Typical situations are in tokamak plasma configurations and in solar flares and coronal loops mass ejections, when strong magnetic fields are present. In the magnetopause it allows particles from the solar wind to enter the magnetosphere. In the present work, we consider a dissipationless two-dimensional configuration with a strong superimposed homogeneous magnetic field perpendicular to the reconnection plane. In the limit of a small ion gyroradius, this two-dimensional system gives a two-fluid equations model where small scale effects related to the electron temperature and electron inertia are retained, but magnetic curvature effects are neglected. We consider a 2D configuration with a strong magnetic field in the ignorable z direction,

Copyright © 2009. Nova Science Publishers, Inc.. All rights reserved.

Baswell, Albert R.. Advances in Mathematics Research, Nova Science Publishers, Inc., 2009. ProQuest Ebook Central, http://ebookcentral.proquest.com/lib/inflibnet-ebooks/detail.action?docID=3019187.
Created from inflibnet-ebooks on 2018-02-22 20:59:47.

$\vec{B} = B_0\vec{e}_z + \nabla\psi \text{ x } \vec{e}_z$, where B_0 is constant and $\psi(x,y,t)$ is the magnetic flux function. The dimensionless governing equations, normalized to the Alfvén time τ_A and to the equilibrium scale length L_{eq}, are Hamiltonian and can be cast in a Lagrangian invariant form [62,63,64], similar to what has been presented in section 3.1:

$$\frac{\partial G_\pm}{\partial t} + \left[\phi_\pm, G_\pm\right] = 0\,;\; G_\pm = \psi - d_e^2\nabla^2\psi \pm d_e\rho_s\nabla^2\varphi \tag{3.48}$$

The Poisson brackets $\left[A,B\right] = \vec{e}_z.\nabla A \text{x} \nabla B$, and the Lagrangian invariants $G_\pm$ are conserved fields advected along the characteristic curves, $x_\pm(t)$:

$$d\vec{x}_\pm(t)/dt = \vec{\upsilon}_\pm(\vec{x}_\pm,t)\;,\; \vec{\upsilon}_\pm(\vec{x}_\pm,t) = \vec{e}_z \text{ x } \nabla\phi_\pm \tag{3.49}$$

where $\phi_\pm = \varphi \pm (\rho_s / d_e)\psi$. d_e is the electron collisionless skin depth and $\rho_s = \left(M_e / M_i\right)^{1/2} v_{the} / \omega_{ci}$ is the ion sound Larmor radius, where v_{the} is the electron thermal velocity and ω_{ci} is the ion cyclotron frequency. The magnetic flux ψ and the plasma stream function φ are given by:

$$\psi - d_e^2\nabla^2\psi = (G_+ + G_-)/2\;;\; d_e\rho_s\nabla^2\varphi = (G_+ - G_-)/2 \tag{3.50}$$

If we compare with Eq.(2.4), we see that $\phi_\pm$ play the role of the single particle Hamiltonian, and that the two Eqs.(3.48) have the form of 1D Vlasov equations, with *x* and *y* playing the role of the coordinate and the conjugate momentum for the equivalent ' distribution functions' $G_\pm$ of two 'particle ' species with opposite charges in the Poisson-type equation for φ, and equal charges in the Yukawa-type equation for ψ [62,63,64].

We apply a method of integration along the characteristics for the numerical solution of Eq(3.48), similar to what has been discussed in section 1 and for the numerical solution of Eqs.(3.1-3.2). To advance Eq.(3.48) in time, Eq.(3.49) are solved iteratively to determine the departure point of the characteristics (similar to Eq.(3.8)) , and the values of $G_\pm$ at these departure points are calculated by a two-dimensional interpolation using a tensor product of cubic *B*-splines, as discussed for Eqs.(3.9) (see Fig.(1)).The departure point of the characteristics is calculated from the expressions:

$$\Delta_{x\pm}^{k+1} = \Delta t\,\upsilon_{x\pm}(x_i - \Delta_{x\pm}^k, y_j - \Delta_{y\pm}^k; t_n) \tag{3.51}$$

$$\Delta_{y\pm}^{k+1} = \Delta t\,\upsilon_{y\pm}(x_i - \Delta_{x\pm}^k, y_j - \Delta_{y\pm}^k; t_n) \tag{3.52}$$

Copyright © 2009. Nova Science Publishers, Inc.. All rights reserved.

Baswell, Albert R.. Advances in Mathematics Research, Nova Science Publishers, Inc., 2009. ProQuest Ebook Central, http://ebookcentral.proquest.com/lib/inflibnet-ebooks/detail.action?docID=3019187.
Created from inflibnet-ebooks on 2018-02-22 20:59:47.

where $\upsilon_{y\pm} = \frac{\partial \phi_{\pm}}{\partial x}$; $\upsilon_{x\pm} = -\frac{\partial \phi_{\pm}}{\partial y}$. We start with $\Delta^0_{x\pm} = 0$, $\Delta^0_{y\pm} = 0$, and two or three iterations in Eqs.(3.51-3.52) are sufficient for convergence. The solutions $G_{\pm}$ at $t = (n+1)\Delta t$ are calculated from the expression:

$$G_{\pm}(x_i, y_j, t_{n+1}) = G_{\pm}(x_i - 2\Delta_{x\pm}, y_j - 2\Delta_{y\pm}, t_n - \Delta t) \tag{3.53}$$

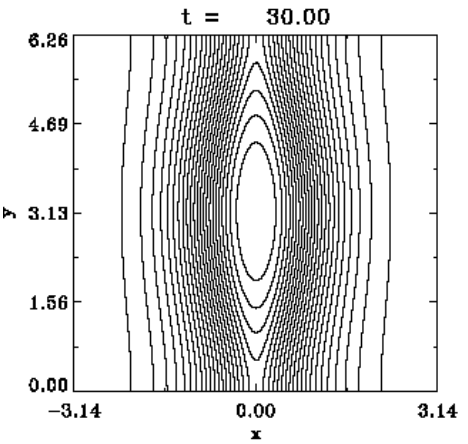

Figure 38. Magnetic flux.

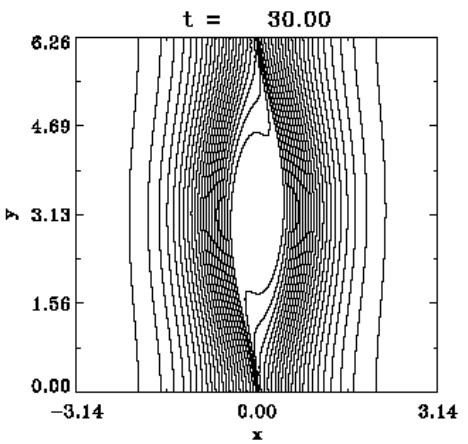

Figure 39. G_+ at time t=30.

The code in [62-64] is a finite difference code using filtering and dissipation to remove small scale features which develop. No small scales filtering or dissipation is added to the present code, as is done in [62,63]. Instead, we use a fine grid of $N_x \mathrm{x} N_y = 2048x512$ to resolve small details, and stop the calculation when the small details are of the order of the

Copyright © 2009. Nova Science Publishers, Inc.. All rights reserved.

Baswell, Albert R.. Advances in Mathematics Research, Nova Science Publishers, Inc., 2009. ProQuest Ebook Central, http://ebookcentral.proquest.com/lib/inflibnet-ebooks/detail.action?docID=3019187.
Created from inflibnet-ebooks on 2018-02-22 20:59:47.

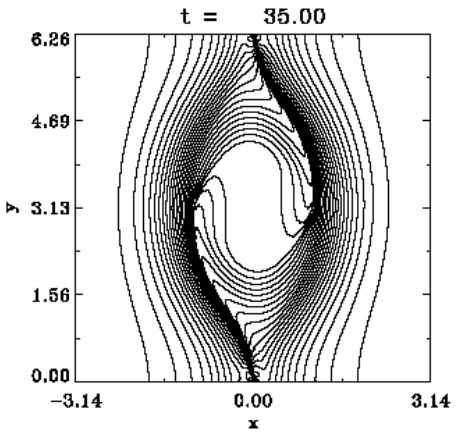

Figure 40. G_+ at time t=35.

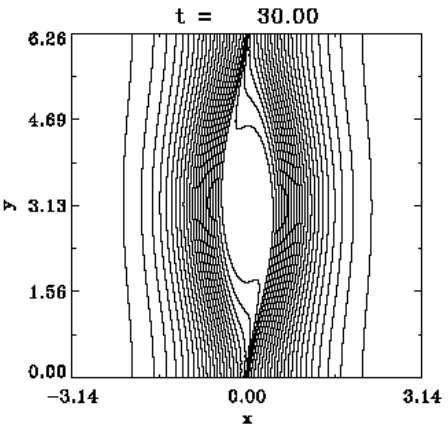

Figure 41. G_- at time t=30.

grid size.. We consider an initial equilibrium $\psi(t=0) = 1/\cosh^2(x) + \delta\psi(x,y)$, and the perturbation $\delta\psi = -10^{-4}\exp(-x^2/(2d_e^2))\cos y$ is the initial perturbation. $d_e = \rho_s = 0.2$. The equations are integrated numerically in the spatial domain $-2\pi < x < 2\pi$, $0 < y < 2\pi$. The domain is periodic in the y direction, and we apply Dirichlet boundary conditions in the x direction. The solution of Eq.(3.48) is followed by a solution of Eqs.(3.50) to determine ψ and φ, and these quantities are used to calculate $\phi_\pm$, to repeat again the integration of Eq.(3.48). The solution of Eqs.(3.50) is done by Fourier transforming in the periodic y direction, then discretizing the equations in the x direction and solving the resulting tridiagonal system with appropriate boundary conditions, and then Fourier transforming back (details have been presented in section 3.1 , Eqs(3.6-3.7)). During the evolution of the reconnection process, we see in Fig.(38) in the contours of the magnetic flux a magnetic island generated and growing in the linear phase and early non-linear phase, in which the process exhibit a quasi-explosive behaviour. In the full nonlinear regime, equilibrium is reached, the island growth saturates and remains more or less unchanged. The

Copyright © 2009. Nova Science Publishers, Inc.. All rights reserved.

Baswell, Albert R.. Advances in Mathematics Research, Nova Science Publishers, Inc., 2009. ProQuest Ebook Central, http://ebookcentral.proquest.com/lib/inflibnet-ebooks/detail.action?docID=3019187.
Created from inflibnet-ebooks on 2018-02-22 20:59:47.

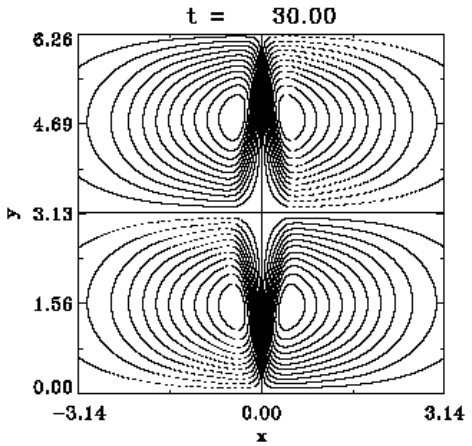

Figure 42. Stream function. φ.

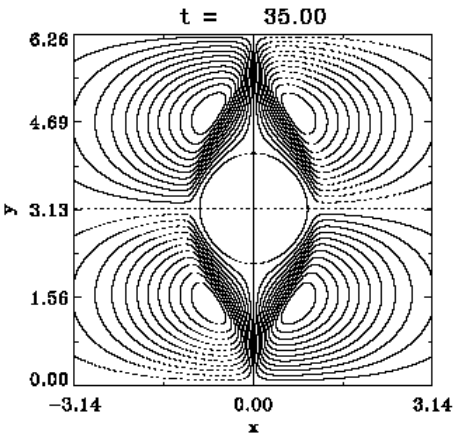

Figure 43. Stream function φ.

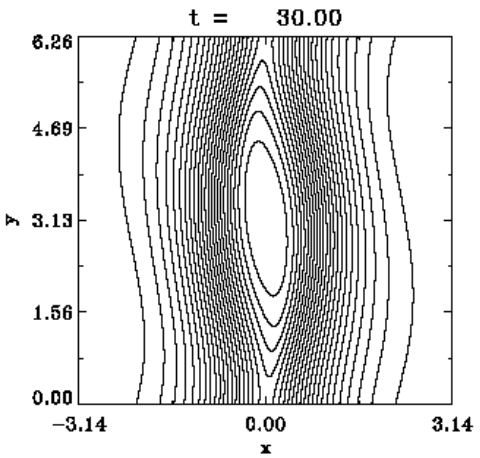

Figure 44. ϕ_+ at t=30.

Copyright © 2009. Nova Science Publishers, Inc.. All rights reserved.

Baswell, Albert R.. Advances in Mathematics Research, Nova Science Publishers, Inc., 2009. ProQuest Ebook Central, http://ebookcentral.proquest.com/lib/inflibnet-ebooks/detail.action?docID=3019187.
Created from inflibnet-ebooks on 2018-02-22 20:59:47.

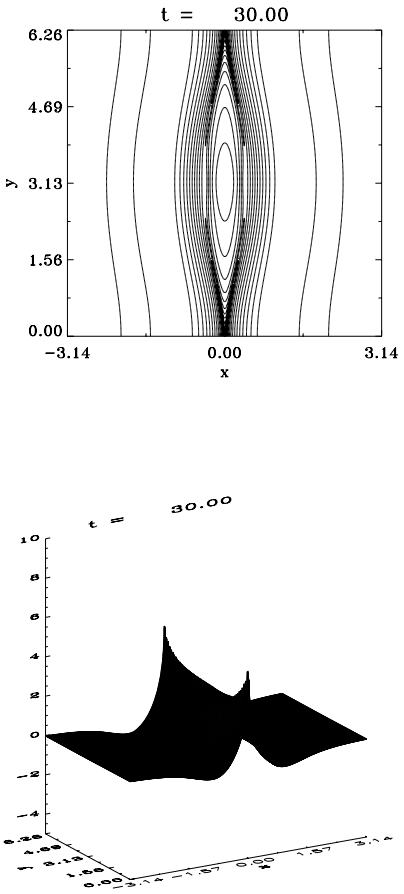

Figure 45. Current J at t =30.

contours of G_+ in Fig.(39) at t=30 and in Fig.(40) at t=35 show the formation of a vortex structure. A similar vortex structure is developed also for the invariant G_-, which is advected in the opposite direction with respect to G_+. Asymptotic states for 2D systems showing the formation of vortex structures has been discussed in [49,50], who showed that energy should move to the largest scale available in the system, showing the formation of a large vortex, similar to the 2D results we obtained in the previous examples. The model preserves parity. If we choose the initial values such that $\psi(-x) = \psi(x)$, and $\varphi(-x) = \varphi(x)$, these relations imply $G_+(-x, y) = G_-(x, y), \quad \phi_+(-x, y) = -\phi_-(x, y),$ which are maintained and accurately verified by the code. Fig.(41) for $G_-(x, y)$ at t=30 shows how this symmetry is well reproduced by the code (to be compared with Fig.(39)). Fig.(42) shows the stream function φ at t=30 and Fig.(43) at t=35. Fig.(44) shows the function ϕ_+ at t=30. In Fig.(45) we have a 3D view and a contour plot of the current $J = -\nabla_\perp^2 \psi$ at t=30. Note the important

Copyright © 2009. Nova Science Publishers, Inc.. All rights reserved.

Baswell, Albert R.. Advances in Mathematics Research, Nova Science Publishers, Inc., 2009. ProQuest Ebook Central, http://ebookcentral.proquest.com/lib/inflibnet-ebooks/detail.action?docID=3019187.
Created from inflibnet-ebooks on 2018-02-22 20:59:47.

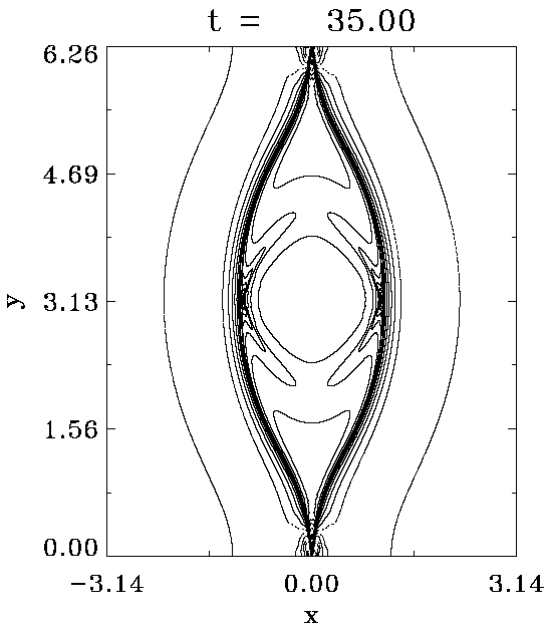

Figure 46. Current J at t =35.

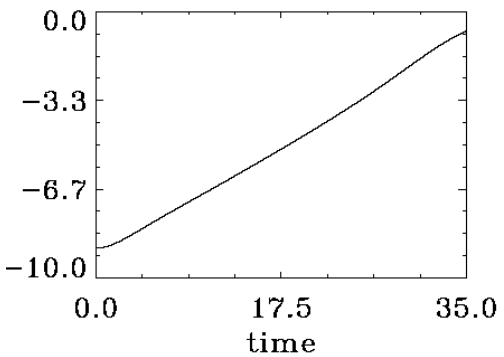

Figure 47. Plot of $\ln(\delta\psi(x = L_x/2, y = 0))$ against time.

peak structure of the current around the X-point. We note also in Fig.(46) for the contour plot of the current at t=35 the fine scale structures which develop, and which make further calculation difficult, even with the 2048x512 grid points we have. Magnetic reconnection leads to the development of increasingly narrow current and vorticity layers. To avoid this difficulty, a numerical diffusion term was added in [62,63] to smooth the solution and push further in time. But this is done at the expense of eliminating some details , as for instance the thin filament current peaking at the X-point in Fig.(45), which has not been observed in [62,63,64]. Finally we stress again the symmetry in the solution reproduced with great precision by the code. The time-step used for this calculation was $\Delta t = 10^{-3}$.

Copyright © 2009. Nova Science Publishers, Inc.. All rights reserved.

Baswell, Albert R.. Advances in Mathematics Research, Nova Science Publishers, Inc., 2009. ProQuest Ebook Central, http://ebookcentral.proquest.com/lib/inflibnet-ebooks/detail.action?docID=3019187.
Created from inflibnet-ebooks on 2018-02-22 20:59:47.

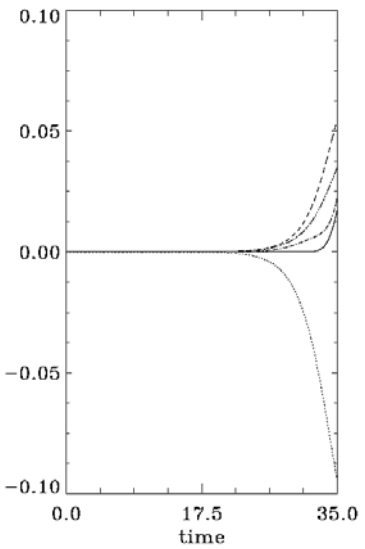

Figure 48. Plot , against time, of the difference between each term of energy, as defined in Eq.(3.54), and the corresponding value at t=0, divided by the Total energy $E(0)$.

Finally we present in Fig.(47) a curve showing the evolution of $\ln(\delta\psi(x = L_x/2, y = 0))$ against time, which shows the growth and saturation of the perturbation $\delta\psi$. And in Fig.(48), the curves present the evolution of the different energies. The magnetic energy $\int dxdy|\nabla\psi|^2$ (dotted curve), which is decaying, is transformed mainly into plasma kinetic energy $\int dxdy|\nabla\varphi|^2$ (broken curve), into electron parallel kinetic energy $\int dxdyd_e^2 J^2$ (two-dashes-dot curve), and into electron internal energy $\int dxdy\rho_s^2 U^2$ (dash-two-dots curve). The total energy E (full curve) is given by:

$$E = \int dxdy\left(|\nabla\psi|^2 + d_e^2 J^2 + \rho_s^2 U^2 + |\nabla\varphi|^2\right)/2 \tag{3.54}$$

(The quantities plotted in Fig.(48) are the difference between each term of energy as defined in Eq.(3.54), and the corresponding value at t=0, divided by the total energy $E(0)$ at t=0).

The extension of this method to the 3D reduced model [63] for collisionless magnetic reconnection is outlined as follows.

The 3D equation:

$$\frac{\partial G_\pm}{\partial t} + [\phi_\pm, G_\pm] = \frac{\partial(\phi_\pm \mp \frac{\rho_s}{d_e} G_\pm)}{\partial z} \tag{3.55}$$

is solved using a fractional step method :

Copyright © 2009. Nova Science Publishers, Inc.. All rights reserved.

Baswell, Albert R.. Advances in Mathematics Research, Nova Science Publishers, Inc., 2009. ProQuest Ebook Central, http://ebookcentral.proquest.com/lib/inflibnet-ebooks/detail.action?docID=3019187.
Created from inflibnet-ebooks on 2018-02-22 20:59:47.

Step1-Solve for a step $\Delta t/2$ the equation:

$$\frac{\partial G_{\pm}}{\partial t}+\left[\phi_{\pm},G_{\pm}\right]=0 \tag{3.56}$$

Step2-Solve for a step Δt the equation :

$$\frac{\partial G_{\pm}}{\partial t}=\frac{\partial(\phi_{\pm}\mp\frac{\rho_s}{d_e}G_{\pm})}{\partial z}; \tag{3.57}$$

Step3-Repeat Step1-.

Eq.(3.56) is solved with the same method discussed in section 1 and 3.1. Eq.(3.57) can be solved by Fourier transform in the periodic *z*-direction.

4. Application of the Method of Characteristics to Fluid Equations

We have already mentioned in section 3.1 that the 2D guiding-center equations in a magnetized plas are isomorphic to the Euler equations that govern the 2D inviscid incompressible fluids in hydrodynamics. In section 3.4, a reduced set of fluid-like equations has been applied to study magnetic reconnection. We present in this section some additional applications in the field of fluid dynamics, for the numerical solution of the shallow water equations, and for the numerical solution of the equations of the incompressible ideal magnetohydrodynamic flows in plasmas.

4.1. Numerical Solution of the Shallow Water Equations

The shallow water equations are of great importance since they are widely applied for the study of atmospheric weather prediction and oceanic dynamics. They are the simplest equations which describe both slow flows and fast gravity wave oscillations, the two main categories of fluid motion present in the more complicated primitive equations, and which are commonly used for atmospheric, oceanic and climate modeling. A method of fractional step for the numerical solution of the shallow water equations has been recently presented in [3]. It consists of splitting the equations and successively integrating in every direction along the characteristics using the Riemann invariants of the equations, which are constant quantities along the characteristics. The integration is stepped up in time using cubic spline interpolation to advance the advection terms along the characteristics. It has also the great advantage of solving the shallow water equations without the iterative steps involved in the multi-dimensional interpolation problem, and the iteration associated with the intermediate step of solving a Helmholtz equation, which is usually the case in other methods like the semi-Lagrangian or Euler-Lagrange method [7,8,65 and references therein]. The absence of iterative steps in the present method reduces considerably the numerical diffusion, and makes it suitable for problems in which small time steps and grid sizes are required, as for instance

Copyright © 2009. Nova Science Publishers, Inc.. All rights reserved.

Baswell, Albert R.. Advances in Mathematics Research, Nova Science Publishers, Inc., 2009. ProQuest Ebook Central, http://ebookcentral.proquest.com/lib/inflibnet-ebooks/detail.action?docID=3019187.
Created from inflibnet-ebooks on 2018-02-22 20:59:47.

the problem of the calculation of the potential vorticity field we study in the present section, where steep gradients and fine scale structures develop, and more generally for regional climate modeling problems. The linear analysis (unpublished) of the shallow water equations for the fractional step method shows the method is unconditionally stable, reproducing exactly the frequency of the slow mode, while the frequencies of the fast modes are exact to second order. We present in this section a new application of the fractional step method to the shallow water equations to study the evolution of a complex flow typical of atmospheric or oceanic situations, namely the nonlinear instability of a zonal jet, similar to what has been presented in [66]. As pointed out in [66], there is well established observations that even in the presence of relatively smooth, large scale flows, tracer fields in the atmosphere and the ocean develop fine scale structures. A tracer of particular significance is the potential vorticity, which develops steep gradients and evolves into thin filaments whose numerical study demands a resolution with small grid sizes and whose evolution requires small time-steps. Several methods have been discussed in [66] for the numerical solution of the potential vorticity of a zonal jet. The semi-Lagangian or Euler-Lagrange method requires iterations at each time-step to interpolate along the characteristics, and includes also an intermediate step for solving by iteration a Helmholtz equation [7,8,65,66]. This double-iterative numerical method can be computationally prohibitive if done on small grid sizes and with small time-steps, as recently pointed out in [66], and results in an important numerical diffusion difficult to evaluate or control. Other methods to solve the shallow water equations include the pseudospectral method [66], which requires the addition of an explicit hyperdiffusion for the numerical stability. This ad hoc addition of hyperdiffusion seriously degrades the solution accuracy. In the results presented in [66], the complex filamentary structures and steep gradients surrounding most vortices are substantially smoothed out in the pseudospectral and semi-Lagrange methods, this later one does worse than the pseudospectral method because the numerical diffusion occurs through repeated iterations and interpolations and is thus not directly controllable. In the contour-advective semi-Lagrangian method presented in [66], the potential vorticity is discretized by level sets separated by contours that are advected in a fully Lagrangian way. This allows one to maintain potential vorticity gradients that are steep, however the small scales in the potential vorticity are removed with contour surgery, by topologically reconnecting contours and eliminating very fine scale filamentary structures. This contour surgery is, of course, an ad hoc procedure as much as the hyperdiffusion used in the pseudospectral method. All the three previously discussed methods (semi_Lagrangian, pseudospectral and contour-advected semi-Lagrangian) require the knowledge of the calculated variables at three time levels, and require different time filtering to damp high-frequency modes and small-scale high frequency gravity waves, otherwise the numerical scheme is unstable. In the fractional step method we present in this section, no iterations are required since only two time levels are used to advance the equations in time, and no time filtering is required. So the numerical diffusion is minimal. The fractional step method applied to the shallow water equations has been recently presented and applied to a climate modeling problem [3], and compared favourably when applied with small grid sizes and time-steps with respect to the semi-Lagrangian method. Further evaluation of the performance of the fractional step method applied to the shallow water equations has been recently presented in [67]. It is the purpose of the present work to apply this fractional step method to follow on an Eulerian grid the evolution of quantities like the height and the velocity field, which are relatively broader in scale, while reconstructing and capturing at each time-step the complex

Copyright © 2009. Nova Science Publishers, Inc.. All rights reserved.

Baswell, Albert R.. Advances in Mathematics Research, Nova Science Publishers, Inc., 2009. ProQuest Ebook Central, http://ebookcentral.proquest.com/lib/inflibnet-ebooks/detail.action?docID=3019187.
Created from inflibnet-ebooks on 2018-02-22 20:59:47.

filamentary and fine scale structures and the steep gradients associated with the corresponding potential vorticity. In other words the potential vorticity is post-processed at each time step from the height and velocity field obtained from the direct solution of the shallow water equations, as it has been recently reported [68]. In the present section, the results obtained will be compared with results obtained by directly integrating the potential vorticity equation on the same Eulerian grid. These direct integrations which follow a quantity developing steep gradients and fine scale structures on an Eulerian grid develop naturally numerical noise, as it will be shown at the end of this section.

We write the two-dimensional shallow water equations in their simplest form in terms of the height *h* and the velocities (u,v) respectively along the *x* and *y* directions.

$$\frac{\partial h}{\partial t}+\frac{\partial uh}{\partial x}+\frac{\partial vh}{\partial y}=0 \ ; \tag{4.1}$$

$$\frac{\partial u}{\partial t}+u\frac{\partial u}{\partial x}+v\frac{\partial u}{\partial y}+g\frac{\partial h}{\partial x}=f\ v \ ; \ \frac{\partial v}{\partial t}+u\frac{\partial v}{\partial x}+v\frac{\partial v}{\partial y}+g\frac{\partial h}{\partial y}=-f\ u \tag{4.2}$$

f is the Coriolis parameter and *g* is the gravitational field. We write the geopotential $\phi = gh$, and we use the following time-centered scheme [68] to integrate by fractional step Eqs(4.1,4.2):

Step 1 - solve for $\Delta t/2$ the equations in the *x* direction:

$$\frac{\partial u}{\partial t}+u\frac{\partial u}{\partial x}+\frac{\partial \phi}{\partial x}=0 \ ; \tag{4.3}$$

$$\frac{\partial \phi}{\partial t}+u\frac{\partial \phi}{\partial x}+\phi\frac{\partial u}{\partial x}=0 \tag{4.4}$$

$$\frac{\partial v}{\partial t}+u\frac{\partial v}{\partial x}=0 \ ; \tag{4.5}$$

Eqs(4.3,4.4) are rewritten:

$$\frac{\partial R_{x\pm}}{\partial t}+\left(u\pm\sqrt{\phi}\right)\frac{\partial R_{x\pm}}{\partial x}=0 \quad ; \tag{4.6}$$

where $R_{x\pm}=u\pm 2\sqrt{\phi}$ are the Riemann invariants [1]. The solution of Eq. (4.6) at $t+\Delta t/2$ is written as follows:

$$R_{x\pm}\left(x,\,y,\,t+\Delta t/2\right)=R_{x\pm}\left(x_{\pm},\,y,\,t\right) \tag{4.7}$$

Copyright © 2009. Nova Science Publishers, Inc.. All rights reserved.

Baswell, Albert R.. Advances in Mathematics Research, Nova Science Publishers, Inc., 2009. ProQuest Ebook Central, http://ebookcentral.proquest.com/lib/inflibnet-ebooks/detail.action?docID=3019187.
Created from inflibnet-ebooks on 2018-02-22 20:59:47.

where $x_{\pm} = x - \int_{t}^{t+\Delta t/2} (u \pm \sqrt{\phi})dt$. The solution of Eq.(4.5) for *v* at $t + \Delta t/2$ is written:

$$v(x, y, t + \Delta t/2) = v(x - \int_{t}^{t+\Delta t/2} u dt, y, t) \tag{4.8}$$

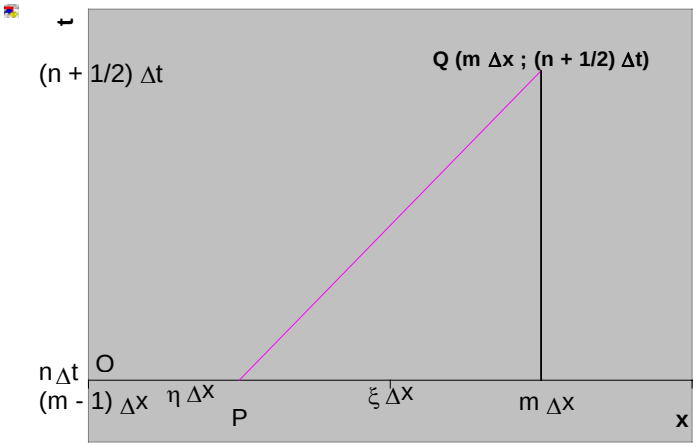

Figure 49. Details for the calculation if Eq.(4.12).

To find the value of the function at $t + \Delta t/2$ at the arrival grid points, the right hand sides of Eqs.(4.7,4.8) imply finding the value of the function at time $t = n\Delta t$ at the departure point of the characteristic at the shifted position. This value is obtained using cubic spline interpolation from the values of the function at the neighboring grid points at $t = n\Delta t$. To avoid iterations, we show as an example how the integral in Eq.(4.8) is approximated (the same technique is applied to approximate the other integrals in Eq.(4.7)). We write:

$$\xi\Delta x = \int_{t}^{t+\Delta t/2} u(x(t'), t')dt' \tag{4.9}$$

Δx is the grid size in the *x* direction, and from Eq.(4.9) $\xi\Delta x$ gives the distance of the departure point *P* of the characteristic from the grid point at $x = m\Delta x$ (the point *P* in Fig.(49) is located between the grid points $x = (m-1)\Delta x$ and $x = m\Delta x$, and the characteristic through the point *P* reaches the grid point $Q(m\Delta x, (n+1/2)\Delta t)$ at $t = (n+1/2)\Delta t$). The vertical axis in Fig.(49) is time. The velocity *u* at the point *P* (denoted by u_P), can be written as a linear interpolation at time $t = n\Delta t$ of the value of *u* at the grid point at $x = m\Delta x$ (denoted by u_m), and the value of *u* at the grid point $x = (m-1)\Delta x$ (denoted by u_{m-1}) :

Copyright © 2009. Nova Science Publishers, Inc.. All rights reserved.

Baswell, Albert R.. Advances in Mathematics Research, Nova Science Publishers, Inc., 2009. ProQuest Ebook Central, http://ebookcentral.proquest.com/lib/inflibnet-ebooks/detail.action?docID=3019187.
Created from inflibnet-ebooks on 2018-02-22 20:59:47.

$$u_p = u_{m-1}(1-\eta) + u_m\eta = u_{m-1}\xi + u_m(1-\xi) \tag{4.10}$$

where $\eta + \xi = 1$. The distance *OP* in Fig.(49) is $\eta\Delta x$. Usually *u* at the point *Q* is unknown. We use Taylor expansion for $\Delta t/2$:

$$u_Q = u_m + (u_m - u_m^{n-1/2}) = 2u_m - u_m^{n-1/2}$$

(the values of *u* without superscript denotes the time $t = n\Delta t$). We can approximate the integral in Eq.(4.9) as follows:

$$\xi\Delta x = \frac{1}{2}(u_P + u_Q)\frac{\Delta t}{2} \tag{4.11}$$

We substitute in Eq.(4.11) for u_P and u_Q. We get for the shifted value in Eq.(4.9):

$$\xi\Delta x = \frac{\frac{1}{2}(3u_m - u_m^{n-1/2})\frac{\Delta t}{2}}{1 + \frac{1}{2}(\frac{u_m - u_{m-1}}{\Delta x})\frac{\Delta t}{2}} \tag{4.12}$$

This result reduces to the one in [68] if we approximate $u_m^{n-1/2}$ by u_m in eq.(4.12). Eq.(4.12) gives an explicit approximation for the value to be shifted in Eq.(4.8). The same technique can be applied to the integrals in Eq.(4.7), so the calculation of the integrals in Eqs.(4.7,4.8) using the approximation of Eq.(4.12) remains explicit, and the interpolated values in Eqs.(4.7,4.8) are calculated using a cubic spline interpolation. No iteration is implied in this calculation. The results we present] show that this approximation is sufficient and good.

Step 2 - use the results of Step 1 to solve for $\Delta t/2$ the equations in the *y* direction:

$$\frac{\partial v}{\partial t} + v\frac{\partial v}{\partial y} + \frac{\partial \phi}{\partial y} = 0 \tag{4.13}$$

$$\frac{\partial \phi}{\partial t} + v\frac{\partial \phi}{\partial y} + \phi\frac{\partial v}{\partial y} = 0 \tag{4.14}$$

$$\frac{\partial u}{\partial t} + v\frac{\partial u}{\partial y} = 0 \ ; \tag{4.15}$$

Eqs.(4.13) and (4.14) are rewritten:

Copyright © 2009. Nova Science Publishers, Inc.. All rights reserved.

Baswell, Albert R.. Advances in Mathematics Research, Nova Science Publishers, Inc., 2009. ProQuest Ebook Central, http://ebookcentral.proquest.com/lib/inflibnet-ebooks/detail.action?docID=3019187.
Created from inflibnet-ebooks on 2018-02-22 20:59:47.

$$\frac{\partial R_{y\pm}}{\partial t} + \left(v \pm \sqrt{\phi}\right)\frac{\partial R_{y\pm}}{\partial y} = 0 \ ; \tag{4.16}$$

where $R_{y\pm} = v \pm 2\sqrt{\phi}$ are the Riemann invariants. The solution of Eq. (4.16) is written:

$$R_{y\pm}\left(x, y, t + \frac{\Delta t}{2}\right) = R_{y\pm}\left(x, y_{\pm}, t\right) \tag{4.17}$$

where $y_{\pm} = y - \int_{t}^{t+\Delta t/2} (v \pm \sqrt{\phi})dt$. The solution for *u* in Eq.(4.15) is calculated in a similar way to Eq. (4.8).

$$u(x, y, t + \Delta t/2) = u(x, y - \int_{t}^{t+\Delta t/2} v dt, t) \tag{4.18}$$

The calculation of the integrals in Eqs.(4.17) and (4.18) is effected in a similar way as explained for Eq.(4.9),by substituting *y* for *x*.

Step 3 - use the results at the end of Step 2 to solve the source terms for Δt:

$$\frac{\partial u}{\partial t} - fv = 0 \qquad ; \qquad \frac{\partial v}{\partial t} + fu = 0 \tag{4.19}$$

If we denote by U_o and V_o the values of *u* and *v* at the end of Step 2, the values of *u* and *v* after Δt in Step 3 are given by:

$$u(x, y, t + \Delta t) = U_o(x, y)\cos(f\Delta t) + V_o(x, y)\sin(f\Delta t) \ ; \tag{4.20}$$

$$v(x, y, t + \Delta t) = V_o(x, y)\cos(f\Delta t) - U_o(x, y)\sin(f\Delta t) \tag{4.21}$$

Step 4 use the results at the end of Step 3 to solve for $\Delta t/2$ the equations in the *y* direction (as in Step 2)

Step 5 use the results at the end of Step 4 to solve for $\Delta t/2$ the equations in the *x* direction (as in Step 1)

This entire cycle will advance the solution by one time-step Δt . We have mentioned that in Eqs.(4.7),(4.8) and Eqs.(4.17-4.18) the value of the function at the points of departure of the characteristics (the shifted value) are calculated from the values of the function at the grid points using a cubic spline interpolation. We use a simple cubic spline defined over three grid points, calculated by writing that the function, its first and second derivatives are continuous at the grid points. Details are given in Appendix B. Testing this cubic spline polynomial

Copyright © 2009. Nova Science Publishers, Inc.. All rights reserved.

Baswell, Albert R.. Advances in Mathematics Research, Nova Science Publishers, Inc., 2009. ProQuest Ebook Central, http://ebookcentral.proquest.com/lib/inflibnet-ebooks/detail.action?docID=3019187.
Created from inflibnet-ebooks on 2018-02-22 20:59:47.

against other methods [4] has shown that this cubic polynomial has very low numerical diffusion compared to other polynomials. The code developed for the present problem is less than 500 fortran lines. At every time step, we reconstruct the potential vorticity q from the calculated values of h, u and v using the relations:

$$q = \frac{f + \zeta}{h} \; ; \; \zeta = \frac{\partial v}{\partial x} - \frac{\partial u}{\partial y} \tag{4.22}$$

The derivatives $\partial v / \partial x$ and $\partial u / \partial y$ are calculated from the values of u and v using cubic splines. If we operate on the first equation of Eq.(4.2) by $\partial / \partial y$, and on the second equation of Eq.(4.2) by $\partial / \partial x$, we can derive with the help of Eq.(4.1) the following equation for the potential vorticity q :

$$\frac{\partial q}{\partial t} + u \frac{\partial q}{\partial x} + v \frac{\partial q}{\partial y} = 0 \tag{4.23}$$

which simply states that q is constant along the characteristics :

$$\frac{dx}{dt} = u \; ; \; \frac{dy}{dt} = v \tag{4.24}$$

As we mentioned in the introduction, it is generally difficult to find a method for the direct integration of Eq.(4.23), because the potential vorticity generally develops steep gradients and finescale structures. In any Eulerian code, this will require a large number of grid points and small time-steps. In the method we present in this paper, we solve directly for the relatively large scale variables , height and velocity in Eqs.(4.1,4.2), and the potential vorticity is accurately calculated (post-processed) at each time-step using Eq.(4.22), capturing the small scale key features and steep gradients associated with the solution.

We apply the numerical scheme presented for the numerical solution of Eqs.(4.1,4.2), and for the problem of post processing the potential vorticity from this solution. The initial flow consists of a perturbed unstable zonal jet which rapidly becomes very complex, and is specified by prescribing the initial potential vorticity as follows (we follow the notation of [66]):

$$q(x, y, 0) = \overline{q} + Q \, \mathrm{sgn}(\hat{y})(a - || \hat{y} | - a |) \tag{4.25}$$

for $| \hat{y} | < 2a$ (the vertical lines indicate the absolute value). Q is the amplitude of the potential vorticity, $\overline{q}$ is the mean potential vorticity, $2a$ is the distance from the minimum to maximum potential vorticity, and:

$$\hat{y} = y + c_m \sin mx + c_n \sin nx \tag{4.26}$$

Copyright © 2009. Nova Science Publishers, Inc.. All rights reserved.

Baswell, Albert R.. Advances in Mathematics Research, Nova Science Publishers, Inc., 2009. ProQuest Ebook Central, http://ebookcentral.proquest.com/lib/inflibnet-ebooks/detail.action?docID=3019187.
Created from inflibnet-ebooks on 2018-02-22 20:59:47.

where $\hat{y}$ is the perturbed *y* coordinate, used to perturb the jet. We use for the present test the same parameters as in [66]. Equilibrium height $\bar{h}=1$, the Coriolis factor $f=4\pi$, $a=0.5$, $\bar{h}Q/f=1$, $Q=4\pi=\bar{q}$. The deformation radius is $L_R=\sqrt{g\bar{h}}/f=0.5$, and $g=(2\pi)^2$. A doubly periodic domain which spans the range $(-\pi,\pi)$ covers about 12.5 deformation radii in each direction. We take *m*=2 , *n*=3, $c_2=-0.1$, $c_3=0.1$ to perturb the *q* profile . We use a slightly different method to calculate the initial velocities and height *h*. We assume initially *v*=0 . We balance the second of Eq.(4.2) initially:

$$fu=-g\frac{\partial h}{\partial y} \tag{4.27}$$

from which

$$f\frac{\partial u}{\partial y}=-g\frac{\partial^2 h}{\partial y^2} \tag{4.28}$$

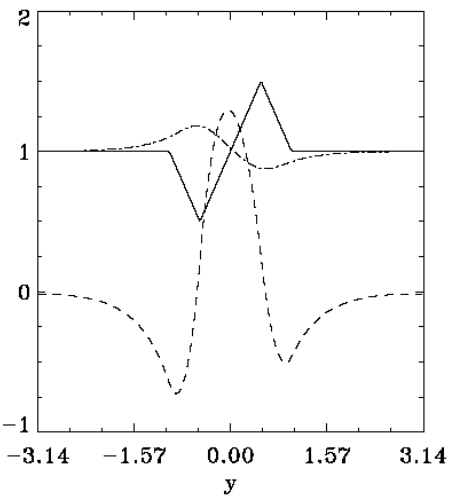

Figure 50. Initial profiles for the shallow water problem $q/4\pi$ (full curve) , *u* (broken curve), $h/2\pi$ (dash-dot curve).

We substitute for $\partial u/\partial y$ from Eq.(4.28) into Eq.(4.22) and solve numerically for the initial value of *h* .Fig.(50) shows the initial equilibrium profiles (uniform in *x*) for $q/4\pi$ (full curve) , *u* (broken curve) and $h/2\pi$ (dash-dot curve). These initial values of *u*,*v* and *h* are used in Eqs.(1,2) to start the evolution of the system. In Figs.(51) and (52) we show respectively the velocities *u* and *v* at *t*=8, and in Fig.(53) we show the contour and 3D view of the geopotential ϕ. Figs.(51-53) show structures which are generally broader in scale than the potential vorticity. Fig.(54) shows the the potential vorticity *q* , calculated at *t*=8 from Eq.(4.22). The instability in the potential vorticity has developed and the initial zonal jet has evolved into vortices and fine structures with steep gradients. These fine scale structures are

Copyright © 2009. Nova Science Publishers, Inc.. All rights reserved.

Baswell, Albert R.. Advances in Mathematics Research, Nova Science Publishers, Inc., 2009. ProQuest Ebook Central, http://ebookcentral.proquest.com/lib/inflibnet-ebooks/detail.action?docID=3019187.
Created from inflibnet-ebooks on 2018-02-22 20:59:47.

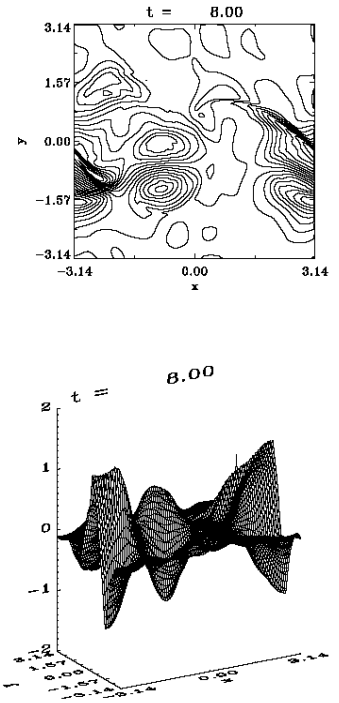

Fig 51. Velocity u .

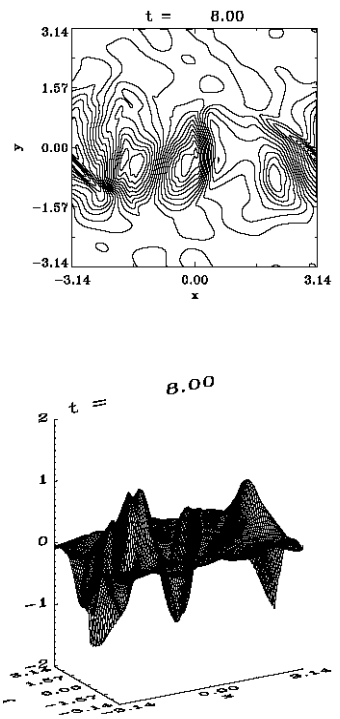

Figure 52. Velocity v.

Copyright © 2009. Nova Science Publishers, Inc.. All rights reserved.

Baswell, Albert R.. Advances in Mathematics Research, Nova Science Publishers, Inc., 2009. ProQuest Ebook Central, http://ebookcentral.proquest.com/lib/inflibnet-ebooks/detail.action?docID=3019187.
Created from inflibnet-ebooks on 2018-02-22 20:59:47.

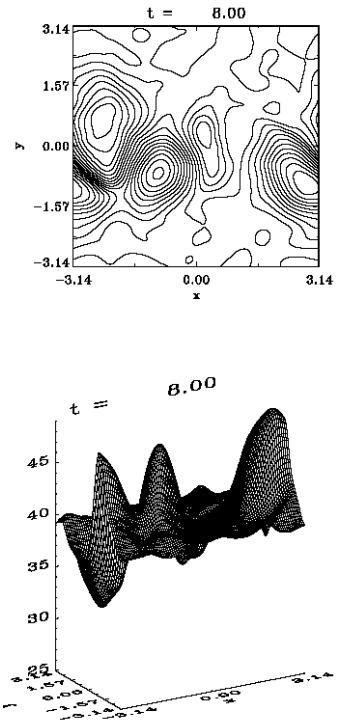

Figure 53. Geopotential ϕ.

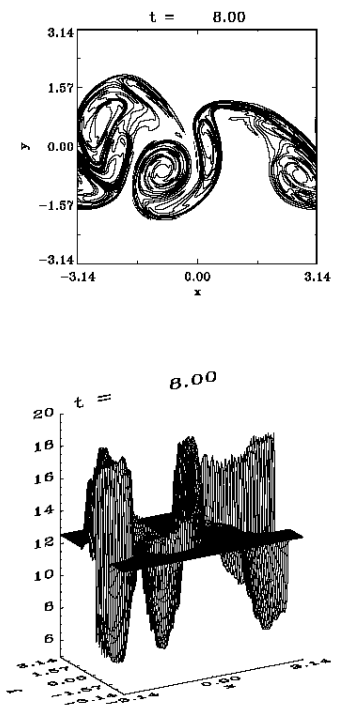

Figure 54. Potential vorticity *q*.

Copyright © 2009. Nova Science Publishers, Inc.. All rights reserved.

Baswell, Albert R.. Advances in Mathematics Research, Nova Science Publishers, Inc., 2009. ProQuest Ebook Central, http://ebookcentral.proquest.com/lib/inflibnet-ebooks/detail.action?docID=3019187.
Created from inflibnet-ebooks on 2018-02-22 20:59:47.

inevitably generated by the forward enstrophy cascade. We note how the steep potential vorticity gradients and the small scale features are nicely captured and reconstructed using Eq.(4.22), from the solution of the relatively broader scale height and velocities, by post processing these relatively smooth large scale flows with the help of Eq.(4.22). These calculations are done with 200x200 grid points, and a time-step $\Delta t = \Delta x / 20$. This time-step has been chosen after few tests to determine the time-step at which the solution appears to converge and become independent of Δt (the solution obtained with $\Delta t = \Delta x / 10$ is essentially identical to what we are presenting here). The computation CPU time on a sun-blade 1000 workstation of 750 Mhz was 64 minutes to reach t=8, and the required memory for the code was 4.5 Mbytes.

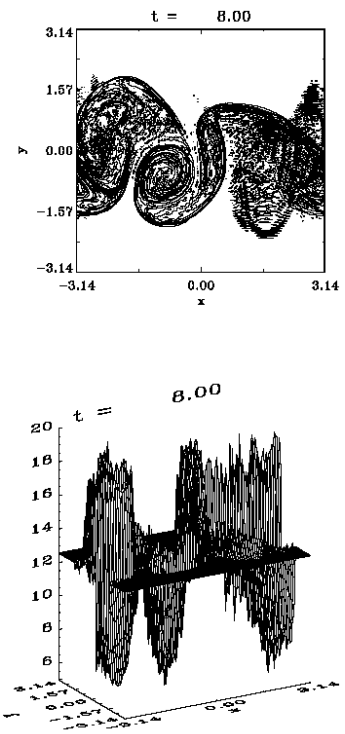

Figure 55. Potential vorticity q(fractional step method).

We present for comparison in Figs(55) the solution for the potential vorticity q obtained by the direct integration of Eq.(4.23) with the initial value in Eq.(4.25) by a fractional step method, and by a semi-Lagrangian method in Fig.(56). For the fractional step method, we follow the steps of the techniques presented in section 2 . To advance Eq.(4.23) in for a time-step Δt , we use the following sequence :

Step1 Solve for $\Delta t / 2$ the equation :

$$\frac{\partial q}{\partial t} + u \frac{\partial q}{\partial x} = 0 \tag{4.29}$$

Copyright © 2009. Nova Science Publishers, Inc.. All rights reserved.

Baswell, Albert R.. Advances in Mathematics Research, Nova Science Publishers, Inc., 2009. ProQuest Ebook Central, http://ebookcentral.proquest.com/lib/inflibnet-ebooks/detail.action?docID=3019187.
Created from inflibnet-ebooks on 2018-02-22 20:59:47.

Step2 Solve for Δt the equation:

$$\frac{\partial q}{\partial t} + v\frac{\partial q}{\partial y} = 0 \tag{4.30}$$

Step3 Repeat Step1 for $\Delta t / 2$.

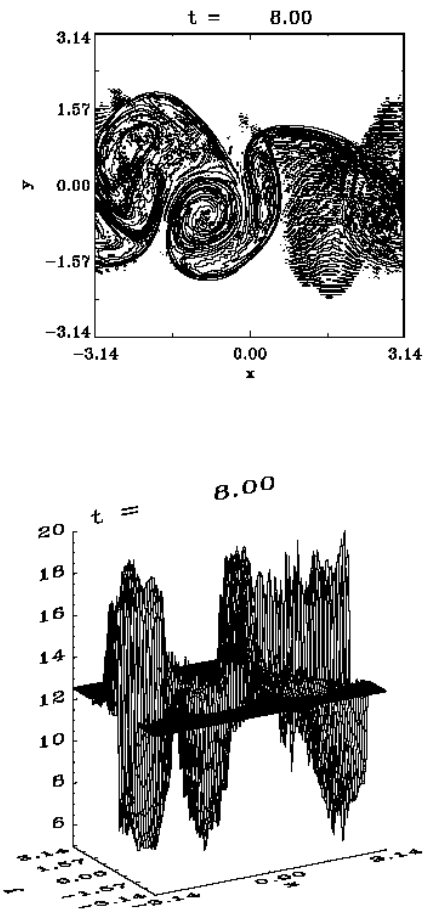

Figure 56. Potential vorticity *q* (semi-Lagrangian method).

We use the same values of *u* and *v* calculated from Eqs.(4.2). Eqs(4.29-4.30) are solved as described for Eq.(4.5), (4.6) or (4.15) . The other method used for the direct solution of Eq.(4.23) is the semi-Lagrangian or Euler-Lagrange method. As described in sections 1 and 3.1, we calculate the displacements Δ_x and Δ_y along the characteristic curves by solving iteratively the equations:

$$\Delta_x^{k+1} = \Delta t u(x - \Delta_x^k, y - \Delta_y^k, t_n) \tag{4.31}$$

Copyright © 2009. Nova Science Publishers, Inc.. All rights reserved.

Baswell, Albert R.. Advances in Mathematics Research, Nova Science Publishers, Inc., 2009. ProQuest Ebook Central, http://ebookcentral.proquest.com/lib/inflibnet-ebooks/detail.action?docID=3019187.
Created from inflibnet-ebooks on 2018-02-22 20:59:47.

$$\Delta_y^{k+1} = \Delta t v(x - \Delta_x^k, y - \Delta_y^k, t_n) \tag{4.32}$$

where u and v are calculated from Eqs.(4.2) using the same method we previously discussed. We start with $\Delta_x^0 = 0$ and $\Delta_y^0 = 0$. Usually two or three iterations are necessary to get convergence. Then the function q is advanced from $t_n - \Delta t$ to $t_n + \Delta t$ using the relation:

$$q(x, y, t_n + \Delta t) = q(x - 2\Delta_x, y - 2\Delta_y, t_n - \Delta t) \tag{4.33}$$

As explained in section 3, the interpolations in Eqs.(4.31-4.33) are done using a tensor product of cubic *B*-spline [6]] (with appropriate modification to the boundary conditions to take into account the periodicity as for instance in [51]). We used the same Eulerian grid as for the solution of Eqs.(4.1-4.2). Figs(55) and (56) show noisy figures compared to what has been presented in Fig.(53), obtained from the direct solution of Eqs.(4.1-4.2) and Eq.(4.22). This noisy behaviour is to be expected since for the fractional step and semi-Lagrangian methods we have the difficult challenge to follow on an Eulerian grid the potential vorticity of a zonal jet, a quantity which develops steep gradients and fine scale structures.

Finally the extension of the method to three dimensional problems is straightforward, requiring only the addition of an extra fractional step in the third dimension to what is presented in this section. The Appendix in [68] outlines an example for a 3D problem.

4.2. Two-Dimensional Magnetohydrodynamic Flows

We present another example for the application of the method of characteristics for the numerical solution of fluid equations, namely the equations of two-dimensional incompressible magnetohydrodynamic flows in plasmas. These equations play an important role in the understanding of strong turbulence properties in high Reynolds number conducting fluids, which have important effects on the reconnection of the magnetic field and changes of flow topology [69-72]. As discussed in section 3.4, magnetic reconnection is a fundamental process which allows magnetized plasmas to convert the energy stored in the field lines into kinetic energy of the plasma. In ideal MHD, the frozen-in flux condition prohibits the magnetic field topology to change. Thus reconnection depends on a non-ideal mechanism responsible, in the region where the topology change takes place, for the dynamics of a diffusion process which creates a mechanism that breaks the magnetic field frozen in the plasma. Hence the importance of a solution to the pertinent equations where numerical diffusion is controlled to the minimum. We have already presented in section 3.4 an application of the methods of characteristics for the numerical solution of a reduced set of MHD equations. We extend this method to the set of two-dimensional fluid ideal MHD equations usually applied to study incompressible MHD turbulence. There is an abundant literature for the numerical solution of these equations [69-72], based essentially on finite difference schemes. Our intention is to apply the method of characteristics to the solution of these equations.

The pertinent incompressible magnetohydrodynamic equations can be written in the form:

Copyright © 2009. Nova Science Publishers, Inc.. All rights reserved.

Baswell, Albert R.. Advances in Mathematics Research, Nova Science Publishers, Inc., 2009. ProQuest Ebook Central, http://ebookcentral.proquest.com/lib/inflibnet-ebooks/detail.action?docID=3019187.
Created from inflibnet-ebooks on 2018-02-22 20:59:47.

$$\frac{\partial \mathbf{z}^{\pm}}{\partial t} + \mathbf{z}^{\mp}.\nabla \mathbf{z}^{\pm} = -\nabla p + \nu \Delta \mathbf{z}^{\pm} \ . \text{div } \mathbf{z}^{\pm} = 0 \tag{4.34}$$

$\mathbf{z}^{\pm}$ denotes the Elsässer variables $\mathbf{z}^{\pm} = \mathbf{u} \pm \mathbf{B}$, where $\mathbf{u}$ is the velocity, $\mathbf{B}$ the magnetic field, and *p* the total pressure. Here we assume a magnetic Prandtl number equal to one. We use the same parameters as in [69,70]. The two-dimensional MHD equations in Eq.(4.34) are solved in a rectangular box of size $L_x = L_y = 2\pi$ with periodic boundary conditions. We use as initial conditions for the magnetic flux function ψ and the velocity streamfunction φ the following expressions :

$$\begin{aligned} \psi(x,y) &= \frac{1}{3}\left[\cos(2x+2.3) + \cos(y+4.1)\right], \\ \varphi(x,y) &= \cos(x+1.4) + \cos(y+0.5) \end{aligned} \ . \tag{4.35}$$

$\mathbf{B} = \mathbf{e}_z \mathrm{x} \nabla \psi$ and $\mathbf{u} = \mathbf{e}_z \mathrm{x} \nabla \varphi$. These initial conditions introduced in [69] show a stronger tendency to generate turbulent small scale structures than the Orszag-Tang vortex. They are made less symmetric by means of arbitrary phases. They have also been used in [70]. The numerical scheme applied to Eq.(4.34) is the following:

Step1 solve for a time step $\Delta t / 2$ the equation :

$$\frac{\partial \mathbf{z}^{\pm}}{\partial t} + \mathbf{z}^{\mp}.\nabla \mathbf{z}^{\pm} = 0 \ . \tag{4.36}$$

This equation is solved in 2D using a tensor product of cubic *B*-spline for interpolation, as described in section 1 and applied for the problems presented in section 3. We next calculate the pressure *p* by taking the divergence of Eq.(4.34). This gives the following equation:

$$\text{div}\,(\mathbf{z}^{\mp}.\nabla \mathbf{z}^{\pm}) = -\Delta p \ . \tag{4.37}$$

This equation is solved for *p* using a fast Fourier transform algorithm, since we have periodic boundary conditions.

Step2 solve for a time step Δt the equation:

$$\frac{\partial \mathbf{z}^{\pm}}{\partial t} = -\nabla p + \nu \Delta \mathbf{z}^{\pm} \ . \tag{4.38}$$

∇p is treated explicitly. The diffusion term is treated by an alternate direction implicit scheme.

Copyright © 2009. Nova Science Publishers, Inc.. All rights reserved.

Baswell, Albert R.. Advances in Mathematics Research, Nova Science Publishers, Inc., 2009. ProQuest Ebook Central, http://ebookcentral.proquest.com/lib/inflibnet-ebooks/detail.action?docID=3019187.
Created from inflibnet-ebooks on 2018-02-22 20:59:47.

Step3 repeat Step1 for a time step $\Delta t/2$.

The quantities $\mathbf{u}$ and $\mathbf{B}$ are calculated from the relations: $\mathbf{u}=\dfrac{\mathbf{z}^{+}+\mathbf{z}^{-}}{\mathbf{2}}$, $\mathbf{B}=\dfrac{\mathbf{z}^{+}-\mathbf{z}^{-}}{\mathbf{2}}$.

We write for reference the explicit form for the solution of Eq.(4.36) for $z_x^{+}=u_x+B_x$:

$$\frac{\partial z_x^{+}}{\partial t}+z_x^{-}\frac{\partial z_x^{+}}{\partial x}+z_y^{-}\frac{\partial z_x^{+}}{\partial y}=0\ . \tag{4.39}$$

The characteristic equations for Eq.(4.39) are given by:

$$\frac{dx}{dt}=z_x^{-}\ ,\quad \frac{dy}{dt}=z_y^{-}\ . \tag{4.40}$$

We calculate the displacement Δ_x and Δ_y as explained in the previous sections, using the following iterations:

$$\Delta_x^{k+1}=\frac{\Delta t}{4}z_x^{-}(x_i-\Delta_x^{k},y_j-\Delta_y^{k},t_n+\Delta t/4) \tag{4.41}$$

$$\Delta_y^{k+1}=\frac{\Delta t}{4}z_y^{-}(x_i-\Delta_x^{k},y_j-\Delta_y^{k},t_n+\Delta t/4) \tag{4.42}$$

The values of z_x^{-} and z_y^{-} at $t_n+\Delta t/4$ can be calculated by a predictor-corrector technique. Two or three iterations are necessary for the convergence in Eqs.(4.41-4.42), and a tensor product of cubic *B*-spline is used for the interpolation [6] (with appropriate modification to the boundary conditions to take into account the periodicity as for instance in [51]). Then the value of z_x^{+} is advanced in time for $\Delta t/2$ as indicated in Step1 using the relation:

$$z_x^{+}(x_i,y_j,t_n+\Delta t/2)=z_x^{+}(x_i-2\Delta_x,y_j-2\Delta y,t_n)\ . \tag{4.43}$$

Again a tensor product of cubic *B*-spline is used for the interpolation [6] in Eq.(4.43). The same method is applied to the other variables in Eq.(4.36).

Copyright © 2009. Nova Science Publishers, Inc.. All rights reserved.

Baswell, Albert R.. Advances in Mathematics Research, Nova Science Publishers, Inc., 2009. ProQuest Ebook Central, http://ebookcentral.proquest.com/lib/inflibnet-ebooks/detail.action?docID=3019187.
Created from inflibnet-ebooks on 2018-02-22 20:59:47.

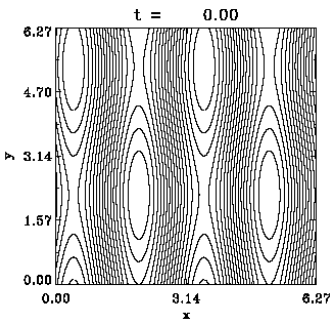

Figure 57. Current J at t=0.

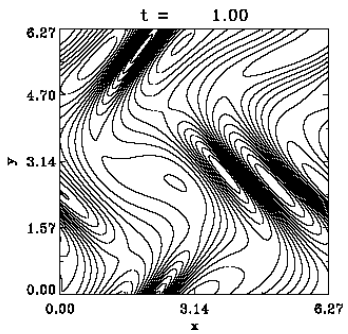

Figure 58. Current J at t=1.

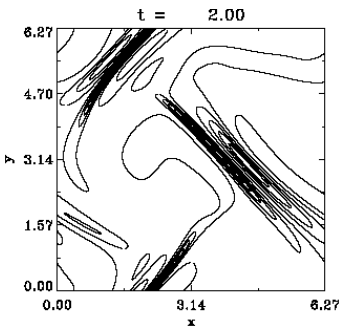

Figure 59. Current J at t=2.

The solution we present has been obtained using 512x512 grid points with the kinematic viscosity $\nu = 10^{-3}$ in Eq.(4.34). One has to be careful when ν is different from zero since any kind of smoothing may artificially inhibit the energy transfer to small scales and slow down magnetic reconnection and the associated instabilities. Comparison with the case $\nu = 0$ has shown very close results up to t=3. However, at this stage the growth of the current becomes very big and the system goes to a numerical instability for longer runs with $\nu = 0$. The nonlinear dynamics indeed leads to the formation, near neutral X points, of magnetic current sheets corresponding to strongly sheared magnetic field configurations. The finite value of ν keeps the growth of the different variables under control. A discussion of the effect of ν on the solution can be found in [71]. (We note that the claim in [70] that the first

Copyright © 2009. Nova Science Publishers, Inc.. All rights reserved.

Baswell, Albert R.. Advances in Mathematics Research, Nova Science Publishers, Inc., 2009. ProQuest Ebook Central, http://ebookcentral.proquest.com/lib/inflibnet-ebooks/detail.action?docID=3019187.
Created from inflibnet-ebooks on 2018-02-22 20:59:47.

simulation presented is done with $\nu = 0$ is probably due to the presence of an important numerical diffusion in the code). Figs(57-61) show the current density J respectively at t=0,1,2,3 and 6. From Eq.(4.35) we have:

$$B_x = -\frac{\partial \psi}{\partial y}; \quad B_y = \frac{\partial \psi}{\partial x}; \quad J = -\Delta \psi = -(-\frac{\partial B_x}{\partial y} + \frac{\partial B_y}{\partial x}) \ . \tag{4.44}$$

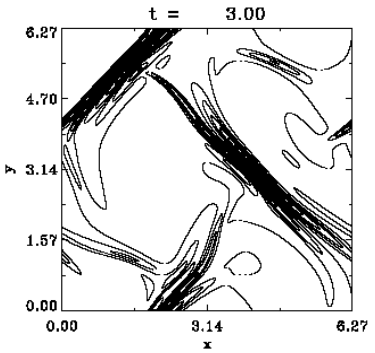

Figure 60. Current J at t=3.

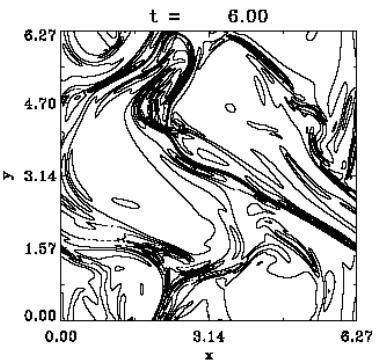

Figure 61. Current J at t=6.

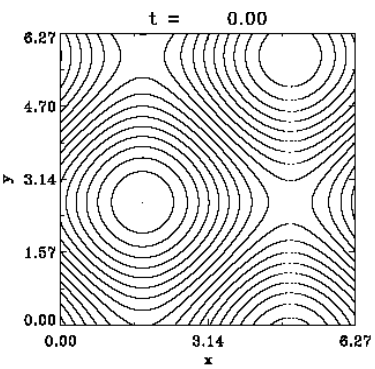

Figure 62. Vorticity at t=0.

Copyright © 2009. Nova Science Publishers, Inc.. All rights reserved.

Baswell, Albert R.. Advances in Mathematics Research, Nova Science Publishers, Inc., 2009. ProQuest Ebook Central, http://ebookcentral.proquest.com/lib/inflibnet-ebooks/detail.action?docID=3019187.
Created from inflibnet-ebooks on 2018-02-22 20:59:47.

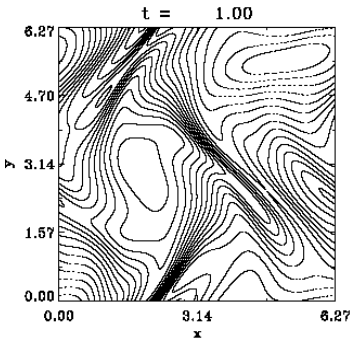

Figure 63. Vorticity at t=1.

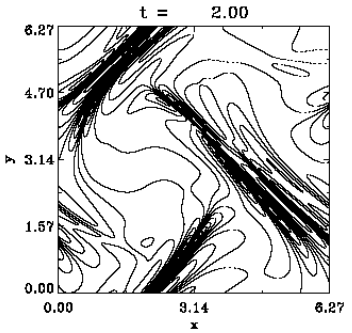

Figure 64. Vorticity at t=2.

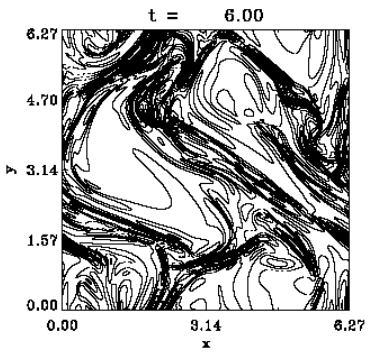

Figure 65. Vorticity at t=6.

The results in Figs.(57-61) are very close to what is presented in Fig.(2) of [70], showing the formation of current sheets. Figs.(62-65) show the vorticity U respectively at t=0,1,2 and 6. From Eqs.(4.35) we have:

$$u_x = -\frac{\partial \varphi}{\partial y}; \quad u_y = \frac{\partial \varphi}{\partial x}; \quad U = \Delta \varphi = (-\frac{\partial u_x}{\partial y} + \frac{\partial u_y}{\partial x}) \ . \tag{4.45}$$

Copyright © 2009. Nova Science Publishers, Inc.. All rights reserved.

Baswell, Albert R.. Advances in Mathematics Research, Nova Science Publishers, Inc., 2009. ProQuest Ebook Central, http://ebookcentral.proquest.com/lib/inflibnet-ebooks/detail.action?docID=3019187.
Created from inflibnet-ebooks on 2018-02-22 20:59:47.

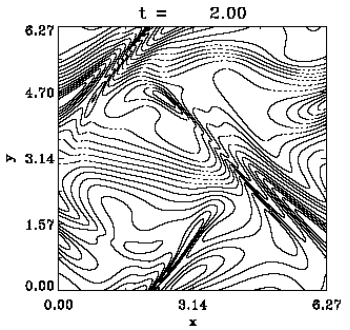

Figure 66. u_x at t=2.

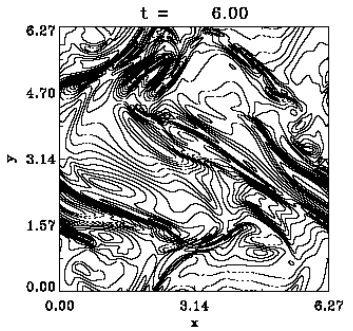

Figure 67. u_x at t=6.

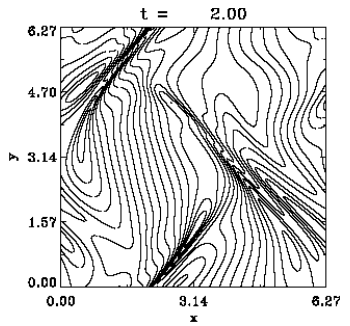

Figure 68. u_y at t=2.

At t=0, B_x, B_y, u_x, and u_y are calculated from Eq.(4.35). Figs.(66-69) show u_x, and u_y at t=2 and t=6, and Figs.(70-73) show B_x and B_y at t=2 and t=6. In Figs.(74-77) the magnetic flux function ψ at t=0,1,2 and 6 is presented. Note in Figs.(75-76) at t=1 and t=2 how, in the regions where the magnetic vortices are pushed towards each others or squeezed between each others, intense currents are created in the corresponding current density plots in Figs.(58-59). Fig.(78) presents the time evolution of the total enstrophy (which is the sum of the kinetic and magnetic enstrophies):

$$W = \int \left(\left| \nabla \mathrm{x} \mathbf{u} \right|^2 + \left| \nabla \mathrm{x} \mathbf{B} \right|^2 \right) dxdy \ . \tag{4.46}$$

Copyright © 2009. Nova Science Publishers, Inc.. All rights reserved.

Baswell, Albert R.. Advances in Mathematics Research, Nova Science Publishers, Inc., 2009. ProQuest Ebook Central, http://ebookcentral.proquest.com/lib/inflibnet-ebooks/detail.action?docID=3019187.
Created from inflibnet-ebooks on 2018-02-22 20:59:47.

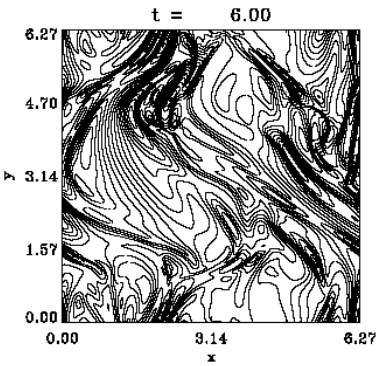

Figure 69. u_y at t=6.

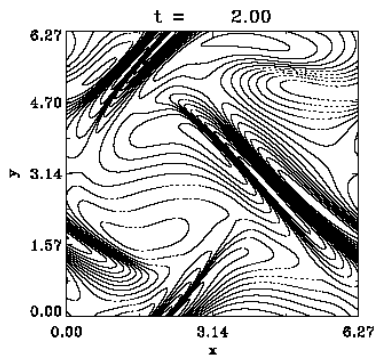

Figure 70. B_x at t=2.

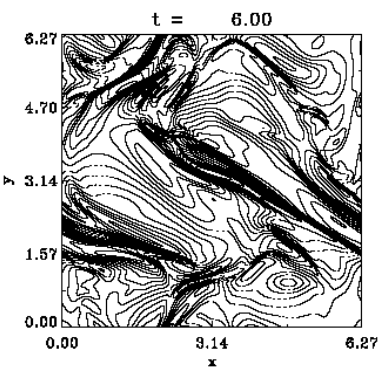

Figure 71. B_x at t=6.

In Fig.(79) we present the time evolution of the total energy (which is the sum of the kinetic and magnetic energies):

$$E = \frac{1}{2}\int \left(|\mathbf{u}|^2 + |\mathbf{B}|^2 \right) dxdy \ . \tag{4.47}$$

Copyright © 2009. Nova Science Publishers, Inc.. All rights reserved.

Baswell, Albert R.. Advances in Mathematics Research, Nova Science Publishers, Inc., 2009. ProQuest Ebook Central, http://ebookcentral.proquest.com/lib/inflibnet-ebooks/detail.action?docID=3019187.
Created from inflibnet-ebooks on 2018-02-22 20:59:47.

The time evolution of the velocity-magnetic field correlation [70] $\rho = \left|H\right| / E$, where the cross-correlation $H = \int \mathbf{u}.\mathbf{B} dxdy$, is presented in Fig.(80). The distribution of kinetic and magnetic energies among the different scales is described by the kinetic and magnetic energy spectra:

$$E^u(k) = \sum_{k \le |\mathbf{k}'| < k+1} \left|\hat{\mathbf{u}}(\mathbf{k}')\right|^2 \quad . \tag{4.48}$$

$$E^M(k) = \sum_{k \le |\mathbf{k}'| < k+1} \left|\hat{\mathbf{B}}(\mathbf{k}')\right|^2 \quad . \tag{4.49}$$

Fig.(81) shows on a logarithmic scale the kinetic ($\log_{10} E^u$ solid line) and magnetic ($\log_{10} E^M$ dashed line) energy spectra at *t*=6 (plotted against $\log_{10} k$, with *k* varying between 1 and 100, showing a slight dominance of the magnetic energy over the kinetic energy over most of the scale lengths). It is beyond the scope of the present work to repeat what has been presented in [69-72]. We intended in this section to outline the pertinent steps for one more application of the method of characteristics (which generally shows low numerical diffusion) to the equations of ideal MHD flows.

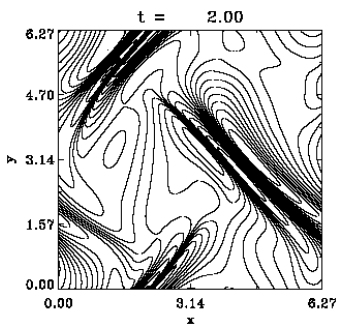

Figure 72. B_y at t=2.

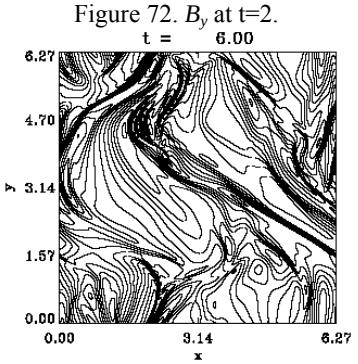

Figure 73. B_y at t=6.

Copyright © 2009. Nova Science Publishers, Inc.. All rights reserved.

Baswell, Albert R.. Advances in Mathematics Research, Nova Science Publishers, Inc., 2009. ProQuest Ebook Central, http://ebookcentral.proquest.com/lib/inflibnet-ebooks/detail.action?docID=3019187.
Created from inflibnet-ebooks on 2018-02-22 20:59:47.

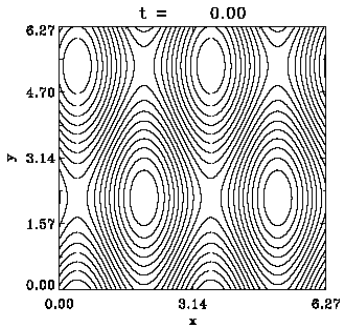

Figure 74. Flux function ψ at t=0.

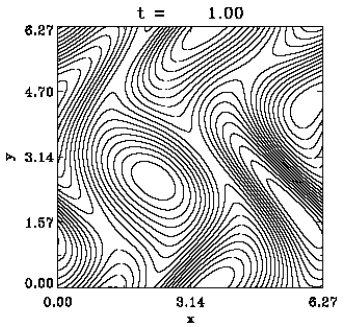

Figure 75. Flux function ψ at t=1.

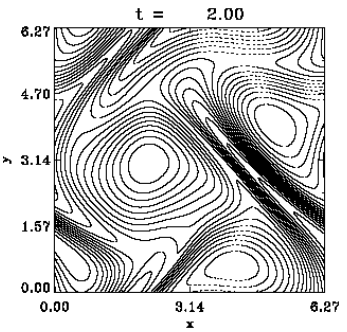

Figure 76. Flux function ψ at t=2.

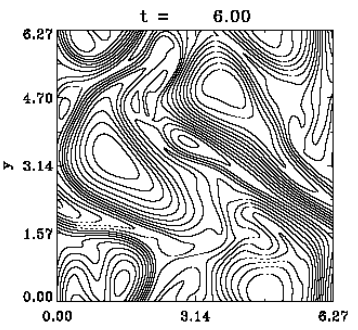

Figure 77. Flux function ψ at t=6.

Copyright © 2009. Nova Science Publishers, Inc.. All rights reserved.

Baswell, Albert R.. Advances in Mathematics Research, Nova Science Publishers, Inc., 2009. ProQuest Ebook Central, http://ebookcentral.proquest.com/lib/inflibnet-ebooks/detail.action?docID=3019187.
Created from inflibnet-ebooks on 2018-02-22 20:59:47.

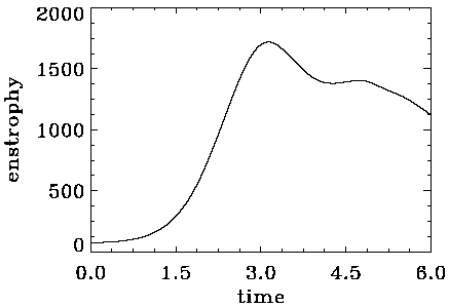

Figure 78. Time evolution of the enstrophy.

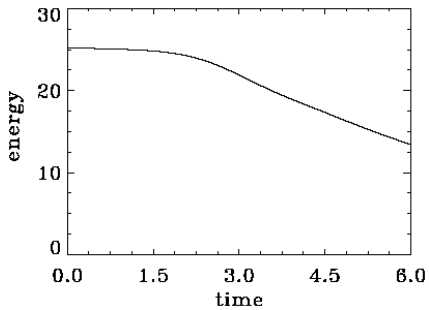

Figure 79. Time evolution of the energy.

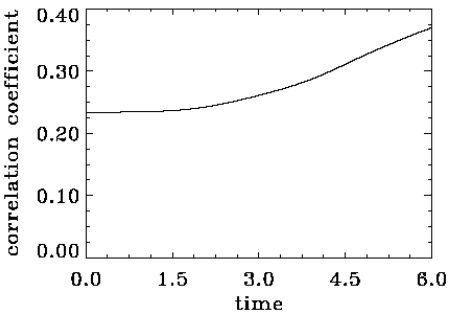

Figure 80. Time evolution of the correlation coefficient

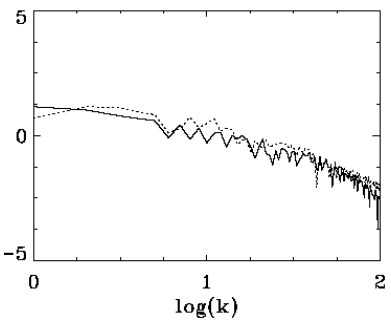

Figure 81. Kinetic (solid line) and magnetic (dashed line) energy spectra at t=6.

Copyright © 2009. Nova Science Publishers, Inc.. All rights reserved.

Baswell, Albert R.. Advances in Mathematics Research, Nova Science Publishers, Inc., 2009. ProQuest Ebook Central, http://ebookcentral.proquest.com/lib/inflibnet-ebooks/detail.action?docID=3019187.
Created from inflibnet-ebooks on 2018-02-22 20:59:47.

5. Conclusion

We have presented in the appendices some simple cubic spline relations which we have applied for interpolation in several problems, showing how hyperbolic type differential equations are solved using the method of characteristics. The values of the functions which remain constant along the characteristic curves are stepped-up in time using cubic spline interpolation. Results illustrating the performance of the cubic spline when applied to interpolation in Eulerian grid-based solvers have been presented. Comparison of the cubic spline interpolation with other methods [4] have shown that the cubic spline interpolation compares favourably with the other methods. Since the ground breaking work of Cheng and Knorr [10] which applied the fractional step method to the one-dimensional Vlasov equation, there has been important applications of the method of characteristics for the numerical solution of the kinetic equations of plasmas, and especially for extending these methods to higher dimensions [15-18]. A historical overview on several applications of these methods in the field of the kinetic equations of plasmas has been recently given in a Vlasovia workshop [73]. This workshop included also recent applications on massively parallel computers, especially in the field of the numerical solution of gyro-kinetic equations [74-77], which testify for the impressive advances and applications of these methods. We mention also the work in [78,79]. It is beyond the scope of the present chapter to review all these works. The intention in this chapter was to present the essential elements of the interesting technique of the method of characteristics associated with cubic splines interpolation, with appropriate selected examples to illustrate the performance, the accuracy, the powerful and efficient tools which Eulerian grid-based solvers can provide for the numerical solution of plasmas kinetic equations and fluid equations: long time evolution of 1D BGK modes, charge separation at a plasma edge involving higher phase-space dimensionality, laser-plasma interaction, magnetic reconnection and the shallow water equations. In section 2.2 and section 3.2 for instance, we have presented the problem of the formation of a charge separation and an electric field at a plasma edge. In Cartesian geometry in section 2.2 a method of fractional step associated with 1D cubic spline interpolation along the characteristic curves has been applied, while in cylindrical geometry in section 3.2 a two dimensional interpolation using a tensor product of cubic *B*-spline [51] has been applied in velocity space. The results from these two different codes are identical (can be superposed if we take into consideration a mirroring due to the opposite positive direction in the two codes). Another comparison has been presented in section 2.3 and 3.3, where two different models for laser-plasma interaction have been discussed. The model in section 2.3 uses a linear polarization for the electromagnetic wave, and applies a method of fractional step for the numerical solution of the equations, associated with one dimensional cubic spline interpolation. The model in section 3.3 is fully relativistic with circular polarization, and applies a two dimensional interpolation with a tensor product of cubic *B*-spline. Again the two different codes are providing similar results, the only difference reflects and underlines the difference in the physical models. Several recent applications of similar codes for problems of laser-plasma interaction have been recently reported [30,31,52], which testify for the success of these methods, together with different other applications of the method of characteristics for the kinetic equations of plasmas which we have rapidly reviewed. In section 3.4 for the numerical solution of the problem of magnetic reconnection, a thin filament current has been observed at the X-point in Fig.(45)

Copyright © 2009. Nova Science Publishers, Inc.. All rights reserved.

Baswell, Albert R.. Advances in Mathematics Research, Nova Science Publishers, Inc., 2009. ProQuest Ebook Central, http://ebookcentral.proquest.com/lib/inflibnet-ebooks/detail.action?docID=3019187.
Created from inflibnet-ebooks on 2018-02-22 20:59:47.

which was not previously observed in [62-64] where an artificial numerical diffusion was added. The method of characteristics has also been applied for the numerical solution of fluid equations. At the same time where [10] was published, the application of the method of characteristics in 1D fluid equations associated with cubic spline interpolation was also published in [80]. In plasma physics, one of the early applications of this method to fluid equations has been for the numerical solution of the coupled mode equations [81-82]. There is an abundant theoretical literature on the method of characteristics applied to fluid equations (see for instance [1,83]). 2D interpolation using tensor product of cubic *B*-splines is commonly applied for the numerical solution of the weather forecast equations in what is known as the semi-Lagrangian method [7,8,65,66]. In section 4.1 we have presented an interesting application to the problem of the calculation of the potential vorticity of a zonal jet from the solution of the shallow water equations, reproducing on an Eulerian grid the fine scale structures and the steep gradients of the potential vorticity without numerical noise. And the problem of magnetic reconnection using the equations of the incompressible ideal MHD flows in plasmas has been studied in section 4.2.

Acknowledgments

The tutoring and fruitful discussions with Professor Georg Knorr are gratefully acknowledged. I would like also to acknowledge the fruitful discussions with Drs. Hartmut Gerhauser and Karl-Heinz Finken on the problem of the formation of an electric field at a plasma edge, and the collaboration with Dr. Erich Pohn on problems of two-dimensional interpolation used in the present chapter, as well as with Dr. David Strozzi for problems of laser-plasma interaction presented in section 2.3.

Appendix A
The Shift Operator Using the Cubic Spline

Let us assume $0 < \Delta < 1$, with a uniform grid size normalized to 1 , and Δ is a constant. We use a Taylor expansion to calculate the shifted value $y_j(x_j + \Delta) = \widetilde{y}_j$, with the function $y = f(x)$ and the notation $f(x_j) = f_j$:

$$y_j(x_j + \Delta) = \widetilde{y}_j = f_j + p_j\Delta + \frac{1}{2}s_j\Delta^2 + g_j\Delta^3 \tag{A.1}$$

p_j, s_j and g_j are respectively the derivative, second derivative and third derivative of the function $f(x)$ at the grid point $j \equiv x_j$. We write that the function, its derivative and second derivative are continous at every grid point, we get the following cubic spline relations on a uniform grid [84,85]:

$$p_{j-1} + 4p_j + p_{j+1} = 3(f_{j+1} - f_{j-1}) \tag{A.2}$$

Copyright © 2009. Nova Science Publishers, Inc.. All rights reserved.

Baswell, Albert R.. Advances in Mathematics Research, Nova Science Publishers, Inc., 2009. ProQuest Ebook Central, http://ebookcentral.proquest.com/lib/inflibnet-ebooks/detail.action?docID=3019187.
Created from inflibnet-ebooks on 2018-02-22 20:59:47.

$$s_{j-1} + 4s_j + s_{j+1} = 6(f_{j-1} - 2f_j + f_{j-1}) \tag{A.3}$$

$$g_{j-1} + 4g_j + g_{j+1} = -f_{j-1} + 3f_j - 3f_{j+1} + f_{j+2} \tag{A.4}$$

We can verify after substitution from Eqs.(A.2-A.4) in Eq.(A.1) the following relation:

$$\tilde{y}_{j-1} + \tilde{y}_j + \tilde{y}_{j+1} = Af_{j-1} + Bf_j + Cf_{j+1} + Df_{j+2} \tag{A.5}$$

$$A = (1-\Delta)^3 \tag{A.6}$$

$$B = 4 - 3\Delta^2(1 + (1-\Delta)) \tag{A.7}$$

$$C = 4 - 3(1-\Delta)^2(1+\Delta) \tag{A.8}$$

$$D = \Delta^3 \tag{A.9}$$

We verify that for $\Delta = 0$ we have from Eq.(A.5):

$$\tilde{y}_{j-1} + \tilde{y}_j + \tilde{y}_{j+1} = f_{j-1} + 4f_j + f_{j+1}$$

i.e.

$$\tilde{y}_j = f_j$$

and for $\Delta = 1$ we verify that:

$$\tilde{y}_{j-1} + \tilde{y}_j + \tilde{y}_{j+1} = f_j + 4f_{j+1} + f_{j+2}$$

i.e.

$$\tilde{y}_j = f_{j+1}$$

as it should be.

The inversion of the tridiagonal matrix in Eq.(A.5) with appropriate boundary conditions determines $\tilde{y}_j$. The calculation of $y_j(x_j - \Delta) = \tilde{y}_j$ with $0 < \Delta < 1$ is done in a similar way and leads to the following relation :

$$\tilde{y}_{j-1} + \tilde{y}_j + \tilde{y}_{j+1} = Af_{j+1} + Bf_j + Cf_{j-1} + Df_{j-2} \tag{A.10}$$

Appendix B
Interpolation Using the Cubic Spline

In the general case of a variable grid size, and for an equation of the form:

Copyright © 2009. Nova Science Publishers, Inc.. All rights reserved.

Baswell, Albert R.. Advances in Mathematics Research, Nova Science Publishers, Inc., 2009. ProQuest Ebook Central, http://ebookcentral.proquest.com/lib/inflibnet-ebooks/detail.action?docID=3019187.
Created from inflibnet-ebooks on 2018-02-22 20:59:47.

$$\frac{\partial f}{\partial t} + \upsilon(x)\frac{\partial f}{\partial x} = 0 \tag{B.1}$$

The interpolation with a cubic spline polynomial is treated as follows. We assume that $y_j(x)$ is a cubic polynomial in $\{x_j, x_{j+1}\}$ such that $y_j(x_j) = f(x_j) = f_j$, and $y_j(x_{j+1}) = f(x_{j+1}) = f_{j+1}$. We denote by s_j the second derivative at the point x_j, and we set $\Delta x_j = x_{j+1} - x_j$. We can write for the second derivative in $\{x_j, x_{j+1}\}$ the following linear interpolation:

$$y_j''(x) = s_j \frac{x_{j+1} - x}{\Delta x_j} + s_{j+1}\frac{x - x_j}{\Delta x_j} \tag{B.2}$$

so that $y_j''(x_j) = s_j$ and $y_j''(x_{j+1}) = s_{j+1}$. Integrating twice Eq.(B.2), we get:

$$y_j(x) = \frac{s_j}{6\Delta x_j}(x_{j+1} - x)^3 + \frac{s_{j+1}}{6\Delta x_j}(x - x_j)^3 + a_j(x_{j+1} - x) + b_j(x - x_j) \tag{B.3}$$

With $y_j(x_j) = f(x_j) = f_j$, and $y_j(x_{j+1}) = f(x_{j+1}) = f_{j+1}$, we get:

$$a_j = \frac{f_j}{\Delta x_j} - s_j\frac{\Delta x_j}{6}\ ;\ b_j = \frac{f_{j+1}}{\Delta x_j} - s_{j+1}\frac{\Delta x_j}{6} \tag{B.4}$$

and

$$\begin{aligned} y_j(x) = {} & \frac{s_j}{6\Delta x_j}(x_{j+1} - x)^3 + \frac{s_{j+1}}{6\Delta x_j}(x - x_j)^3 + \left(\frac{f_j}{\Delta x_j} - s_j\frac{\Delta x_j}{6}\right)(x_{j+1} - x) \\ & + \left(\frac{f_{j+1}}{\Delta x_j} - s_{j+1}\frac{\Delta x_j}{6}\right)(x - x_j) \end{aligned} \tag{B.5}$$

We write that the derivative $y_j'(x)$ is continuous at $x = x_j$: $y_j'(x_j) = y_{j-1}'(x_j)$, we get the following relation:

$$\Delta x_j s_{j+1} + 2(\Delta x_j + \Delta x_{j-1})s_j + \Delta x_{j-1}s_{j-1} = 6\left(\frac{f_{j+1} - f_i}{\Delta x_j} - \frac{f_j - f_{j-1}}{\Delta x_{j-1}}\right) \tag{B.6}$$

Copyright © 2009. Nova Science Publishers, Inc.. All rights reserved.

Baswell, Albert R.. Advances in Mathematics Research, Nova Science Publishers, Inc., 2009. ProQuest Ebook Central, http://ebookcentral.proquest.com/lib/inflibnet-ebooks/detail.action?docID=3019187.
Created from inflibnet-ebooks on 2018-02-22 20:59:47.

Inverting the tridiagonal matrix in Eq.(B.6) with proper boundary conditions determine the s_j to be used in the cubic polynomial given in Eq.(B.5), which can also be rewritten in the form:

$$y_j(x) = A_j f_j + B_j f_{j+1} + C_j s_j + D_j s_{j+1} \tag{B.5}$$

Where $A_j = \dfrac{x_{j+1} - x}{\Delta x_j}$; $B_j = \dfrac{x - x_j}{\Delta x_j}$; $C_j = \dfrac{\Delta x_j^2}{6} A_j (A_j^2 - 1)$; $D_j = \dfrac{\Delta x_j^2}{6} B_j (B_j^2 - 1)$.

For a value of $y_j(x)$ at $x = x_j + \Delta_j$ where $x_j < x < x_{j+1}$, (as for instance in Eq.(B.1) when $\Delta_j = \upsilon(x_j)\Delta t,\ \upsilon(x_j) < 0)$ we have : $A_j = 1 - \dfrac{\Delta_j}{\Delta x_j}$ and $B_j = \dfrac{\Delta_j}{\Delta x_j}$. It is straightforward to derive from the previous results the expression for $y_j(x)$ at $x = x_j - \Delta_j$, where $x_{j-1} < x < x_j$.(as for instance in Eq.(B.1) when $\Delta_j = \upsilon(x_j)\Delta t,\ \upsilon(x_j) > 0)$. In this case we have, with $\Delta x_{j-1} = x_j - x_{j-1}$, we have:

$$y_j(x) = A_j f_j + B_j f_{j-1} + C_j s_j + D_j s_{j-1} \tag{B.6}$$

Where $A_j = 1 - B_j$; $B_j = \left| \dfrac{\Delta_j}{\Delta x_{j-1}} \right|$; $C_j = \dfrac{\Delta x_{j-1}^2}{6} A_j (A_j^2 - 1)$; $D_j = \dfrac{\Delta x_{j-1}^2}{6} B_j (B_j^2 - 1)$.

(note that in the previous results, we assumed , $\left|\upsilon(x_j)\right|\Delta t < \Delta x_j$, but the results can be generalized without difficulty to arbitrary values of $\left|\upsilon(x_j)\right|\Delta t$).

Appendix C
Interpolation Using the Cubic *B*-spline

To interpolate using a cubic *B*-spline, we write the function *f(x)* as follows:

$$f(x) = \sum_{j=-2}^{N_x - 1} \gamma_j B_j(x) \tag{C.1}$$

where the $B_j(x)$ are defined as follows [84]:

Copyright © 2009. Nova Science Publishers, Inc.. All rights reserved.

Baswell, Albert R.. Advances in Mathematics Research, Nova Science Publishers, Inc., 2009. ProQuest Ebook Central, http://ebookcentral.proquest.com/lib/inflibnet-ebooks/detail.action?docID=3019187.
Created from inflibnet-ebooks on 2018-02-22 20:59:47.

$$B_j(x) = \frac{1}{6}\begin{cases} (x - x_j)^3 & x_j \le x < x_{j+1} \\ 1 + 3(x - x_{j+1}) + 3(x - x_{j+1})^2 - 3(x - x_j)^3 & x_{j+1} \le x < x_{j+2} \\ 1 + 3(x_{j+3} - x) + 3(x_{j+3} - x)^2 - 3(x_{j+3} - x)^3 & x_{j+2} \le x < x_{j+3} \\ (x_{j+4} - x)^3 & x_{j+3} \le x < x_{j+4} \end{cases}, \quad \text{(C.2)}$$

and $B_j(x)$ is equal to zero otherwise. Note that in this case the cubic polynomial is defined using four grid points. Because of the local definition of each *B*-spline, only 4 summands of Eq.(C.1) are non-zero. The calculation of the coefficients for the *B*-spline interpolation is performed as follows. We write for the given function value at the grid points x_i:

$$f(x_j) = \sum_{j=-2}^{N_x - 1} \gamma_j B_j(x_j) \quad \text{(C.3)}$$

which results in the equation:

$$\gamma_{j-3} + 4\gamma_{j-2} + \gamma_{j-1} = 6 f_j \ ; \text{for } j=1,\ldots\ldots N_x \quad \text{(C.4)}$$

where $f_j(x) = f_j$, and we assume as boundary condition that the derivative is equal to zero at the boundaries : $\gamma_0 = \gamma_{-2}$, $\gamma_{N_x - 1} = \gamma_{N_x - 3}$. We use the recursive ansatz:

$$\gamma_j = \gamma_{j+1} X_j + H_j \quad \text{(C.5)}$$

which inserted into Eq.(C4) yields by comparison the coefficients:

$$X_j = -\frac{1}{4 + X_{j-1}} \ ; \ X_{-2} = -2 \quad \text{(C.6)}$$

$$H_j = X_j (H_{j-1} - 6 f_{j+2}) \ ; \ H_{-2} = 3 f_1 \quad \text{(C.7)}$$

The values of X_{-2}, H_{-2} are obtained by considering the recursive ansatz with $j = 2$ and the left boundary condition $\gamma_0 = \gamma_{-2}$. The starting value of the recursion is obtained using the right boundary condition:

$$\gamma_{N_x - 1} = \frac{H_{N_x - 3} + H_{N_x - 2} X_{N_x - 3}}{1 - X_{N_s - 2} X_{N_x - 3}} \quad \text{(C.8)}$$

Copyright © 2009. Nova Science Publishers, Inc.. All rights reserved.

Baswell, Albert R.. Advances in Mathematics Research, Nova Science Publishers, Inc., 2009. ProQuest Ebook Central, http://ebookcentral.proquest.com/lib/inflibnet-ebooks/detail.action?docID=3019187.
Created from inflibnet-ebooks on 2018-02-22 20:59:47.

Once the coefficients γ_j are known, arbitrary interstitial function values $\widetilde{f} = f(x_j + \Delta_x)$ are now calculated as follows :

$$\widetilde{f} = \sum_{\kappa=0}^{3} \gamma_{j-\kappa} b_\kappa^x \tag{C.9}$$

where $j \equiv x_j$, $\Delta_x = x - x_j$, and :

$$\begin{aligned}
b_0^x &= \frac{1}{6}\Delta_x^3 \ ; \\
b_1^x &= \frac{1}{6}\left(1 + 3(\Delta_x + \Delta_x^2 - \Delta_x^3)\right) \\
b_2^x &= \frac{1}{6}\left(1 + 3((1-\Delta_x) + (1-\Delta_x)^2 - (1-\Delta_x)^3)\right) \ ; \\
b_3^x &= \frac{1}{6}\left(1-\Delta_x\right)^3
\end{aligned} \tag{C.10}$$

References

[1] Abbott, B.A. *An Introduction to the Method of Characteristics*; Thames and Hudson: London, 1966

[2] Pohn, E.; Shoucri, M.; Kamelander, G. *Comp. Phys. Comm*. 2005, 166, 81-93

[3] Shoucri, M. *Comp. Phys. Comm*. 2004, 164, 396-401

[4] Pohn, E.; Shoucri, M.; Kamelander, G. *Comp. Phys. Comm*. 2001, 137, 380-395;ibid 2001, 137, 396-404

[5] Yanenko, N.N. *The Method of Fractional Steps*, Springer-Verlag, New York, 1971

[6] Shoucri, M., Gerhauser, H., Finken, K-H. *Comp. Phys. Comm*. 2003, 154, 65-75

[7] Makar, P.A., Karpik, S.R. *Mon. Wea. Rev*. 1996, 124, 182-199

[8] Staniforth, A., Côté, J. *Mon. Wea. Rev*. 1991, 119, 2206-2223

[9] Sonnendrücker, E., Roche, J., Bertrand, P., Ghizzo, A. *J. Comp. Phys.* 1998, 149, 201

[10] Cheng, C.Z., Knorr, G. *J. Comp. Phys*. 1976, 22, 330-351

[11] Shoucri, M., Gagné, R. *J. Comp. Phys.* 1997, 24, 445-449; *Phys. Fluids* 1978, 21, 1168-1175, *IEEE Plasma Science* 1978, PS-6, 245-248; *J. Comp. Phys*. 1978, 27, 315-322

[12] Shoucri, M. *Phys. Fluids* 1978, 21, 1359-1365; ibid 1979, 22, 2038; ibid 1980, 23, 2030; *J. de Physique* 1979, 40, 38-39

[13] Shoucri, M., Storey, O. 1986, 29, 262-265; Simon, A., Short, R.W. *Phys Fluids* 1988, 31, 217

[14] Bertrand, P., Ghizzo, A., Feix, M., Fijalkow, E., Mineau, P., Suh, N.D., Shoucri, M. In *Nonlinear Phenomena in Vlasov Plasmas;* Doveil, F.;Ed.; Proc. Cargèse Workshop; *Les Editions de Physique*: Les Ulis, France, 1988; 109-125

[15] Cheng, C.Z. *J. Comp. Phys*. 1977, 24, 348-360

Copyright © 2009. Nova Science Publishers, Inc.. All rights reserved.

Baswell, Albert R.. Advances in Mathematics Research, Nova Science Publishers, Inc., 2009. ProQuest Ebook Central, http://ebookcentral.proquest.com/lib/inflibnet-ebooks/detail.action?docID=3019187.
Created from inflibnet-ebooks on 2018-02-22 20:59:47.

[16] Shoucri, M., Gagné, R. J. Comp. Phys. 1978, 27, 315-322; Shoucri, M. In Modeling and Simulation; *Proc. 10th Annual Pittsburgh Conference*; Publisher: Instrument Society of America, Pittsburgh, 1979; Vol. 10; 1187-1192
[17] Shoucri, M. *IEEE Plasma Science*, 1979, PS-7, 69-72
[18] Johnson, L.E. *J. Plasma Phys*. 1980, 23, 433-452
[19] Rickman, J.D. *IEEE Plasma Science* 1982, PS-10, 45-56
[20] Ghizzo, A., Bertrand, P., Shoucri, M., Johnston, T., Feix, M., Fijalkow, E. *J. Comp. Phys*. 1990, 90, 431-457
[21] Bertrand, P., Ghizzo, A., Johnston, T., Shoucri, M., Fijalkow, E., Feix, M. *Phys. Fluids* 1990, B2, 1028-1037
[22] Johnston, T., Bertrand, P., Ghizzo, A., Shoucri, M., Fijalkow, E., Feix, M. *Phys. Fluids* 1992, B4, 2523-2537
[23] Ghizzo, A., Shoucri, M., Bertrand, P., Johnston, T., Lebas, J. *J. Comp. Phys*. 1993, 108, 373-376
[24] Shoucri, M., Bertrand, P., Ghizzo, A., Lebas, J., Johnston, T., Feix, M., Fijalkow, E. *Phys. Letters A*, 1991, 156, 76-80
[25] Ghizzo, A., Bertrand, P., Lebas, J., Shoucri, M., Johnston, T. J., Fijalkow, E., Feix, M.R. *J. Comp. Phys*. 1992, 102, 417-422
[26] Bertrand, P., Ghizzo, A., Karttunen, S., Pättikangas, T., Salomaa, R., Shoucri, M. *Phys. Plasmas* 1995, 2, 3115-3129; *Physical Rev. E* 1994, 49, 5656-5659
[27] Ghizzo, A., Bertrand, P., Bégué, M.L., Johnston, T., Shoucri, M. *IEEE Plasma Science* 1996, 24, 370-378
[28] Bégué, M.L., Ghizzo, A., Bertrand, P. *J. Comp. Phys*. 1999, 151, 458-478
[29] Ghizzo, A., Bertrand, P., Shoucri, M., Johnston, T., Fijalkow, E., Feix, M.R., Demchenko, V.V., *Nucl. Fusion* 1992, 32, 45-65
[30] Brunner, S., Valeo, E. *Phys. Rev. Lett*. 2004, 93, 145003-1 -145003-4
[31] Strozzi, D., Shoucri, M., Bers, A., Williams, E., Langdon, A.B. *J. Plasma Physics*. 2006, 72, 1299-1302
[32] Manfredi, G., Shoucri, M., Feix, M., Bertrand, P., Fijalkow, E., Ghizzo, A. *J. Comp. Phys*. 1995, 121, 298-313
[33] Ghizzo, A., Bertrand, P., Shoucri, M., Fijalkow, E., Feix, M. *Phys. Fluids* 1993, B5, 4312-4326
[34] Manfredi, G., Shoucri, Shkarofsky, I., Ghizzo, A., Bertrand, P., Fijalkow, E., Feix, M., Karttunen, S., Pattikangas, T., Salomaa, R. *Fusion Tech*. 1996, 29, 244-260
[35] Manfredi, G., Shoucri, M., Dendy, R.O., Ghizzo, A., Bertrand, P. *Phys. Plasmas* 1996, 3, 202-217
[36] Manfredi, G., Shoucri, M., Bertrand, P., Ghizzo, A., Lebas, J.,Knorr, G., Sonnendrücker, E., Bürbaumer, H., Entler, W., Kamelander, G. *Phys. Scripta* 1998, 58, 159-175
[37] Shoucri, M., Lebas, J., Knorr, G., Bertrand, P., Ghizzo, A., Manfredi, G., Christopher, I., *Phys. Scripta* 1997, 55, 617-627; ibid 1998, 57, 283-285
[38] Shoucri, M., Manfredi, G., Bertrand, P., Ghizzo, A., Knorr, G. J. *Plasma Phys* 1999, 61, 191
[39] Watanabe, T.-H., Sugama, H., Sato, T. *J. Phys. Soc. Japan*, 2001, 70, 3565-3576
[40] Watanabe, T.-H., Sugama, H. *Trans. Theory Stat. Phys*. 2005, 34, 287-309
[41] Arber, T.D., Vann, R.G.L., *J. Comp. Phys*. 2002, 180, 339

Copyright © 2009. Nova Science Publishers, Inc.. All rights reserved.

Baswell, Albert R.. Advances in Mathematics Research, Nova Science Publishers, Inc., 2009. ProQuest Ebook Central, http://ebookcentral.proquest.com/lib/inflibnet-ebooks/detail.action?docID=3019187.
Created from inflibnet-ebooks on 2018-02-22 20:59:47.

[42] Pohn, E., Shoucri, M., Kamelander, G. *Comp. Phys. Comm*. 2005, 166, 81-93; *J. Plasma Physics*. 2006, 72, 1139-1143
[43] Pohn, E., Shoucri, M. *Proc. Vlasovia workshop* (to be published in *Commun. Nonlinear Sci. Numer. Simul.*) 2007
[44] Shoucri, M. *Czech. J. Phys*. 2001, 51, 1139-1151
[45] Batishchev, O., Shoucri, M., Batishcheva, A., Shkarofsky, I. *J. Plasma Physics* 1999, 61, 347- 364
[46] Ghizzo, A., Izrar, B., Bertrand, P., Fijalkow, E., Feix, M., Shoucri, M. *Phys. Fluids* 1988, 31, 72-82
[47] Ghizzo, A., Izrar, B., Bertrand, P., Feix, M.R., Fijalkow, E., Shoucri, M. *Phys. Lett. A* 1987, 120, 191-195
[48] Bernstein, I.B., Greene, S.M., Kruskal, M.D. *Phys.Rev.* 1957, 108, 546-554
[49] Knorr, G. *Plasma Phys*. 1977, 19, 529-538
[50] Knorr, G., Pecseli, H.L. *J. Plasma Phys*. 1989, 41, 157-170
[51] Reproduced from *Comp. Phys Comm*., Vol. 164; Shoucri, M., Gerhauser, H., Finken, K.H., *Study of the Generation of a Charge Separation and Electric field at a Plasma Edge using Eulerian Vlasov Codes in Cylindrical Geometry*, p. 139-141, Copyright 2004, with permission from Elsevier.
[52] Huot, F., Ghizzo A., Bertrand, P., Sonnendrücker, E., et al *J. Comp. Phys*. 2003, 185, 512-531
[53] Strozzi, D., Shoucri, M., Bers, A. *Comp. Phys. Comm*. 2004, 164, 156-159
[54] Shoucri, M., Matte, J.-P., Côté, A. *J. Phys. D* : *Appl. Phys*. 2003, 36,2083-2088
[55] Joyce, G., Montgomery, D. *J. Plasma Phys*. 1973, 10, 107-120
[56] Knorr, G. *Plasma Phys*.1974, 5, 423-434
[57] Marchand, R., Shoucri, M. *J. Plasma Phys*. 2001, 65, 151-160
[58] Shoucri, M. *Int. J. Num. Methods Eng.* 1981, 17, 1525-1538
[59] Shoucri, M., Knorr G. *Plasma Phys.* 1976, 18, 187-204
[60] Krane, B., Christopher, I., Shoucri, M., Knorr, G. *Phys. Rev. Lett*. 1998, 80, 4422-4425
[61] Ghizzo, A., Bertrand, B., Shoucri, M., Fijalkow, E., Feix, M.R. *J. Comp. Phys*. 1993, 108, 105- 121
[62] Grasso, D., Califano, F., Pegoraro, F., Porcelli, F. *Phys. Rev. Lett*. 2001, 86, 5051-5054
[63] Grasso, D., Borgogno D., Califano, F., Farina, D., Pegoraro, F., Porcelli, F. *Comp. Phys. Comm*. 2004, 164, 23-28
[64] Pegoraro, F., Liseikina, T., Echkina, E.Yu. *Trans. Theory Stat. Phys*. 2005, 34, 243-259
[65] Durran, D.R. *Numerical Methods for Wave Equations in Geophysical Fluid Dynamics; Text in Applied Mathematics* **32**; Springer: New-York, N.Y., 1998
[66] Dritschel, D.G., Polvani, L., Mohebalhojeh, A.R. *Mon. Wea. Rev*. 1999, 127, 1551-1565
[67] Imai, Y., Aoki, T., Shoucri, M. *J. Appl. Meteo. Climat*. 2007, 46, 388-395
[68] Reproduced from *Comp. Phys. Comm*., Vol. 176; Shoucri, M., *Numerical Solution of the Shallow Water Equations with a Fractional Step Method,* p. 23-32, Copyright 2007, with permission from Elsevier.
[69] Biskamp, D., Welter, H. *Phys. Fluids* 1989, B1, 1964-1979
[70] Grauer, R., Marliani, C. *Phys. Plasmas*, 1995, 2, 41-47
[71] Politano, H., Pouquet, A., Sulem, P.L. *Phys. Fluids* 1989, B1, 2330-2339
[72] Pouquet, A., Sulem, P.L., Meneguzzi, M. *Phys. Fluids*, 1988, 2635-2642

Copyright © 2009. Nova Science Publishers, Inc.. All rights reserved.

Baswell, Albert R.. Advances in Mathematics Research, Nova Science Publishers, Inc., 2009. ProQuest Ebook Central, http://ebookcentral.proquest.com/lib/inflibnet-ebooks/detail.action?docID=3019187.
Created from inflibnet-ebooks on 2018-02-22 20:59:47.

[73] Shoucri, M. *Proc. Vlasovia Workshop*, (to be published in *Comm. Nonlinear Sci. Numer. Simul.*) 2007
[74] Grandgirard, V., Brunetti, M., Bertrand, P., Besse, N., Garbet, X., Ghendrih, P., Manfredi, G., Sarazin, Y., Sauter, O., Sonnendrücker, E., Vaclavick, J., Villard, L. *J. Comp. Phys*. 2006, 217, 395-423
[75] Jenko, J. *Comp. Phys. Comm*. 2000, 125, 196-209
[76] Candy, J., Waltz, R.E. *J. Comp. Phys*. 2003, 186, 545-581
[77] Idomura, Y., Watanabe, T.-H., Sugama, H. *C. R. Physique* 2006, 7, 650-669
[78] Nakamura, T., Yabe, T. *Comp. Phys. Comm*. 1999, 120, 122-135
[79] Mangeney, A., Califano, F., Cavazzoni, C., Travnicek, P. *J. Comp. Phys*. 2002, 179, 475-490
[80] Purnell, D.K. *Mon. Wea. Rev*. 1976, 104, 42-48
[81] Johnston, T.W., Picard, G., Matte, J.P., Fuchs, V., Shoucri, M. *Plasma Phys. Cont. Fusion* 1985, 27, 473-485
[82] Reveillé, T., Bertrand, P., Ghizzo, A., Lebas, J., Johnston, T.W., Shoucri, M. *Phys. Fluids* 1992, B4, 2665-2668
[83] Toro, E.F. *Riemann Solvers and Numerical Methods for Fluid Dynamics*; Springer: Berlin, 1999
[84] de Boor, C. A Practical Guide to Splines; *Applied Mathematics* **27**; Springer-Verlag: New-York, N.Y., 1978
[85] Ahlberg, J.H., Nilson, E.N., Walsh, J.L. *The Theory of Splines and their Applications*; Academic Press: New York, N.Y., 1967

Copyright © 2009. Nova Science Publishers, Inc.. All rights reserved.

Baswell, Albert R.. Advances in Mathematics Research, Nova Science Publishers, Inc., 2009. ProQuest Ebook Central, http://ebookcentral.proquest.com/lib/inflibnet-ebooks/detail.action?docID=3019187.
Created from inflibnet-ebooks on 2018-02-22 20:59:47.

Copyright © 2009. Nova Science Publishers, Inc.. All rights reserved.

Baswell, Albert R.. Advances in Mathematics Research, Nova Science Publishers, Inc., 2009. ProQuest Ebook Central,
http://ebookcentral.proquest.com/lib/inflibnet-ebooks/detail.action?docID=3019187.
Created from inflibnet-ebooks on 2018-02-22 20:59:47.